# Direct visualization of cellular protein complexes *in situ* by fluorescence-guided cryo-FIB-SEM and cryo-ET

Thesis by

Jue (Phyllis) Wang

In Partial Fulfillment of the Requirements for the Degree

of

Doctor of Philosophy


CALIFORNIA INSTITUTE OF TECHNOLOGY

Pasadena, California

2025

(Defended February 20, 2025)

Jue (Phyllis) Wang
ORCID: 0000-0002-5623-0994

# ACKNOWLEDGEMENTS

I would like to express my sincere gratitude to my advisor, Dr. Grant Jensen. He has always been a role model to me, and I'm grateful for all the wisdom and guidance he has shared with me. Throughout this journey, I have gained invaluable experience in developing a project, finding resources, effectively communicating with colleagues and collaborators, and critically analyzing primary literature. Collectively, these experiences allow me to grow as an independent researcher.

I would also like to thank my collaborator, Dr. Hao Wu, for constantly giving me feedback, sharing knowledge, and exchanging ideas on my project. I truly respect all hard work, time, and patience she has put on me.

I am also grateful to be a member of Dr. Pete Dahlberg's group. I appreciate the time we spent troubleshooting the instrument and dealing with failures at the beginning of my project.

I am also thankful to my undergraduate research advisor and longtime friend, Dr. Elaine Marzluff, who is also a Caltech alumnus, for bringing me to science and encouraging me to pursue a career in science.

I would also like to thank Amy Kendall, Dr. Terunaga Nakagawa, and Dr. Michael Sheedlo for their patience and time to introduce me to the world of cryo-EM.

To my mom, I could not have accomplished this without your unwavering support during this demanding journey.

# ABSTRACT

Cryogenic electron tomography (cryo-ET) is a technique that can reconstruct three-dimensional volumes of large protein complexes *in situ* at sub-nanometer resolution. In addition to imaging proteins extracted from cells, cryo-ET also allows direct visualization of macromolecular complexes in their native environment. To reveal molecular details buried deeply inside thick eukaryotic cells, cryogenic focused ion beam milling with scanning electron microscopy (cryo-FIB-SEM) has been established as the leading approach for preparing thin sections of cells suitable for cryo-ET. Recent advances in cryo-FIB-SEM systems integrate fluorescence microscopy (cryo-FM-FIB-SEM) to help direct the milling to specific labeled regions of interest. This method has had success localizing large organelles and protein aggregates. Unfortunately, it is difficult to localize small and rare targets along the optical axis of the cryo-FIB. This thesis work pioneered a customized integrated tri-coincident imaging system (ENZEL) that allows for simultaneous fluorescence imaging and cryo-FIB milling. This novel method allows precise targeting of small and rare structures with a high success rate compared to other systems. To demonstrate the imaging workflow, we applied this approach to visualize the microtubule organizing center (MTOC), a crucial organelle responsible for cell division and cellular transport in mammalian cells. It presents as a single fluorescent punctum expanding approximately 1 μm in diameter in live cells, making it a challenging target for cryo-FM-FIB-SEM. Our cryo-tomograms resolved the molecular architecture of the MTOC and revealed molecular details at the microtubule nucleation sites. We then used the ENZEL to explore more complicated biological systems. Here we chose the NLRP3 inflammasome, a master mediator of innate immunity colocalized with the MTOC. We captured the first in-situ image of the NLRP3 inflammasome and

showed new mechanistic insights that this complex forms a condensate at the MTOC, halting cell division and inducing drastic organelle changes.

# PUBLISHED CONTENT AND CONTRIBUTIONS

**Wang, J.**, Sica, A. V., Jensen, G. J., and Dahlberg, P. D. (2025). "Targeted milling of cellular samples using a cryogenic coincident fluorescence, electron, and ion beam microscope." Manuscript is under review in Journal of Visualized Experiments.

J. W. conceived and designed the imaging workflow, collected the data, analyzed the data, prepared the figures, and wrote the manuscript.

**Wang, J.**, Wu, M., Magupalli, V. G., Dahlberg, P. D., Wu, H., and Jensen, G. J. (2025). "Human NLRP3 inflammasome activation leads to formation of condensate at the microtubule organizing center." bioRxiv. https://doi.org/10.1101/2024.09.12.612739

J. W. conceived experiments, prepared samples, acquired and analyzed data, prepared the figures, and wrote the manuscript.

Dutka, P.*, Liu, Y.*, Maggi, S.*, Ghosal, D., **Wang, J.**, Carter, S. D., Zhao, W., Vijayrajratnam, S., Vogel, J. P., Jensen, G. J. (2023). "Structure and Function of the Dot/Icm T4SS." bioRxiv. https://doi.org/10.1101/2023.03.22.533729

J. W. prepared samples, acquired and analyzed cryo-ET data of bacteria infecting human macrophages, prepared the figures for this section, and wrote this section of the manuscript.

Shin, B., Zhou, W., **Wang, J.**, Gao, F., and Rothenberg, E. V. (2023). "Runx factors launch T-cell and innate lymphoid programs via direct and gene network-based mechanisms." Nat. Immunol. **24**(9):1458-1472. https://doi.org/10.1038/s41590-023-01585-z. Author correction: https://doi.org/10.1038/s41590-023-01716-6.

J. W. prepared samples for RNA-seq, acquired and analyzed RNA-seq data, and edited the manuscript.

# TABLE OF CONTENTS

# LIST OF ILLUSTRATIONS AND/OR TABLES

*Number* *Page*

*Chapter 1*

# INTRODUCTION

Since the first atomic-resolution model was determined by cryogenic electron microscopy (cryo-EM) in 1990 (Henderson et al. 1990), studying protein structures and dynamics in their native environments became a theme of structural biology (Clarey et al. 2008, Zhang et al. 2010, Liao et al. 2013). Cryo-EM utilizes electrons to generate two-dimensional projections of protein complexes randomly distributed in a layer of vitrified ice, which provides a frozen hydrated environment for "live" protein complexes (Nogales and Scheres 2015, Frank 2016, Cheng 2018, Nogales and Mahamid 2024). Collections of numerous projections of the same protein complex are used to reconstruct a three-dimensional model. Since protein complexes are prepared in micro-litters of solution, cryo-EM is particularly powerful for studying protein complexes that are known to be challenging to crystallize or purify. In 2014, the development of the direct electron detector and subsequent computational advances revolutionized the field, improving sensitivity of electron detection and speed of data collection (Li et al. 2013, McMullan et al. 2014, Wu et al. 2016) to achieve time- and labor-efficient high-resolution structural determinations (Liao et al. 2013, Fribourgh et al. 2014, Verba et al. 2016). More recent studies in cryo-EM further emphasized the idea of "native" environments by extracting protein complexes directly from cells instead of overexpressing a construct in reconstituted systems (Su et al. 2021, Laporte et al. 2024). However, cryo-EM with isolated protein complexes still lacked cellular context.

Cryogenic electron tomography (cryo-ET) provides a way to directly visualize biological specimens in *in situ*, thus restoring the cellular context. Instead of collecting and averaging single projections representing a variety of orientations of a protein complex, cryo-ET collects projections of the same target of interest while tilting the sample through a range of angles, commonly +/- 60 degrees, to obtain a three-dimensional volume. This method has enabled many studies of protein complexes in small and thin organisms such as bacteria and amoeba. However, difficulties remain when imaging larger and thicker organisms. For instance, eukaryotic cells are often too thick to image directly with an electron because of multiple scattering events, which increase noise and reduce the overall image quality. One strategy to overcome this limitation is to thin cells to 200 nm or less before imaging them (Villa et al. 2013, Wagner et al. 2020, Kaplan et al. 2021, Lam and Villa 2021). The preferred method uses a focused ion beam (FIB) (5-10 nm in diameter) to ablate thick cells, , typically a few microns, to a final thin slice called the lamella, revealing molecular details originally buried inside a thick cell (Villa et al. 2013, Wagner et al. 2020, Kaplan et al. 2021, Lam and Villa 2021). Previous studies in this field have utilized this technique to visualize cellular features in a variety of cell types, delineating organelle morphology, host-defense interactions, and various states of protein complexes *in situ*. However, it can be difficult to localize specific objects in thick cells as there is no way to know if the final lamella contains the object of interest. In addition, cells are crowded, full of organelles, proteins, and even unidentified structures, making them challenging for interpretation without any guidance. For these reasons, recent technological advances combined cryo-ET with fluorescence microscopy (cryo-FM-FIB-SEM) to help direct the milling process to look at fluorescently labeled regions. Studies using cryo-FM-FIB-SEM have succeeded in targeting organelles such as mitochondria and large protein aggregates (Guo et al. 2018, Carter et al. 2020, Wu et al. 2020, Liu et al. 2023), but technical obstacles remain in visualizing relatively small targets, typically less than a

micron by fluorescence. Key challenges include the following: first, it is difficult to precisely localize the target along the optical axis in the FIB settled at angle, which is settled at an angle of ~10-20 degrees against the sample plane; second, the axial resolution (or z resolution) in fluorescent microscopy is always the lowest, but it is a crucial parameter to locate a given target at any specific depth inside the cell; and third, standard workflows require frequent sample stage movements to perform milling and fluorescence imaging, generating errors in target registration. Collectively, all these challenges lead to imprecise target localization during milling and ultimately, the loss of targets due to milling. Further optimization in instrumental design and imaging pipeline are necessary to improve the precision of target localization by cryo-FM-FIB-SEM.

There have been multiple attempts to improve the cryo-FM-FIB-SEM workflow aiming to precisely direct the milling process (Guo et al. 2018, Carter et al. 2020, Wu, Mitchell et al. 2020, Yang et al. 2021, Sexton et al. 2022, Liu et al. 2023) (Fig. 1-1). The traditional approach involves two standalone instruments, a cryo-FIB-SEM scope and a fluorescence microscope equipped with a cryo-stage (Fig. 1-1). After identifying a target of interest under the cryo-FM, a sample is transferred to the cryo-FIB-SEM, and cryo-FM images with selected target of interest are loaded and registered to the FIB view for guided milling. After the lamella is generated, it is sent back to the cryo-FM to take a post-milling fluorescent image to ensure the lamella contains the target of interest (Liu et al. 2023). However, frequent sample transfer can introduce ice contamination covering the surface of the lamella or cause physical damage on the lamella. Additionally, because all sample transferring is done manually, it is labor-intensive to obtain enough lamellae containing the targets of interests to for subsequent cryo-ET imaging. One recent study also reported a less than 5% success rate following

this method (Liu et al. 2023), suggesting potential optimization is needed to achieve precise target localization by cryo-FIB-SEM.

The latest technological advances in cryo-FM-FIB-SEM introduced "in-column fluorescence," which allows vitrified cells to be viewed and milled in the same instrument. The in-column fluorescence system integrates an upright cryo-FM with a cryo-FIB-SEM platform (Fig. 1-1). Though the FM and FIB-SEM are in the same instrument, the sample still rotates position within the column: vitrified cells are milled with the cryo-FIB-SEM and then moved to the fluorescence imaging position to be checked for fluorescent signals (Wagner et al. 2020). Using an in-column fluorescence system, one recent study developed a "slice-and-view" approach to identifying their target of interest: instead of one or two rounds of milling followed by FM, they milled a small section of the vitrified cell away, imaged it with the SEM, and repeated the process until their target of interest was fully visible, then took a final fluorescent image to confirm target was retained on the final lamella (Wu et al. 2020). However, this workflow is not suitable for targets exhibit no contrast under SEM (Wu et al. 2020). The integrated cryo-FM and cryo-FIB-SEM system allows direct visualization of protein aggregates and organelles, but no small target has been reported utilizing this workflow. The precision in target localization is potentially compromised during frequent and drastic stage movements between the cryo-FIB milling position and the cryo-FM imaging position.

We therefore believe a universal platform supporting precise target localization and minimizing stage motions will expand the use of cryo-FM-FIB-SEM for visualizing small cellular structures *in situ*. We instead pioneered a customized tri-coincident imaging system (ENZEL) equipped with an inverted fluorescent microscope, which aligns the FM, SEM, and FIB beams to aligned to one focal point at

the sample stage (Boltje et al. 2022). This tri-coincident configuration enables simultaneous fluorescence imaging and cryo-FIB milling without any stage motion, and real-time fluorescence intensity can be used to determine when to stop milling while we are approaching the target of interests (Boltje et al. 2022). To demonstrate its effectiveness, we used the ENZEL to visualize the microtubule organizing center (MTOC) in human macrophages. The MTOC is a crucial organelle responsible for regulating cell division and cellular transport. The primary MTOC in mammalian cells is known as the centrosome, which consists of the centrioles, the pericentriolar material (PCM), and associated microtubules (MT). Although the centrosome architecture has been known for years, this complex has not been captured *in situ* in mammalian cells. Furthermore, the biogenesis of microtubule nucleation sites and how they interact with PCM are yet to be understood. We utilized a tubulin marker previously utilized in super-resolution light microscopy to label the MTOC, and cryo-EM showed the MTOC as a single punctum expanding approximately 1 μm in diameter by fluorescence. We then utilized the ENZEL to target the MTOC, relying on real-time fluorescence to show us when to stop milling, and had a ~70% success rate. Compared to other available systems previously described, this is a significant improvement in precise target localization.

We further utilized the ENZEL to investigate the molecular mechanisms of more complicated biological systems, for instance, the immune system. The immune system involves delicate networks of signaling molecules, cells, and organs working together to protect our body against infections. There are a tremendous amount of biochemistry experiments and animal studies on the immune system, however, lack of suitable technology precludes direct visualization of key immune pathways *in situ*. Here we investigated an important family of molecular complexes in the immune system called inflammasomes. Canonical inflammasomes are cytoplasmic supramolecular complexes

responsible for detecting and sensing cellular distress (Stutz et al. 2009, Broz and Dixit 2016, Wang et al. 2020, Wang et al. 2021). Upon activation, these multi-protein complexes oligomerize, leading to proteolytic cleavage of pro-caspases, which further activates downstream proinflammatory cytokine release (Stutz et al. 2009, Broz and Dixit 2016, Wang et al. 2020, Wang et al. 2021). Canonical inflammasomes are architecturally conserved and comprise a sensor protein, an adaptor, and a downstream effector. The tripartite structure is thought to oligomerize to form a star-shaped higher-order complex, expanding to ~1-2 μm in diameter (Stutz et al. 2009, Broz and Dixit 2016, Swanson et al. 2019, Wang et al. 2020, Wang et al. 2021). One of the most extensively studied inflammasomes, the NLRP3 inflammasome, is the largest known inflammasome complex (Stutz et al. 2009). It is composed of an NLRP3 sensor protein, an apoptosis speck-like protein (ASC) adaptor, and a pro-caspase-1 effector (Stutz et al. 2009, Broz and Dixit 2016, Swanson et al. 2019, Wang et al. 2020, Wang et al. 2021). Activation of NLRP3 inflammasomes involves two consecutive steps (Fig. 1-2): In macrophages, Toll-like receptors on the cell surface recognize various pathogen-associated molecular patterns (PAMPs) or damage-associated molecular patterns (DAMPs) and activate gene expression of precursor proteins (Stutz et al. 2009, Broz and Dixit 2016, Swanson et al. 2019, Wang et al. 2020, Wang et al. 2021). The second step initiates inflammasome formation and oligomerization at the microtubule organizing center (MTOC) through interactions between the centrosomal kinase NEK7 and the NLRP3 sensor protein (Sharif et al. 2019, Magupalli et al. 2020). The oligomerized NLRP3 further recruits ASC, which is known to polymerize into filamentous macromolecular structures called ASC filaments (Sborgi et al. 2015, Swanson et al. 2019, Liu et al. 2023). ASC filaments direct pro-caspase-1 processing via proximity-induced self-cleavage to produce the active state, caspase-1 (Fig. 1-2) (Sborgi et al. 2015, Swanson et al. 2019, Liu et al. 2023). Fully assembled NLRP3 inflammasomes then convert the inactive pro-IL-1β to the mature cytokine IL-

1β and activate a downstream inflammatory response (Fig. 1-2) (Stutz et al. 2009, Broz and Dixit 2016, Wang et al. 2020, Wang et al. 2021). One intriguing feature of the NLRP3 inflammasome is that it is assembled at the MTOC, and previous studies have shown NLRP3 inflammasome activation and cell division are mutually exclusive. Recent studies suggest the MTOC is involved in generating immune responses because cytoskeletal polarization plays a critical role T-cell activation response (Kumar et al. 2014, Vertii et al. 2016, Qi and Zhou 2021, Weier et al. 2022, Schapfl et al. 2024). However, how MTOC interacts with the NLRP3 inflammasome activation pathway requires further characterization. Early studies in this field revealed that NLRP3 inflammasome hyperactivity is associated with autoinflammatory diseases in humans (Stutz et al. 2009, Broz and Dixit 2016, Wang et al. 2020, Wang et al. 2021). It has also been implicated in the development of Alzheimer's disease, cardiovascular diseases, and age-related metabolic complications. It has also been shown that NLRP3 inflammasome activation also mediates cardiac inflammation during the progression of heart failure (Abbate et al. 2020, Wu et al. 2021). Though the mechanism of NLRP3 inflammasome activation and regulation remain elusive, it has become an emerging pharmacological target because of its significance as a critical participant in innate immunity (Zahid et al. 2019, Abbate et al. 2020, Christgen et al. 2020).

There has been extensive structural analysis on the NLRP3 inflammasome to elucidate the molecular basis of its architecture and activation mechanism. Cryo-EM enabled structural characterization of isolated NLRP3 components; however, proteins in the NLR family are known to be challenging for *in vitro* protein purification (Wang et al. 2021). Recent single-particle work revealed that NLRP3 and ASC come together as a disc structure, but NLRP3 alone forms a cage-like conformation (Fig. 1-3A-B) (Andreeva et al. 2021, Hochheiser et al. 2022, Ohto et al. 2022, Xiao et al. 2023). Other studies

in this field revealed protein-protein interactions between NEK7 and the inactive NLRP3 monomers in the inactive state (Fig. 1-3C) (Sharif et al. 2019). Structures of the ASC and caspase-1 filaments have been determined *in vitro* by a combination of different structural techniques, revealing a helical arrangement (Fig. 1-3D) (Lu et al. 2014, Sborgi et al. 2015, Li et al. 2018). A cryo-ET study in an ASC-overexpressing cell line reported short ASC filament networks far from the MTOC (Liu et al. 2023). While all studies determined the structures of various isolated NLRP3 components, the overall architecture of NLRP3 inflammasomes *in vivo* remained unclear. The current structural model of a fully assembled NLRP3 inflammasome is based on early electron micrographs of the "star-shaped" reconstituted AIM2 inflammasome ternary complexes (Fig. 1-3E), and the fully assembled NLRP3 and NEK7 complex was modeled according to the cryo-EM structure of the NLRC4 oligomer (Zhang et al. 2015). Therefore, direct visualization of the fully assembled NLRP3 inflammasome is necessary to compile all available structural information.

This thesis focuses on utilizing state-of-the-art fluorescence-guided cryo-FIB-SEM (ENZEL) and cryo-ET to elucidate the molecular architecture of two key players in the innate immunity, the MTOC and NLRP3 inflammasome. Chapter 2 is an article currently under review at *Journal of Visualized Experiments* that describes the instrumentation and methods used to achieve targeted milling for sub-diffraction-limited specimen. Compared to previous methods, this imaging platform significantly improves the success rate of retaining the target of interest within the final lamella. The ENZEL utilizes a unique tri-coincident design to allow simultaneous fluorescent imaging and milling without moving the stage. This chapter describes detailed protocols for alignment of the tri-coincident system, target identification and localization, and stepwise lamella generation. Representative results targeted the MTOC via a fluorescent marker on tubulin.

Chapter 3 is a summary of a manuscript in preparation that describes the molecular architecture of the MTOC, a key organelle responsible for cell division and cellular transport. In mammalian cells, the MTOC is often referred to as the centrosome. Abnormal centrosomal activity has been linked to uncontrollable cell growth and cancer. The centrosome consists of centrioles, a surrounding cloud of proteins called the pericentriolar material (PCM), and associated microtubule networks. Previous studies have shown the centrosome structure in isolated systems but did not provide the complete MTOC structure. This chapter describes the structural organization of the centrosome and microtubule nucleation sites in human macrophages *in situ*. Cryo-tomograms demonstrate cellular features of the centrioles, PCM, and microtubule networks, and detailed structural analysis provides new mechanistic insights regarding microtubule nucleation. Further work on pursuing a subtomogram average of the microtubule nucleation site at multiple functional states is planned and those results will be added to the manuscript before it is submitted for publication.

Chapter 4 is a paper that we submitted to *Science* describing the molecular mechanism of NLRP3 inflammasome activation. The NLRP3 inflammasome mediates IL-1beta maturation, a crucial step in the inflammation pathway. Its dysregulation has been linked to numerous human diseases, and novel treatments selectively targeting the NLRP3 inflammasome have become an emerging therapeutic strategy. In this chapter, cryo-tomograms of the NLRP3 inflammasome at different stages of activation are shown in frozen human macrophages. Instead of a giant molecular complex composed of filamentous structures, cryo-tomograms reveal dense condensates of NLRP3 within and around the MTOC. NLRP3 inflammasome condensates further disrupts centriole conformation, potentially disrupting the cell cycle. In an early stage of activation, complete Golgi expansion and dispersion ferry NLRP3 in numerous small, uniformly sized vesicles to the MTOC.

Following activation, organelle changes such as mitochondrial damage and autophagosome formation are observed in cryo-tomograms.

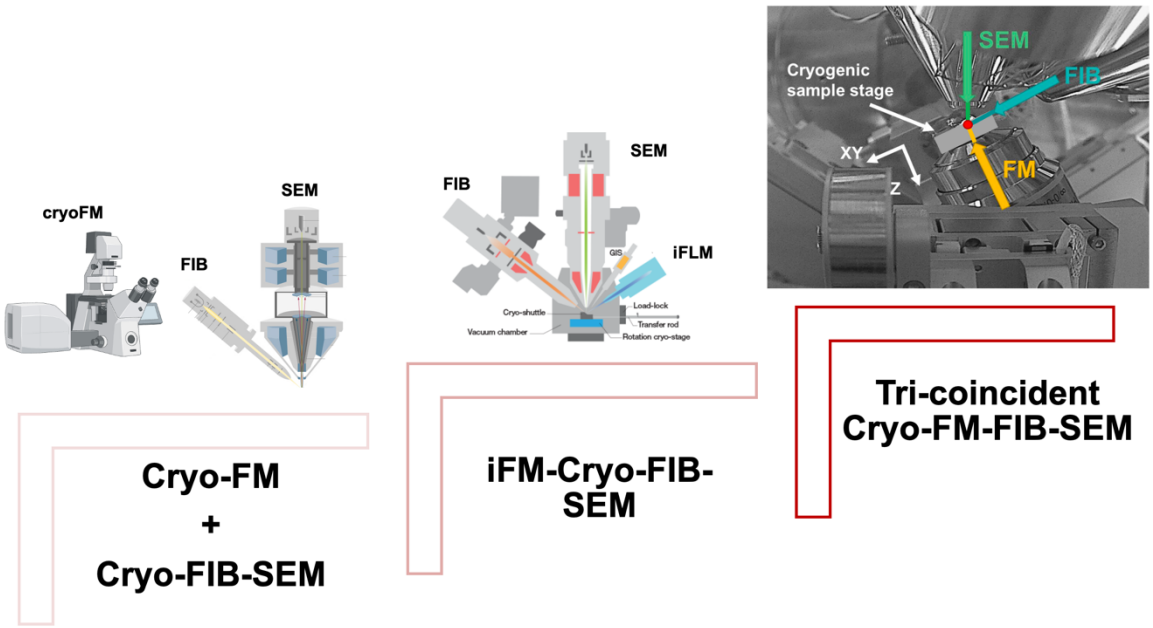


**Figure 1-1. Schematics of cryo-FM and cryo-FIB-SEM instruments.** Cryo-FM+Cryo-FIB-SEM: the cryo-FM was created with Biorender [Figure was created with Biorender, https://biorender.com] and the cryo-FIB-SEM was adapted from Zeiss Dual Beam system (zeiss.com) [accessed 2/2/2025]. iFM-Cryo-FIB-SEM was adapted from ThermoFisher Aquilos2 system (thermofisher.com) [accessed 2/2/2025]. Tri-coincident cryo-FM-FIB-SEM, or the ENZEL system was adapted from literature (Boltje, Hoogenboom et al. 2022) [Figure was created with Biorender, https://biorender.com.]

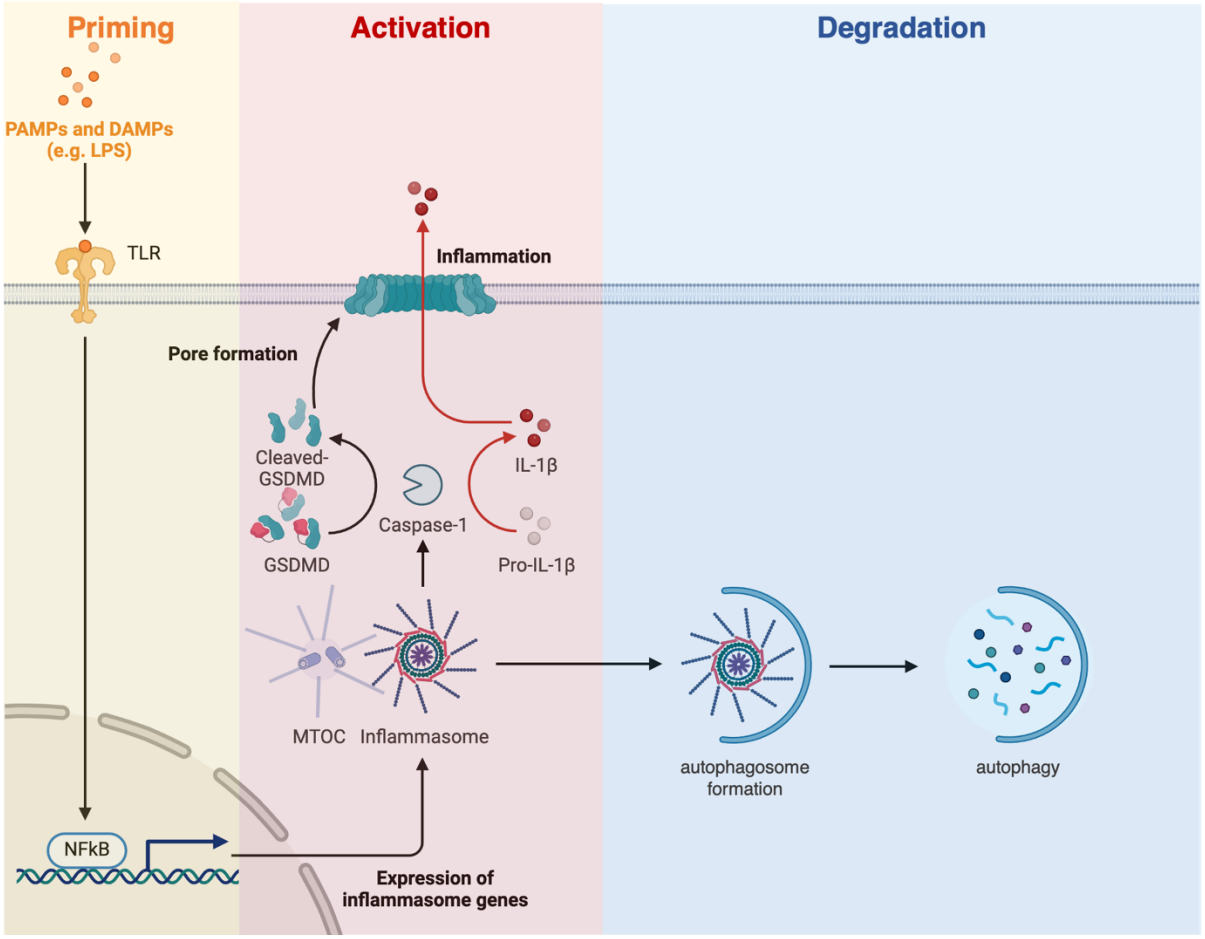


**Figure 1-2. Schematics of NLRP3 inflammasome activation in macrophages.** Priming is initiated by pathogen-associated molecular patterns (PAMPs) and damage-associated molecular patterns (DAMPs), such as LPS, *Clostridiodes difficile* toxins, and particulates. Activation leads to the formation of fully assembled NLRP3 inflammasome. Activation of the NLRP3 inflammasome also induces formation of GasderminD (GSDMD) pores on the cell surface and activates calcium efflux, ultimately leading to pyroptosis. The fully assembled NLRP3 inflammasome is also marked for autophagy to prohibit over-activation of immune responses [Figure was created with BioRender, https://BioRender.com.]

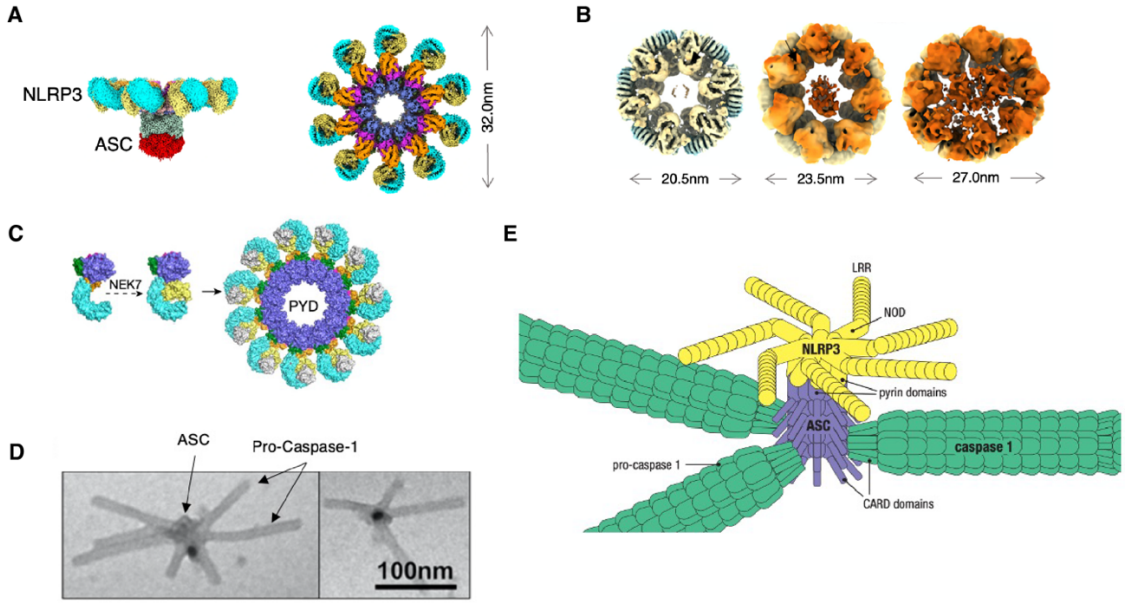


**Figure 1-3. Modeling of fully assembled NLRP3 inflammasome. (A)** Cryo-EM structure of the NLRP3 inflammasome disc [Figure adapted from (Xiao et al. 2023)]. **(B)** Cryo-EM structures of NLRP3 cages [Figure adapted from (Andreeva et al. 2021)]. **(C)** Cryo-EM structure of NLRP3 monomer in complex with NEK7. The assembled NLRP3 oligomer is modeled based on the NLRC4-NAIP structure [Figure adapted from (Zhang et al. 2015, Sharif et al. 2019)]. **(D)** Electron micrographs of the AIM2 ternary complex. The central stalk is formed by ASC and surrounded by branched capase-1 filamentous polymers. ASC is immunogold-labeled (shown as dark spots) [Figure adapted from (Lu et al. 2014)]. **(E)** Model of the NLRP3 inflammasome based on available structural information [Figure adapted from (Murphy and Weaver 2017)].

*Chapter 2*

# TARGETED MILLING OF CELLULAR SAMPLES USING A CRYOGENIC COINCIDENT FLUORESCENCE, ELECTRON, AND ION BEAM MICROSCOPE

*Adapted from:*

Jue Wang, Anthony V. Sica, Grant J. Jensen, and Peter D. Dahlberg. 2025. "Targeted milling of cellular samples using a cryogenic coincident fluorescence, electron, and ion beam microscope." Manuscript is under review in *Journal of Visualized Experiments*.

## ABSTRACT

Cryogenic focused ion beam milling with scanning electron microscopy (Cryo-FIB-SEM) has been established over the past decade as the leading approach for preparing thin sections of cells to electron semi-transparency for subsequent cryogenic tomography (Cryo-ET). It is often the case that specific structures within the cellular environment are of interest and for this reason fluorescence microscopy has been integrated into Cryo-FIB-SEM systems to help direct the sectioning process to fluorescently labelled regions of interest. Unfortunately, this integration is often done with the optical and ion microscopes having entirely different focal planes at different regions within vacuum chamber, akin to having two separate microscopes. This integration strategy necessitates a registration process between optical and ion images, which lacks the precision necessary to routinely capture rare and small structures of interest *in situ*. Here we report a workflow using a customized integrated tri-coincident imaging system (ENZEL) that enables for simultaneous fluorescence imaging and milling. Real-time fluorescence intensity is used to determine when to stop milling and from what direction milling should be done to ensure target capture in the final thin section. Here we apply this approach to visualize the microtubule organizing center (MTOC) in vitrified macrophages. The MTOC is a crucial organelle responsible for cell division and cell differentiation in mammalian cells displayed as a single fluorescent punctum expanding approximately 1 μm in diameter in live cells. Using this approach we have successfully localized the MTOC with high fidelity to thin sections of vitrified cells and subsequent tomographic reconstructions reveal detailed organization of microtubules at the MTOC and interactions with other organelles. This established workflow demonstrates high precision correlative Cryo-FM and FIB-SEM can be achieved without any axial registration process and can be applied to a wide range of biological specimens.

## 2.1 INTRODUCTION

Cryo-ET has been widely applied to observe biological specimens in their near-native environment (Komeili et al. 2006, Mahamid et al. 2016, Bykov et al. 2017, Hampton et al. 2017, Xue et al. 2022). Instead of extracting proteins from cells, Cryo-ET provides an understanding of biological processes with molecular scale resolution *in situ*. However, eukaryotic cells can be several microns thick which is beyond the penetration power of the electron beam without introducing severe radiation damage. One strategy to overcome this limitation is to ablate the majority of the cell with a cryogenic focused ion beam (Cryo-FIB), in a process known as Cryo-FIB milling. This process achieves thin sections sufficient for electron semi-transparency allowing subsequent Cryo-ET to reveal molecular details originally buried inside (Rigort and Plitzko 2015, Arnold et al. 2016, Lam and Villa 2021, Noble and de Marco 2024).

In standard workflows, samples are first properly preserved in vitrified ice by plunge freezing (Iancu et al. 2006, Dobro et al. 2010) and loaded into a dual-beam instrument that contains both a Cryo-FIB and scanning electron microscope (SEM), where imaging with the SEM can be used to direct milling to subcellular structures such as organelles. Samples are ablated by stepwise Cryo-FIB milling with a goal to preserve a target of interest in a final sub-200 nm thick slice which is suitable for Cryo-ET imaging (Rigort and Plitzko 2015, Wagner et al. 2020, Lam and Villa 2021). However, this standard approach presents two key challenges that this protocol addresses. First, it is often desired to obtain Cryo-ET of specific subcellular structures that are far below the resolution limit of the SEM when performed on unstained biological material. How can milling be directed to these regions? Second, once a thin section is obtained and Cryo-ET is performed, the resulting grayscale

reconstructions often lack the resolution necessary to identify specific biomolecule of interest. How can the positions of specific biomolecules be identified in the resulting Cryo-ET reconstructions?

For the solution to both challenges, the community has turned to fluorescence microscopy. It is now routine to fluorescently label specific biomolecules of interest for example through genetically encoded fluorescent proteins, or the addition of exogenous dyes that bind specific proteins (Hampton et al. 2017, Guo et al. 2018, Carter et al. 2020). Using cryogenic fluorescence microscopy of vitrified cells, we can direct the milling process to regions of interest and correlate the final light micrographs taken after milling is completed to the resulting tomographic reconstructions. The correlation of light and electron microscopy is a well-established approach known as cryogenic correlative light and electron microscopy (Cryo-CLEM) and has been used extensively to identify the locations of specific proteins in the context of Cryo-ET reconstructions (Arnold et al. 2016, Hampton et al. 2017, Guo et al. 2018, Carter et al. 2020). More recently advanced optical methods have been employed, such as the use of fluorescent biosensors and super-resolution (Perez et al. 2022, Sexton et al. 2022, Sartor et al. 2023). The use of fluorescence microscopy to direct milling is more recent, with initial workflows being developed roughly a decade ago (Arnold et al. 2016). In these initial workflows stand-alone light microscopes were used to acquire 2D or 3D fluorescence information and this was followed by Cryo-FIB-SEM (Arnold et al. 2016) where the information from fluorescence was painstakingly registered to the Cryo-FIB-SEM micrographs. More recently fluorescent microscopes have been integrated into the Cryo-FIB-SEM vacuum chamber, which reduces ice contamination from transferring the samples between microscopes and makes fluorescence imaging of the final lamella more feasible. There have been multiple imaging platforms

to combine fluorescent microscopy and cryo-FIB-SEM to achieve fluorescence-guided milling. Previous studies showed successful targeting of organelles and large protein complexes (Hampton et al. 2017, Guo et al. 2018, Carter et al. 2020). However, with few exceptions (Li et al. 2023), this integration has been done with the optical microscope having a different focal plane in a separate region of the vacuum chamber from the FIB-SEM. This geometry still necessitates the challenging registration process between the fluorescence micrographs and FIB-SEM micrographs to direct milling. This registration process comes with inherent errors due to refractive index mismatch that leads to apparent focal shifts (Loginov et al. 2024, Petrov and Moerner 2020), and motion of the sample during milling. Further, registration is often achieved through the addition of micron diameter fluorescent beads that are visible in each modality, but this can obscure fluorescence of interest in the sample. These aspects have prohibited the routine capture of small and rare targets, for example, targets that are less than a micron in axial extent, in the final lamella.

Here we report the use of a tri-coincident imaging system that possesses a FIB, SEM, and FM all at a single focal position to both direct milling and acquire multicolor cryogenic fluorescence microscopy data of the final thin lamella for subsequent correlative analysis and localization of sub-diffraction limited targets (Boltje et al. 2022). To direct milling we utilized the capability of the tri-coincident system to monitor changes in fluorescence intensity while milling to ensure we preserve the target of interest in the final lamella. We also use a customized toolkit to perform image transformation to obtain precisely correlated FM and TEM images to guide our Cryo-ET data collection. With this imaging platform, we can consistently localize the microtubule organizing center (MTOC), which forms a single punctum expanding approximately a micron in mammalian cells (Lukinavičius et al. 2014). We are able to show the fluorescent intensity increases initially during

rough milling as the absorptive support film, which is located between the optical microscope objective and the fluorescently labelled sample, is removed (Dahlberg et al. 2022). This brightness gradually decreases as we mill out of focus fluorescence away and dims rapidly as we begin to remove the MTOC structure. As the lamella thickness approaches one micron or less, we are often able to resolve two individual centrioles. Two centrioles correlate precisely with areas showing strong fluorescent signals. This imaging platform opens new possibilities for future work on direct visualization of a wide range of cellular structures that are challenging to localize with current technologies.

## 2.2 PROTOCOL

NOTE: The ENZEL system is a customized instrument and currently not commercially available.

**1. Setup**

1. Cool down the system to cryogenic temperature, which can be accessed by readings from two temperature sensors with one located on the sample stage, and another one inside the chamber. The sample stage is kept at 20°C higher than the chamber temperature (approximately -190°C) to reduce ice contamination. This cooling process on average takes 1.5 hours.

**2. Sample loading**

1. When the sample stage approaches cryogenic temperature (approximately –167.5°C), manually cool down the transfer station with liquid nitrogen.
2. Load one frozen Cryo-EM grid to the sample cassette located on the transfer station.
3. Attach the transfer station to the system and load the sample cassette directly onto the

sample stage guided by a camera.

**3. Sample coating with gas injection system (GIS)**

1. Open Odemis (Delmic) software and move the sample stage from the **Loading** to **Coating** position.
2. Insert the GIS needle in xT Microscope (ThermoFisher) Control from the drop-down manual.
3. Open the gas flow to allow GIS deposition for 30 seconds. Depending on sample type, this may vary arranging from 20 seconds to 1 minute. The goal of this step is to achieve sufficient protection of the sample from the subsequent FIB milling procedure.
4. Retract the GIS needle and move the sample stage back to the **Loading** position.

**4. Three-beam system alignment**

1. Move the sample stage from the **Loading** position to **3-beam** position.
2. Go back to xT Microscope Control and click on the top left window to set the SEM at magnification of 100x.
3. Take an atlas of the grid in Odemis under Alignment tab by clicking the View button. This acquired image is taken based on parameters set in the previous step.
4. Identify a squared area with broken carbon film, and then double click on that area to move the sample stage to desired location.
5. Go back to xT Microscope control and adjust the SEM to a higher magnification to focus on the identified squared area centered in the field of view.
6. Repeat step 4-5 to fine adjust the stage position until SEM is focused on a distinguishable

pattern. For example, the sharp edge of a broken carbon film.

7. Turn on the fluorescent microscope component (FM) to match the view observed under the SEM by adjusting x, y, z coordinates.
8. Make a small pattern with the FIB, for instance, a small rectangle or circle.
9. Identify this pattern under the FIB and FM and adjust the alignment by following step 3-7 if necessary.
10. No further alignment or registration of the optical and ion microscopes is necessary.

**5. Target localization and milling**

1. Move on to Localization tab in Odemis, set up fluorescent channels by activating proper filtered wavelength. Each color should be read as one fluorescent channel with an additional channel for transmitted light (or brightfield).
2. Tune the laser power and exposure time for each fluorescent channel to identify the target of interest. As a reference, we typically expose the sample for 1.2 seconds with a constant LED power setting of 30mW for the SiR-tubulin marker. Parameters may vary between fluorescent channels, but anything resulting in less than ~25-50 $W/cm^2$ of optical intensity at the sample should be suitable. Greater than this can result in significant heating and devitrification of the sample (Dahlberg et al. 2022, Last et al. 2023).
3. Once satisfied, take a pre-milling fluorescent image stack to go through the axial direction above and below the focus. Then, make the target as a ROI.
4. Go back to xT microscope control to set up a lamella at the ROI.
5. Start rough milling to remove the bulk of material approximately 3 μm above and below the ROI. Meanwhile, keep the FM on to monitor any decrease in fluorescent signal.

6. Thin down the ROI to 2µm using cleaning cross section mode and open the interferometric toolkit to monitor the fluorescent signal while thinning the lamella (Sica et al. 2024).
    a. If the target is significantly larger than the target lamella thickness, use rapid decrements in the fluorescence intensity to determine if the milling direction should be switched, i.e., if milling from the bottom up when a significant decrease in fluorescence intensity is observed, then stop milling and mill from the top down in cleaning cross section mode. Continue milling in this way until the desired lamella thickness is achieved.
    b. If the fluorescent object of interest is roughly the final target size of the lamella or smaller, mill from the top down through a test target and note the fringe contrast observed by the interferometric software prior to milling through the target. In future targets, use the interferometric software to predict the appropriate trough in fluorescence brightness to stop at when milling from the top down. The goal is to stop when the object is a distance equal to half the desired lamella thickness below top milling surface. Once milling from the top is completed, produce the final lamella by milling bottom up in cleaning cross section mode until the desired thickness is produced.
7. Take a post-milling fluorescent image.

**6. Correlative light microscopy and tilt series collection**

1. After transferring the sample to Cryo-TEM, collect an atlas overview of the grid.

2. At an appropriate intermediate magnification, collect a single projection of the final lamella at 0-degree tilt.
3. Read 1) the post-milling multi-channel fluorescent images and 2) the projection image from step 2 above into a customized toolkit (compatible with MATLAB version R2023b) for ROI registration.
4. Pick a total of 8-10 pairs of reference points for precise computation of a projective image transformation. These points can be obvious features (e.g., lamellae edges, visible ice contamination, or open grid holes) that are present in both brightfield optical microscopy and the electron microscopy.
5. This overlaid FM-TEM image can be used as a reference for users to select an imaging area within limit of camera frame size for high magnification tilt-series collection. Magnification and parameters of the tilt-series should be selected accordingly based on the biological question. For demonstration, we collected data from plus minus 54 degree with 2-degree increments at a pixel size of 3.465 Å (Kremer et al. 1996, Mastronarde 2005, Mastronarde and Held 2017).

## 2.3 REPRESENTATIVE RESULTS

We labeled differentiated macrophage cells with a tubulin marker, SiR-tubulin, prior freezing. Following the protocol, we successfully identified the MTOC as a single punctum expanding 1 μm under the FM (Fig. 2-1A). We also observed some fibril-like fluorescent signals radiating from the MTOC to the cell periphery as an indication of microtubule networks (Fig. 2-1A). Snapshots from stepwise milling at different specimen thickness was recorded in Fig. 1B. Interestingly, we observed the single MTOC punctum was separated into two adjacent speckles when we reached a thickness

of 800 nm, with each approximately 700 nm in diameter. This signal separation was also captured in the SiR brightness profile (Fig. 2-1C): the single MTOC punctum displayed as a broad peak in the SiR brightness profile which was clearly separated into 2 peaks at 800 nm and was retained till the final sub-200 nm lamella was produced (Fig. 2-1B-C).

Simultaneous viewing and milling allow us to monitor changes in fluorescent brightness. Intriguingly, we observed an increase in fluorescent intensity after the bulk non-fluorescent materials were removed (Fig. 2-1B-D). We observed a sharp decrease in fluorescence intensity when thinning from 2 μm to 800 nm as we milled away fluorescent signals and continued to decrease when sub-200 nm was achieved (Fig. 2-1B-D).

The correlated FM image and TEM atlas indicated centrioles displayed high fluorescent signal, suggesting our workflow can provide precise guidance for targeted milling (Fig. 2-2A). Reconstructed tomograms and segmented models showed centrioles are composed of triplets of microtubules (Fig. 2-2A-B) (Kremer et al. 1996, Mastronarde and Held 2017, Heebner et al. 2022, Meng et al. 2023). In other cases where we only preserve one centriole on the final lamella, we can resolve one centriole in the final tomogram reconstruction (Fig. 2-2B). However, we are not able to resolve the orientation of centrioles by fluorescence (Fig. 2-2B).

## 2.4 DISCUSSION

This workflow provides a possibility to precisely target small and rare biological specimens *in situ* guided by fluorescence. The tri-coincident imaging platform enables simultaneous viewing and milling. This unique feature not only reduces intricate stage movements during milling but by

enabling fluorescence monitoring in real time while milling, challenging steps of registration are avoided. The interferometric guidance further enhances the targeting precision for challenging biological specimens. Meanwhile, high-resolution optics also facilitates target localization in the process of lamella generation. For instance, we showed signal separation from two centrioles occurred when lamellae reached 800 nm or less.

Our customized image transformation software makes correlation possible at the TEM in low magnification overviews of lamella that can be used to guide Cryo-ET data collection specifically to a region-of-interest. This workflow is vital for imaging small and rare biological targets as it could be very challenging to identify those subtle features at the atlas magnification under Cryo-TEM. The precise correlation analysis provides high confidence to include region-of-interest within the imaging frame, which could be only several microns extent.

High targeting precision comes with a cost in efficiency. Instead of automated milling, our manual workflow limits the throughput of lamella generation. Within an 8-hour milling session, we can produce 6-8 lamellae and on average 5 of them containing a target-of-interest. However, we believe this workflow can provide insights for the field to achieve high targeting precision in an automated fashion using future tri-coincident milling systems.

## 2.5 ACKNOWLEDGMENTS

We would like to acknowledge funding sources for the support of this research. P.D.D. was supported in part by the Panofsky Fellowship at the SLAC National Accelerator Laboratory as part of the Department of Energy Laboratory Directed Research and Development program under

contract DE-AC02-76SF00515 and by Department of Energy, Office of Science, Office of Biological and Environmental Research, under Contract No. DE-AC02-76SF00515 FWP 100883. J.W. was supported by grant 2021-234593 from the Chan Zuckerberg Initiative DAF, an advised fund of Silicon Valley Community Foundation.

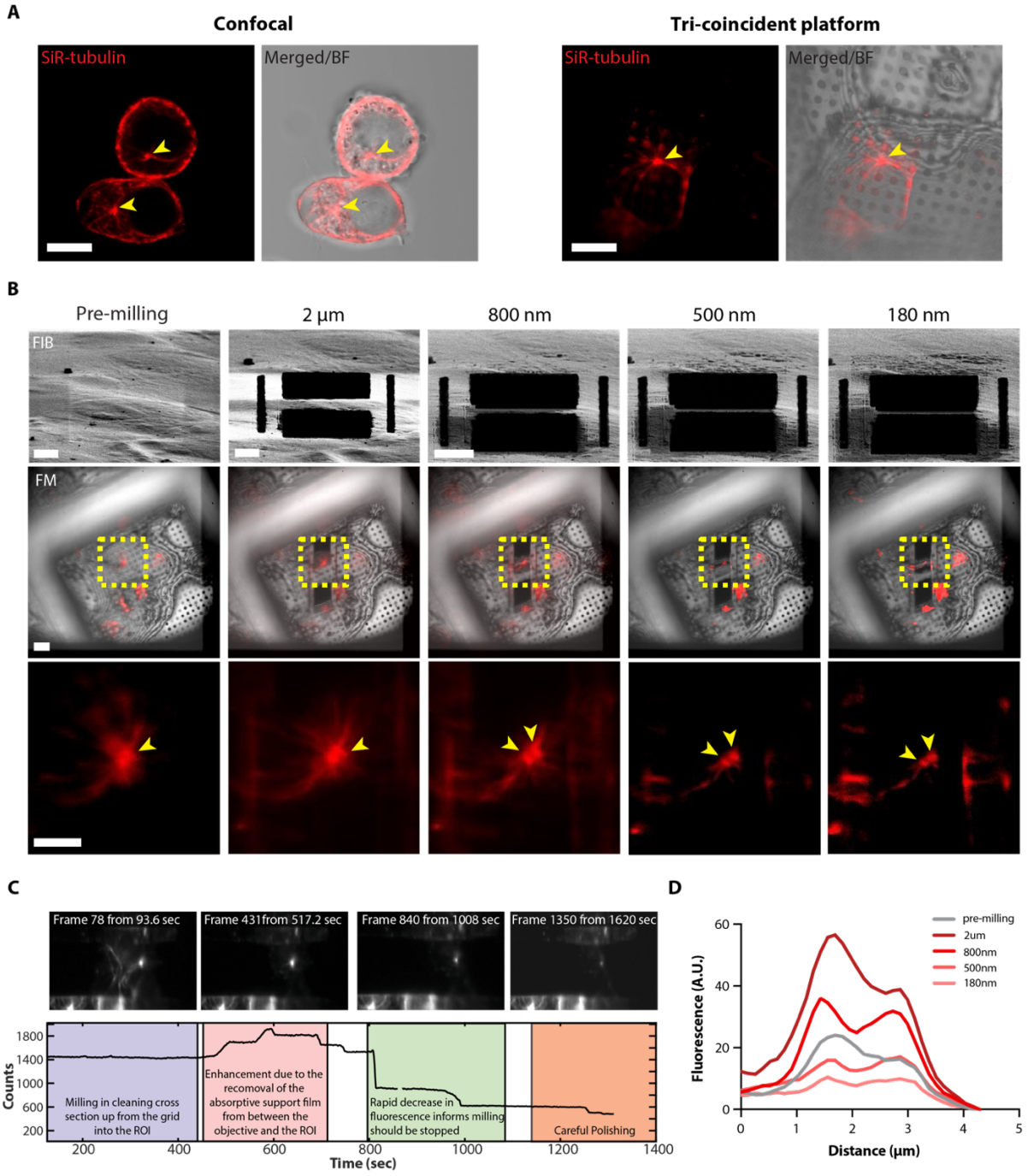


**Figure 2-1. Workflow of tri-coincident cryo-FM-FIB-SEM for precise localization of the microtubule organizing center. (A)** Live cell microscopy and cryo-FM of the MTOC. Scale bar = 10 µm. **(B)** Stepwise snapshots of cryo-FM and cryo-FIB for targeted milling. Close-up FM view is indicated as yellow dashed boxes. Centrioles are marked as yellow arrows. Scale bar = 5 µm. **(C)** Fluorescence intensity profile of cryo-FIB milling. **(D)** Fluorescence brightness profile of cryo-FIB milling.

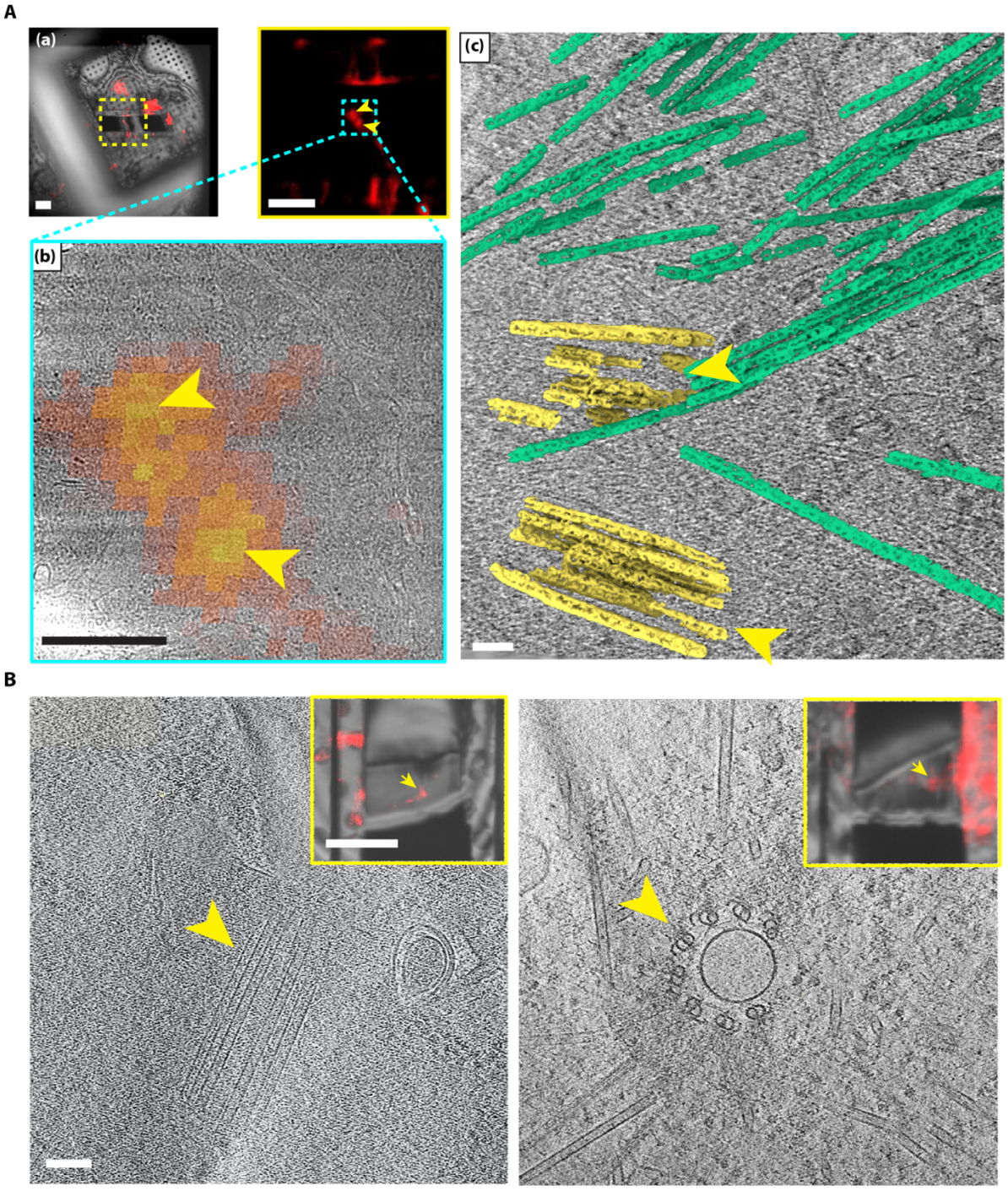


**Figure 2-2. Tri-coincident cryo-FM-FIB-SEM workflow reveals molecular details of the MTOC. (A)** Correlated FM, EM, and segmentation model of the MTOC. (a) Post-milling FM image. This is the same image from the last panel of Fig. 1B marked as 180 nm. Scale bar=5 μm; (b) Correlated FM and TEM projection. Scale bar=1 μm. (c) Segmented model of tomographic reconstruction at the region of interest (yellow, centriole; green, microtubule). Scale bar=100 nm. **(B)** Representative FM image and tomographic slices showing orientations of the MTOC. FM: Scale bar=5μm. Tomographic slice: Scale bar=200 nm.

*Chapter 3*

# MOLECULAR ARCHITECTURE OF THE MICROTUBULE ORGANIZING CENTER

## ABSTRACT

The microtubule organizing center (MTOC) is an organelle regulating cell division and cellular transport that consists of centrioles, the surrounding pericentriolar material (PCM), and nucleated microtubule (MT) filaments. The primary MTOC in mammalian cells is the centrosome, and abnormal centrosomal activities are linked to diverse human diseases. A full understanding of centrosome organization and microtubule nucleation will likely provide new therapeutic opportunities, but today there is limited information on MTOC architecture *in situ*, partially due to the lack of an established workflow for high-resolution imaging small and rare protein complexes in eukaryotic cells. Here we visualized the MTOC in human macrophages by fluorescence-guided cryogenic focused ion beam milling (cryo-FIB-SEM) and cryo-electron tomography (cryo-ET). Consistent with previous reports, we observed that centrioles are organized as nine triplets of MTs surrounded by approximately 150-nm thick amorphous pericentriolar material. We also saw that MTs nucleate from the PCM at various angles with no obvious preferred orientation. Cryo-tomograms also showed MTs anchored to the PCM via tethering proteins, including at various stages along the nucleation process.

## 3.1 INTRODUCTION

Cells rely on their cytoskeleton to maintain their morphology, move, and divide. The MTOC is the main organizing center for microtubules (MTs) (Sanchez and Feldman 2017, Jana 2021). In animal somatic cells, the main MTOC is known as the centrosome (Carvalho-Santos et al. 2011, Conduit et al. 2015, Sanchez and Feldman 2017, Breslow and Holland 2019, Jana 2021). It is a membrane-less organelle located in the perinuclear region of the cell, and it plays essential roles in cell division and cellular transport (Carvalho-Santos et al. 2011, Conduit et al. 2015, Sanchez and Feldman 2017, Breslow and Holland 2019, Jana 2021). Recent evidence suggests the centrosome can also modulate immune response (Kumar et al. 2014, Vertii, Ivshina et al. 2016, Qi and Zhou 2021, Weier et al. 2022, Schapfl et al. 2024). Dysregulation of centrosomal activity has been associated with abnormal cell growth and several epithelial cancers (Pancione, Cerulo et al. 2021, Qi and Zhou 2021).

The centrosome consists of two centrioles, the surrounding pericentriolar material (PCM), and associated MTs (Carvalho-Santos et al. 2011, Jana et al. 2014, Laporte et al. 2024, Tollervey et al. 2024). In interphase cells, the two centrioles are perpendicular to each other and are ~500 nm long and ~200 nm wide (Carvalho-Santos et al. 2011, Jana et al. 2014, Winey and O'Toole 2014, Laporte et al. 2024, Tollervey et al. 2024). Structural analysis of isolated centrosomes by cryogenic electron tomography (cryo-ET) showed barrels of nine MT triplets (Busselez et al. 2019, Li et al. 2019, Guichard et al. 2020, Li et al. 2023, Tollervey et al. 2024). The centrioles are surrounded by an amorphous PCM composed of hundreds of proteins. Studies have shown that PCM accumulates as a phase-separated compartment (Gould and Borisy 1977, Woodruff et al. 2014); however, there are very few available structural details regarding the PCM because it is usually

absent in purified or isolated systems (Busselez et al. 2019, Li et al. 2019, Li et al. 2023, Tollervey et al. 2024).

Microtubule organization is a critical function of the MTOC. It has been reported that MTs are anchored to the PCM via a γ-tubulin ring complex (γ-TuRC) (Tovey and Conduit 2018, Brilot, Lyon et al. 2021, Dendooven, Yatskevich et al. 2024). High-resolution structures of purified γ-TuRC showed a helical array of γ-tubulin assembled into a conical complex (Kollman et al. 2011, Zimmermann et al. 2020, Würtz et al. 2022). However, little has been done *in situ* to show how γ-TuRC interacts with PCM, and it remains unclear how the MTOC directs microtubule nucleation. Recently, more information has been obtained from the intact MTOC structure in mammalian cells. One study provided an elegant time-series analysis on the MTOC architecture using expansion microscopy (Laporte et al. 2024). This study involved molecular mapping of more than 20 centriolar proteins during centriole biogenesis, including proteins known to be part of PCM (Laporte et al. 2024). Cryo-ET has recently began allowing macromolecular complexes, such as the MTOC, to be visualized directly *in situ*. A recent cryo-ET study captured the MTOC structure in *C. elegans* at various stages of cell division (Tollervey et al. 2024). However, none of the reported cryo-tomograms showed complete centriole structure (Tollervey et al. 2024). One challenge has been preserving centrioles, which is a small and only one or two copy per cell, within lamellae thin enough for imaging. This problem has been overcome by the development of the ENZEL cryo-FM-SIB-SEM system elaborated in the previous chapter. In this study, we applied fluorescence-guided cryo-FIB-SEM and subsequent cryo-ET to visualize the molecular architecture of the MTOC in human macrophages, and we established a model of the MTOC based on cellular details

observed in cryo-tomograms. We also analyzed how MTs anchor to the PCM, providing an improved understanding of the molecular architecture of the MTOC and MT organization.

## 3.2 RESULTS

### The molecular architecture of the MTOC in human macrophages

We used a fluorogenic dye, SiR-tubulin, to chemically label beta-tubulin in human macrophages differentiated from THP-1 cells. SiR-tubulin emits in the far-red region of the visible light spectrum, and live cell imaging showed the MTOC as a single punctum ~1 μm wide. Some additional signal radiated from the punctum, likely arising from the surrounding microtubule networks (Fig. 3-1A). A similar phenotype was observed at cryogenic temperatures (Fig. 3-1A). We used the ENZEL to image the MTOC punctum following the protocol reported in Wang et al. (Chapter 1) (Sica et al. 2024). An overlay of the FM images and corresponding segmentation models showed the highest fluorescence intensity correlated precisely with centrioles (Fig. 3-1B) and the low fluorescence intensity correlated with peripheral MT networks (Fig. 3-1B).

Cryo-tomograms of the MTOC were obtained from 11 interphase cells and revealed the features of centrioles and their surrounding MT networks. We found that MTs were nucleated ~200 nm away from the centrioles (Fig. 3-1C). Because previous studies have shown that MTs are nucleated from PCM, we believe the space between the MT nucleation sites and the centriole is filled with PCM, which is not clearly resolved in cryo-tomograms. Indeed, current cryo-ET studies on the centrosome do not show clear structural features in PCM (Li et al. 2023, Tollervey et al. 2024). Each centriole in the present study was organized in a barrel structure with 9 triplets of microtubules, consistent with previous studies on isolated MTOCs in eukaryotes (Busselez et al.

2019, Li et al. 2019, Guichard et al. 2020, Li et al. 2023, Tollervey et al. 2024). MT triplets are composed of three protofilaments called the A-, B-, and C-tubules (Fig. 3-1C). We resolved the A-tubule to be a ring of 13 MT protofilaments and the B-tubule to be a ring of 10 protofilaments. The C-tubule in the mother centriole is known to be highly flexible, and we saw no intact ring structure (Fig. 3-1C). The diameter of each MT protofilament observed was ~4 nm, comparable to the reported value of tubulin (Tollervey et al. 2024). There was a small number of incomplete centrioles with eight MT triplets instead of nine (Fig. 3-1C). The absent MT triplet is not due to milling since the direction of the centrioles is perpendicular to the ion beam. Therefore, there were only eight MT triplets (Fig. 3-1C).

Because the centriole structure in mammalian cells has been reported to be ~500 nm long and ~200 nm wide, it is difficult to preserve two complete centriole structures in the same sub-200-nm-thick lamella. From all three cryo-tomograms containing both centrioles, the two centrioles were oriented perpendicularly to each other and were approximately 500 nm apart (Fig. 3-1C). Among all cells analyzed in this study, we observed both side view and top view of centrioles. We could not detect the centriole orientation during cryo-FIB milling as both views exhibited a single punctum (Fig. 3-1D). Centrioles were on average, 257 nm in diameter, but they varied in length, ranging from 380 to 645 nm (Fig. 3-1E-F). The variance in length could potentially be due to the limitation in lamella thickness.

Interestingly, we found a hollow vesicle-like structure in the center of the centriole barrel (Fig. 3-1C). Previous studies on isolated centrioles showed DNA was sometimes present in the centriole barrel (Busselez et al. 2019), however, this vesicle-like structure is different (Li et al. 2023). We

also ruled out the possibility of the novel ring density complexes reported in Li et al. since they are different in size and relative location. We also observed a faint density connecting the structure to the MT triplets which is not present in previous reported structures obtained from isolated systems (Fig. 3-1C) (Busselez et al. 2019, Li et al. 2019).

### Nucleating microtubules are anchored to PCM via tethering proteins

The γ-TuRC has a distinctive asymmetrical conical shape, and we observed a similar structure at the end of every MT in our cryo-tomograms (Fig. 3-1C, Fig. 3-2A). Interestingly, we observed some heterogeneity at the tip of the γ-TuRC. A small portion of MTs (~19%) displayed extra densities at the tip, indicating the presence of other tethering proteins (Fig. 3-2A). In addition, we also observed rare cases of incomplete γ-TuRC with a small open gap at the tip (Fig. 3-2A). Previous studies in yeast reported that tethering proteins organize into an ordered bundle-like structure, but in human macrophages the tethering proteins appear amorphous or highly flexible (Fig. 3-2A) (Kollman et al. 2011, Brilot et al. 2021). We further quantified the length of MTs in each class of nucleation sites and noticed the class with an open end appears shorter in length compared to other two classes (Fig. 3-2B). We speculate that this difference suggests that γ-TuRC is in the process of assembling and that the complex is fully assembled in other classes.

## 3.3 DISCUSSION

Our study provides a direct observation of the MTOC molecular architecture in mammalian cells *in situ*. Our results support the model of the MTOC architecture reported in previous studies. We showed the centrioles are spatially perpendicular to each other in interphase. Each centriole is ~250 nm in diameter and 500 nm in length and is organized in a barrel structure with 13 microtubule

triplets. Centrioles are surrounded by a 150-nm layer of PCM composed of a myriad of proteins. This layer of proteins displays unexpectedly low contrast in cryo-ET, indicating proteins involved in this region may be flexible or unorganized. Similar observations have been reported in other studies where PCM does not show distinguishable features (Li et al. 2023, Tollervey et al. 2024). Notably, previous studies pointed out the PCM is a dynamic assembly forming a selective phase separated compartment composed of high concentration of tubulin and other effector proteins involved in microtubule nucleation (Zwicker et al. 2014, Woodruff et al. 2017, Jiang et al. 2021). The low contrast in cryo-tomograms potentially indicate cellular feature of a phase separation with high concentration of proteins. Another study done in isolated systems has shown amorphous protein clusters composed of a mixture of PCM proteins, cohesion, and condensin, with high EM contrast inside the centriole barrel (Busselez et al. 2019). However, this feature is absent from our cryo-tomograms, and may be cell-state dependent. We also identified an unknown vesicle-like structure inside the centriole barrel that does not appear to be similar to any reported structures of centrosomal proteins. We speculate that this protein density could come from the SAS-6 proteins required for centriole formation. This protein has been known to be highly conserved in *C. elegans* and human cells (Leidel et al. 2005, Kantsadi et al. 2022). Atomic model of SAS-6 showed coiled-coil complex organized into a ring, forming direct interactions with microtubule triplets (Kantsadi et al. 2022).

We also observed the microtubule nucleation site anchored to the PCM connected by tethering proteins. Previous models suggested the MT nucleation site is composed of γ-TuRC and scaffolding cap proteins, which together lead to the formation of a conically shaped protein complex (Kollman et al. 2011, Zimmermann et al. 2020, Würtz et al. 2022). Structural studies in yeast also showed attachment factors decorate the cap proteins (Kollman et al. 2011, Zimmermann et al. 2020, Würtz

et al. 2022), however, the architecture of MT nucleation sites in mammalian cells remains largely unknown. Our cryo-tomograms showed how MTs are anchored to the PCM via tethering proteins. Notably, previous models obtained in yeast cells demonstrated that all tethering proteins form an ordered bundle connecting to the PCM, whereas in our cryo-tomograms, tethering proteins are highly flexible. We speculate that this heterogeneity depends on functional states of microtubule nucleation, and high-resolution subtomogram averages of this complex can provide *in-situ* insights of how the microtubule nucleation site is assembled.

## 3.4 MATERIALS AND METHODS

### Cell culture

Human monocytic THP-1 cells were maintained in Roswell Park Memorial Institute (RPMI) 1640 Medium (Thermo Fisher Scientific, Cat. No: 11875085), supplemented with heat inactivated 10% FBS and 0.05 mM 2-mercaptoethanol (Thermo Fisher Scientific, Cat. No: 31350010),10 mM HEPES (Thermo Fisher Scientific, Cat. No: 15630080), 1 mM Sodium Pyruvate (Thermo Fisher Scientific, Cat. No: 11360070), 100 units/mL of penicillin and 100 µg/mL of streptomycin. All cells were maintained at 37 °C with 5% CO2 and were differentiated for 48 hours with 100 nM phorbol myristate acetate (PMA, Sigma-Aldrich, Cat. No: P8139–5MG) before experiments.

### Live cell imaging

For visualization of SiR-tubulin in live cells, cells were differentiated and grown in glass bottom dishes (MatTek corporation, Cat. No: P35G-1.5–14-C) for 48 hours. Then cells were first washed once with PBS and the medium was replaced by RPMI 1640 medium with no phenol red (Thermo Fisher Scientific, Cat. No: 11835030) supplemented with 10% FBS, and placed back in the incubator for at least 1 hour. 1 µM SiR-tubulin (Cytoskeleton, Inc., Cat. No: CY-SC002) was used for 1-2 hours to stain the microtubule network in live cells. Live cell images were obtained at 37 °C with 5% $CO_2$.

### Sample preparation for cryo-ET

THP-1 cells were maintained as described in previous section. Cells were differentiated for 24 hours in tissue culture treated plate and seeded onto human fibronectin (25µg/mL in 1xPBS, Advanced Biomatrix, Cat. No: 5050) coated grids (R2/2, Au 200-mesh London Finder grid coated

with extra thick carbon, Electron Microscopy Sciences) for another 24 hours to allow sufficient adherence. Untreated cells were stained by SiR-tubulin only for 4 hours and maintained at 37 °C with 5% $CO_2$. Grids were plunge-frozen in liquid ethane (Airgas) on a MarkIV vitrobot (Thermo Fisher Scientific) at 100% humidity with manual blotting and transferred into liquid nitrogen for long-term storage.

**In-situ fluorescence-guided cryoFIB-SEM milling**

Frozen grids were clipped into AutoGrids with 4 milling slots (Thermo Fisher Scientific) and loaded onto the Ariyscan laser scanning microscope (Zeiss LSM880) equipped with a cryogenic sample stage (Linkam, CMS196) for inspection of MTOC punctum and ice quality. Grids were then transferred to an Aquilos2 Dual-Beam system (Thermo Fisher Scientific) with customized integrated fluorescent light microscope (ENZEL from Delmic) that is coincident with the FIB and SEM of the Aquilos2 as described previously. Organo-platinum (Pt) deposition was applied to grids via the gas injection system (GIS) for 20-30 seconds. The MTOC punctum was observed on the ENZEL system equipped with a 100x long working distance vacuum objective (NA 0.85). Materials above and below the target of interests were ablated accordingly monitored by real-time fluorescence. The stepwise milling was performed as described in previous studies (Wagner et al. 2020, Lam and Villa 2021). In brief, rough milling, thinning, and polishing were done at 0.1nA, 30pA, 10pA at 30kV. Final fluorescent images were taken when the thickness of the lamella was approximately 200nm with the following imaging parameters: MTOC, ~ 0.4 W/cm$^2$ of 625 ± 10 nm with 1-2 seconds exposure; Reflected brightfield, ~0.1 W/cm$^2$ of 470 ± 10 nm with 500 milliseconds exposure.

### Tilt series acquisition guided by correlated fluorescence microscopy

Atlas images and tilt series were acquired on a Titan Krios G2 (Thermo Fisher Scientific) at 300 keV equipped with a K3 Summit detector and BioQuantum post-column energy filter (Gatan) operated in counting and dose fractionation mode with 10 eV slit in. Atlases were collected as joint serial sections at 6,500x magnification under low dose mode in SerialEM software suite (Mastronarde 2003, Mastronarde 2005). Tilt series were collected at a pixel size of 3.465 Å with a total dose of approximately 120-160 e-/Å$^2$, ranging from -48° to 60° to account for a ~6-8° milling angle with 2-degree increment using SerialEM.

### Tomogram reconstruction and quantification of cellular features

Unbinned image frames were preprocessed in Tomo3D with motion correction and assembled to aligned tilt series with a binning factor of 2 (Agulleiro and Fernandez 2011, Agulleiro and Fernandez 2015). Aligned tilt series were reconstructed manually in IMOD at a pixel size of 13.86 Å with 30 iterations of SIRT-like filter following CTF correction (Kremer et al. 1996, Mastronarde and Held 2017). Centriole length and width were measured in rendering mode in IMOD.

### Tomogram segmentation and visualization

Tomograms used for segmentation were imported to Dragonfly 2022.2 and subject to Gaussian filtering to enhance image contrast. Training data sets were prepared by manually segmented 10 slices containing microtubules, large membrane structures, ribosomes, and mitochondria. The Neural Network Model was generated with a dimension of 2.5D and 3 slices. Segmented features were exported independently and later processed in FIJI with Gaussian blurring (sigma=0.8) and imported to ChimeraX (version 1.7.1) for visualization (Schindelin et al. 2012, Meng et al. 2023).

Tomograms with fluorescence overlay were manually segmented in IMOD for microtubules and centrioles.

**Correlated fluorescence microscopy**

Registration of fluorescence and electron tomography data was performed utilizing a customized toolkit compatible with MATLAB version R2023b. Briefly, 16-bit multi-channel fluorescent images obtained from the ENZEL system were firstly correlated to atlases collected at 6500x magnification using obvious features (e.g., lamellae edges, visible ice contamination, or grid holes) present in both brightfield optical microscopy and the electron microscopy. A total of 8-10 pairs of reference points were selected accordingly for precise correlation. These point pairs were used to calculate a projective transformation to carry the fluorescence data to this low magnification EM space. Secondly, a new set of points visible in the registered atlases and in a z-projection of the tomographic reconstruction were selected. These points largely included visible cellular features (e.g., large membrane structure, vesicles, mitochondria, or MTOC). A total of 10-13 pairs of reference points were manually selected for registration and the computation of a similarity transformation to carry the atlas space into the tomography space. Lastly, the projective and similar transformation were serially applied to the fluorescence images to bring the fluorescence images to the tomography space. For visualization, final correlated images containing SiR-tubulin channel were generated by overlaying fluorescent channels with actual tomogram reconstruction ($z = 10$ slices).

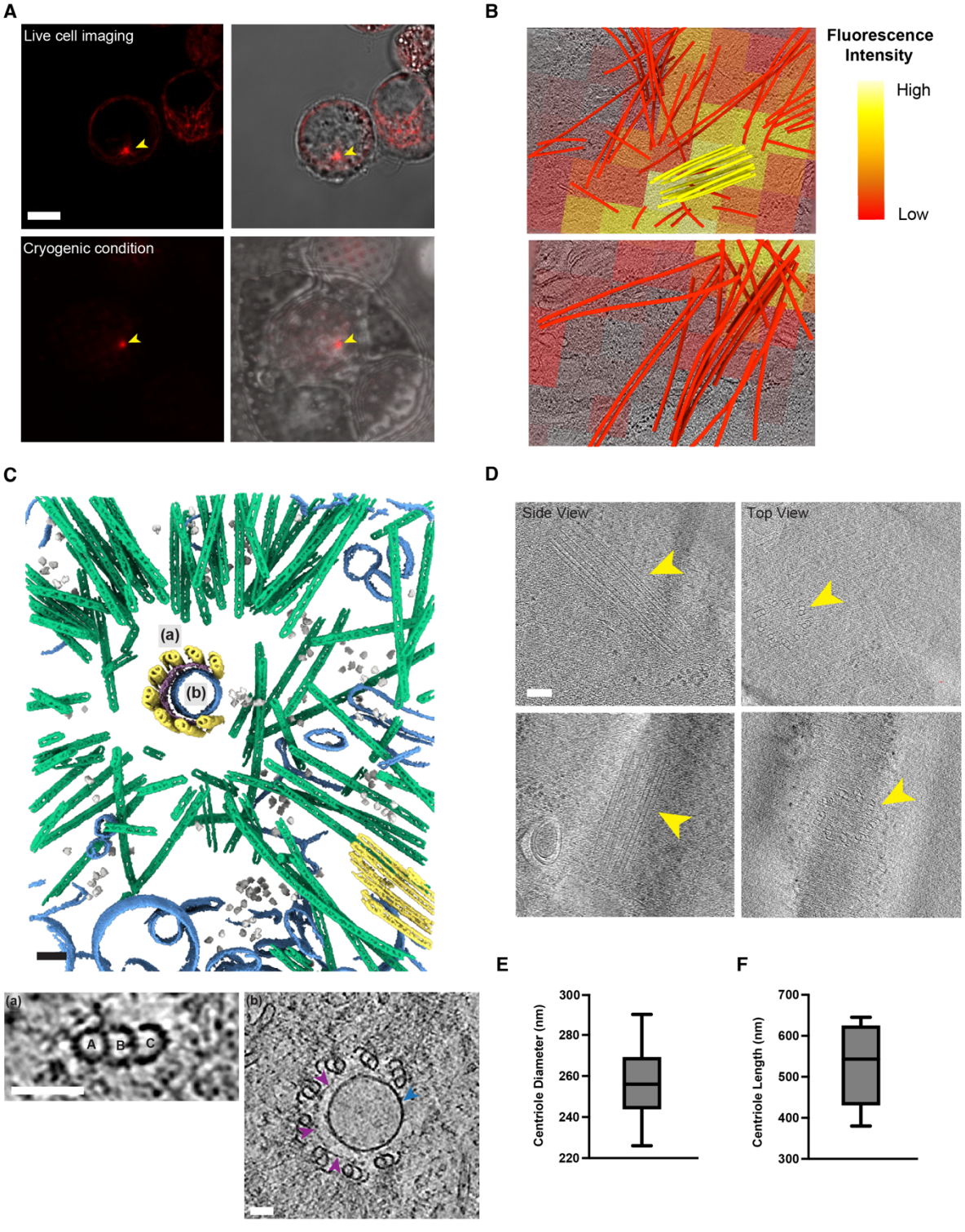
A
Live cell imaging
Cryogenic condition
B
Fluorescence Intensity
High
Low
C
(a)
(b)
A
B
C
D
Side View
Top View
E
Centriole Diameter (nm)
300
280
260
240
220
F
Centriole Length (nm)
700
600
500
400
300

**Figure 3-1. Cryo-ET workflow for direct visualization of the MTOC architecture. (A)** Live cell microscopy and cryo-FM of the MTOC. Scale bar=10 μm. **(B)** Overlaid cryo-FM image superimposed on cryo-tomographic slices with segmentation. Top: tomogram collected "on-target." Bottom: tomogram collected "off-target" (MTOC, yellow; microtubule networks, red). Scale bar=100 nm. **(C)** Segmented model of the MTOC (MTOC, yellow; microtubule networks, green; membrane structures, blue; ribosomes, grey; ring density complex, purple). Scale bar=100 nm; (a) Enlarged view of a MT triplet. Scale bar=50 nm; (b) Enlarged view of a centriole barrel highlighting the ring density complex (purple arrow) and an unknown vesicle structure (blue arrow). Scale bar=50 nm. **(D)** Quantification of centriole diameter (n=11). **(E)** Quantification of centriole length (n=8). Only centrioles presenting a clear side view and entirely contained within the lamella were analyzed.

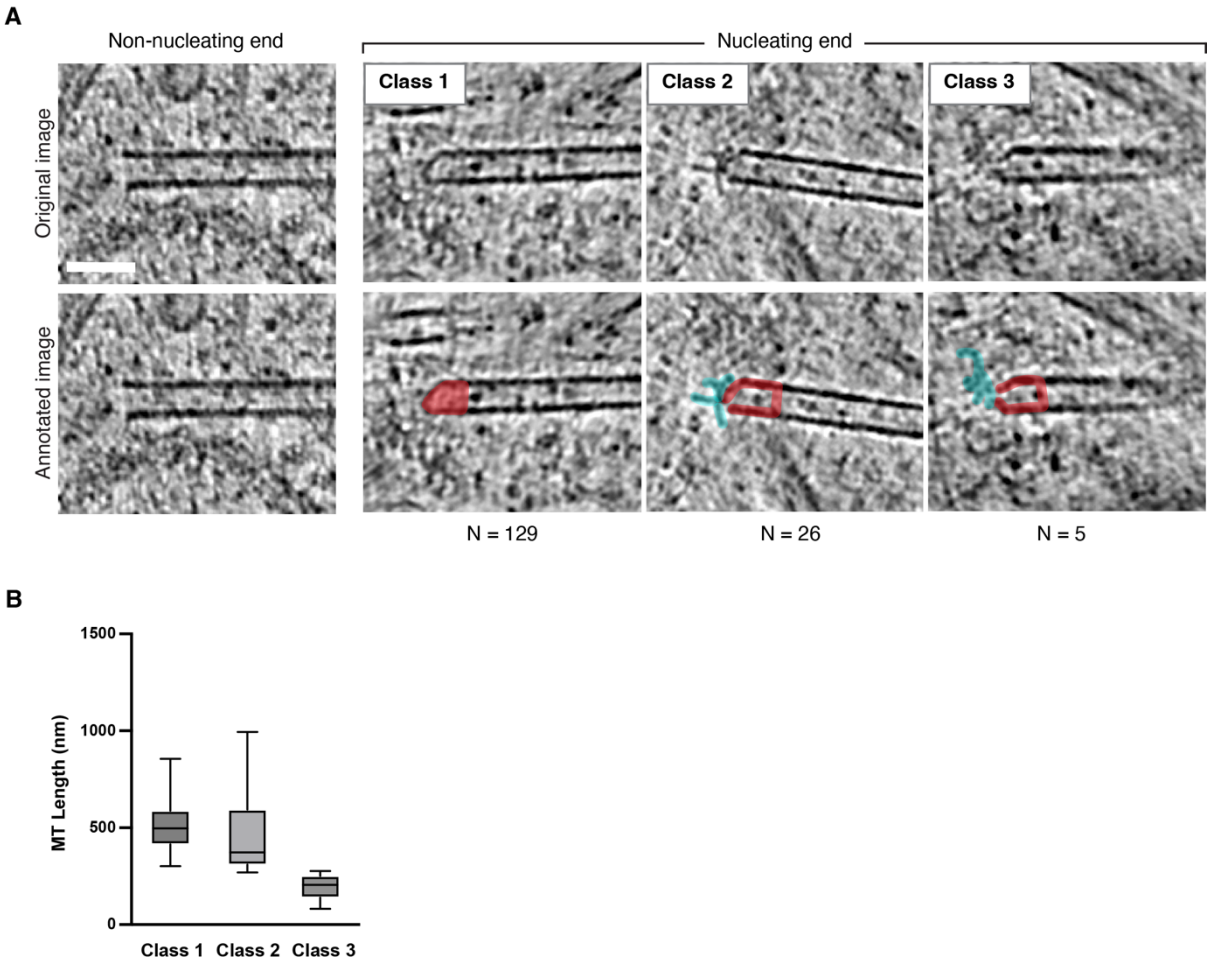


**Figure 3-2. The microtubule nucleation site displays a variety of conformations.** (A) Gallery of MT nucleating ends and non-nucleating ends. For annotation, γ-TuRC, red; tethering proteins, cyan. Scale bar=50 nm. (B) Quantification of microtubule length in each class. Class 1, n=52; class 2, n=12; class 3, n=5.

*Chapter 4*

# HUMAN NLRP3 INFLAMMASOME ACTIVATION LEADS TO FORMATION OF CONDENSATE AT THE MICROTUBULE ORGANIZING CENTER

*Adapted from:*

Jue Wang, Man Wu, Venkat G. Magupalli, Peter D. Dahlberg, Hao Wu, and Grant J. Jensen. "Human NLRP3 inflammasome activation leads to formation of condensate at the microtubule organizing center." Manuscript is under review.

## ABSTRACT

The NLRP3 inflammasome is a multi-protein molecular assembly that mediates inflammatory responses in innate immunity. Its dysregulation has been linked to a large number of human diseases. Here, we used cryogenic fluorescence-guided focused ion beam (cryo-FIB) milling and electron cryo-tomography (cryo-ET) to obtain 3D images of the NLRP3 inflammasome in human macrophages in situ at various stages of its activation. The cryo-tomograms at macromolecular resolution revealed unexpectedly dense condensates within and around the microtubule organizing center (MTOC). We also found that following NLRP3 priming and activation, the Golgi cisternae expand and disperse while 50-nm NLRP3-associated vesicles appear. These vesicles likely ferry NLRP3 to the MTOC. At a later stage after activation, we saw that the electron-dense condensates progressively solidified and the cells underwent pyroptosis with widespread mitochondrial damage and autophagy.

## 4.1 INTRODUCTION

Canonical inflammasomes are cytoplasmic complexes responsible for detecting infections and cellular distress (Schroder and Tschopp 2010, Swanson et al. 2019, Fu and Wu 2023). Upon activation, these multi-protein complexes assemble into supramolecular structures that activate pro-caspases, release proinflammatory cytokines, and eventually cause pyroptotic cell death (Schroder and Tschopp 2010, Swanson et al. 2019, Fu and Wu 2023). One of the most extensively studied members of this family, the NLRP3 inflammasome, is composed of an NLRP3 sensor protein (also known as cryopyrin), an apoptosis-associated speck-like protein containing a C-terminal caspase recruitment domain (ASC) adaptor, and a pro-caspase-1 effector (Broz and Dixit 2016, Gaidt and Hornung 2018, Swanson et al. 2019, Fu and Wu 2023). Early studies revealed that germline mutations and hyperactivity of NLRP3 are associated with rare hereditary autoinflammatory diseases in humans (Zahid et al. 2019, Wang et al. 2020, Que et al. 2024). NLRP3 has also now been implicated in the development of many common diseases including Parkinson's disease, Alzheimer's disease, cardiovascular diseases, and age-related metabolic complications (Zahid et al. 2019, Wang et al. 2020, Wu et al. 2022, Fu and Wu 2023, Que et al. 2024).

In macrophages, activation of the NLRP3 inflammasome involves two steps. In the first step (priming), Toll-like receptors (TLRs) on the cell surface recognize pathogen-associated molecular patterns (PAMPs) or damage-associated molecular patterns (DAMPs). This leads to the production of inflammasome proteins, including NLRP3 and the precursor of proinflammatory cytokine IL-1β (Broz and Dixit 2016, Gaidt and Hornung 2018, Swanson et al. 2019, Fu and Wu 2023). In the second step of activation, extracellular ATP, bacterial toxins like nigericin, or other

molecules induce cellular $K^+$ efflux and NLRP3 activation. Active NLRP3 recruits ASC, which is thought to polymerize and thereby cause caspase-1 processing via proximity-induced dimerization and self-cleavage (Schroder and Tschopp 2010, Broz and Dixit 2016, Swanson et al. 2019, Fu and Wu 2023, Xiao et al. 2023). Active caspase-1 cleaves the precursors of IL-1β and IL-18, leading to their maturation (Dong et al. 2024). Active caspase-1 also cleaves the pore-forming protein gasdermin D (GSDMD), which then forms pores in cytoplasmic membranes that release the processed cytokines and induce pyroptosis (Lieberman et al. 2019).

By fluorescence microscopy, the NLRP3 inflammasome is seen as a single speck within each cell (Hornung et al. 2009, Wu et al. 2010, Magupalli et al. 2020). Some of us (Magupalli et al. 2020) and others showed previously that this single speck contains the caspase-1 holoenzyme and colocalizes with the microtubule organizing center (MTOC) (Li et al. 2017, Magupalli et al. 2020, Wu et al. 2022). Many *in vitro* structures of purified components and reconstituted sub-assemblies are already available, including cryo-EM structures of inactive monomeric NLRP3 (in complex with NEK7) (Sharif et al. 2019, Yu et al. 2024), inactive oligomeric NLRP3 in cage form (Andreeva et al. 2021, Hochheiser et al. 2022, Ohto et al. 2022), active NLRP3 in disc form (in complex with NEK7 and ASC) (Xiao et al. 2023), and the pyrin domain (PYD) and caspase-recruitment domain (CARD) filaments of ASC (Lu et al. 2014, Sborgi et al. 2015, Li et al. 2018).

A recent *in situ* cryo-ET study of ASC-overexpressing mouse immortalized bone-marrow-derived macrophages (iBMDMs) (Stutz et al. 2013) revealed networks of ASC filaments (Liu et al. 2023), but the significance to inflammasome structure remains unclear for the following reasons: while the inflammasome speck forms at the MTOC in wildtype iBMDMs, they do not in the ASC-

overexpressing cells (Magupalli et al. 2020). Additionally, many organelles have been associated with NLRP3 activation, including mitochondrial damage (Zhou et al. 2011, Mishra et al. 2021, Xian et al. 2022), Golgi cisternae dispersion, and endosomal trafficking disruption (Lee et al. 2023, Zhang et al. 2023), which were not reported in the recent study (Liu et al. 2023). In recent years, it has also become evident that human and mouse NLRP3 may employ different mechanisms for their activation (He et al. 2016, Schmid-Burgk et al. 2016, Shi et al. 2016, Schmacke et al. 2022). Notably, while mouse cells require NEK7 for NLRP3 activation and speck formation (He et al. 2016, Schmid-Burgk et al. 2016, Shi et al. 2016), priming alone results in NLRP3 activation in human cells independent of NEK7 (Schmacke et al. 2022). NEK7 is a centrosomal kinase important for mitosis, but its function in mouse cells is not dependent on its kinase activity, only its scaffolding function. Thus, it remains imperative to investigate NLRP3 activation in human cells.

Cryo-FIB milling and cryo-ET have become powerful techniques to visualize protein complexes in their near-native state *in situ* to macromolecular resolution (Hampton et al. 2017, Wu et al. 2020). Previous studies have successfully targeted certain organelles and large protein aggregates by fluorescence (Carter et al. 2020, Wu et al. 2020, Liu et al. 2023). However, guidance of the milling along the axis of the microscope remains challenging for small and rare structures, including the MTOC and NLRP3 inflammasome, due to motion of the sample that occurs during the transfer of the sample from the cryogenic light microscope to the FIB-SEM and registration errors during the milling process itself. These challenges persist even when the light microscope is integrated into the FIB-SEM vacuum chamber due to the common configuration of the optical imaging position and the milling position being in two separate regions of the vacuum chamber. As a result,

small targets are nearly always lost during milling without precise localization (Arnold et al. 2016, Fu, Ning et al. 2019, Yang et al. 2021, Liu et al. 2023). Here we employed a new, tri-coincident cryo-FIB-SEM-fluorescence instrument (Boltje et al. 2022), called the ENZEL, to overcome these challenges. The ENZEL allows real-time simultaneous fluorescence and cryo-FIB to guide the milling. Using the ENZEL and then cryo-ET to image the milled lamellae, we visualized multiple NLRP3 inflammasomes directly *in situ* at the MTOC in human macrophages during various stages of activation. The images revealed new insights into the NLRP3 structure and organelle alterations that occur during inflammation.

## 4.2 RESULTS

### Fluorescence-guided cryo-FIB milling

In order to find the NLRP3 inflammasome (hereafter referred to as simply the inflammasome) *in situ* and guide the FIB-milling process, we first constructed a human THP-1 monocytic cell line in which the endogenous NLRP3 was knocked out. We added the NLRP3 gene fused to the fluorescent protein mScarlet to the cell line, referred to as mSL-NLRP3 cells (Fig. 4-S1A). Monocytic cells were then differentiated into macrophages. This macrophage cell line recapitulated all the hallmark behaviors of wildtype inflammasome activation: after priming with LPS and activating with nigericin, we observed ASC speck formation, GSDMD processing, and cell death as shown by LDH release (Fig. 4-S1B–D). These effects were seen in wildtype and mSL-NLRP3 cells, but not in the parent NLRP3 knock-out cells, confirming the dependence of the processes on NLRP3 (Fig. 4-S1B–D). Because we wanted the milling process to be guided in real time by fluorescence with multiple color channels (Boltje et al. 2022), we also added SiR-tubulin to mark the MTOC (Lukinavičius et al. 2014), such that untreated cells would show only SiR-

tubulin signal (Fig. 4-S1E, F). In live cells, we observed no NLRP3 punctum formation before priming (Fig. 4-S1E). Addition of lipopolysaccharides (LPS), which activate TLR4, led to the formation of a diffused NLRP3 signal covering the region where the MTOC is located (Fig. 4-S1E). We then added nigericin, a potassium ionophore frequently used to activate NLRP3 (Muñoz-Planillo et al. 2013, Lamkanfi and Dixit 2014), and observed a NLRP3 fluorescent signal colocalized with the MTOC fluorescence, as seen in other inflammasome studies (Fig. 4-S1E, G) (Li et al. 2017, Magupalli et al. 2020, Wu et al. 2022).

To prepare samples for cryo-ET, we used the ENZEL tri-coincident cryo-FM and cryo-FIB-SEM platform to mill ~200-nm-thick lamellae (Boltje, Hoogenboom et al. 2022) within cells at various time points before and after priming and activation. Similar to the results from live cell imaging, primed cells exhibited both mScarlet (NLRP3) and SiR-tubulin signals. Addition of nigericin to primed cells caused the mScarlet fluorescence to condense into a single bright punctum colocalized with the MTOC (Fig. 4-S1F, Fig. S2). In every cell investigated in this study, both live and frozen, the NLRP3 puncta colocalized with the MTOC (Fig. 4-S1G). Using this tri-coincident cryo-FIB-milling system, 52 of the 82 total milled lamellae retained the target of interest, as seen by fluorescence of the final lamellae and cryo-ET.

**NLRP3 accumulates into a condensate at the MTOC**

The brightest SiR-tubulin fluorescence correlated precisely with centrioles in the cryo-tomograms, unambiguously marking the MTOC (Fig. 4-1A–B). In nigericin-stimulated cells, but not in untreated or only LPS-primed cells, an electron-dense region containing irregular patch-like densities and small vesicles was seen between and around the centrioles, expanding to

approximately 2 μm in diameter, (Fig. 4-1C-D; Fig. 4-2, H–J; Fig. 4-S3A). The patches were variable in size and shape, with rough dimensions of 30 to 200 nm (Fig. 4-S3B), whereas the small vesicles were quite homogenous (Fig. 4-1C–D) with an average size of 50 nm. The mScarlet fluorescence correlated with this electron-dense region, identifying it as containing large amounts of NLRP3 (Fig. 4-1C–D; Fig. 4-2C–E, H–J; Fig. 4-S3A). While the region around the MTOC contained ribosomes before stimulation, ribosomes were excluded from this region afterwards. Thus, the NLRP3 inflammasome punctum correlates to a patchy, electron-dense, ribosome-free condensate, similar to other cellular condensates (Guo et al. 2018, Zhang et al. 2023). The number of small vesicles as well as microtubule nucleation sites also decreased with time after nigericin stimulation, another indication that the condensate gradually excluded other cellular structures (Fig. 4-3A). No extended filaments besides microtubules were observed, unlike the organized network of tubular filaments away from the MTOC seen by cryo-ET in ASC-overexpressing mouse macrophages (Liu, Zhai et al. 2023). At later time points after nigericin activation (> 30 min), fewer small patches were seen, replaced instead by a large, more uniform dense condensate (Fig. 4-1D; Fig. 4-2E).

In order to examine the dynamics of NLRP3 within the late-stage condensate, we performed fluorescence recovery after photobleaching (FRAP) experiments using mSL-NLRP3 cells also expressing mNeonGreen-ASC. Neither NLRP3 nor ASC in the inflammasome speck recovered after photobleaching (Fig. 4-3B–C), suggesting the condensate had transitioned into a stable, solid-like state.

**NLRP3 inflammasome priming and activation perturbs the MTOC conformation**

In our tomographic reconstructions, each centriole appeared as a ring of nine triplets of microtubules (MTs) 500–700 nm in length and ~250 nm in diameter (Fig. 4-2F–G, I), consistent with previous studies (Paintrand et al. 1992, LeGuennec et al. 2021, Li et al. 2023, Laporte, Gambarotto et al. 2024). In untreated cells, the two centrioles were found to lie perpendicular to each other, spaced an average of 500 nm apart (Fig. 4-4A), also consistent with other studies (Fujita, Yoshino et al. 2016). Because these distances are close to the diffraction limit of our imaging system, under these conditions the two centrioles' fluorescence signal partially overlapped but had distinct maxima (Fig. 4-1A–B).

The pericentriolar material (PCM) has been described as a phase-separated compartment in close contact with the centrosome that acts as a scaffold for nucleating microtubules (Woodruff et al. 2017, Jiang et al. 2021). While we could not discern PCM in the cryo-tomograms of untreated cells, priming with LPS resulted in the appearance of dark amorphous densities with well-defined boundaries, tightly associated with the centrioles (Fig. 4-2B, G, Fig. 4-S3A). As a similarly-dark amorphous material was identified as PCM in a previous report (Li et al. 2023), we interpreted these densities to be PCM. In untreated cells, we observed only a few microtubule nucleation sites in close proximity to the centrioles, but in LPS-primed cells there were many more located within the PCM (Fig. 4-4B–C). Microtubule nucleation sites were identified by conically-shaped γ-tubulin ring complexes (γtuRC) at the tip (Fig. 4-4C) (Guillet et al. 2011, Kollman et al. 2011, Consolati et al. 2020). Recruitment of PCM and enhanced microtubule nucleation are both recognized hallmarks of interphase centrosome maturation (Vertii et al. 2016). Thus, our observations infer that NLRP3 inflammasome priming induces features of centrosome maturation.

Ten minutes after nigericin stimulation, the two centrioles were observed approximately 2 μm away from each other (Fig. 4-4A) and nearly parallel (Fig. 4-1C). Notably, before cryo-FIB milling, the SiR (tubulin) fluorescence appeared as a single punctum in the cryo-light microscope, but after milling, each centriole could be resolved (Fig. 4-S2). The distance between centrioles has been reported to be cell-cycle dependent, and fully separated centrioles (>2 μm) are formed at the late G2 phase (Bertran et al. 2011, Smith et al. 2011, Vitiello et al. 2019). Thus, NLRP3 inflammasome activation induces changes characteristic of cell cycle progression.

**Inflammasome activation induces Golgi cisternae expansion and disruption**

In untreated cells, we observed Golgi stacks with 20–30-nm-thick cisternae, similar to what has been reported in previous studies (Ladinsky et al. 1999) (Fig. 4-5A–B). Following LPS priming, the diameter of cisternae expanded to 80–100 nm (Fig. 4-5A–B), an effect previously reported to reflect increased cargo loading (Dunlop et al. 2017, Williams and Peden 2023). To investigate Golgi structure with a wider field of view than possible with cryo-ET, we stably expressed TGN38-mNeonGreen and recorded fluorescence images. Indeed, the area positive for TGN38 also appeared to be larger in LPS-primed cells compared to untreated cells, suggesting Golgi expansion (Fig. 4-5C). We hypothesize, therefore, that LPS priming alone is sufficient to drive the reported increase in NLRP3 abundancy in the Golgi (Schmacke et al. 2022).

In LPS-primed cells we also noticed clusters of ~50-nm vesicles close to the expanded Golgi (Fig. 6A, Fig. S4A–C). The clusters' positions and vesicle concentration correlated with mScarlet fluorescence intensity, indicating the presence of concentrated NLRP3 (Fig. S5). Sectioning through the vesicle subtomograms revealed densities inside the vesicles (Fig. 4-S4C). Because

NLRP3 cage structures, which have been implicated as the entities recruited to the Golgi (Andreeva et al. 2021), have two opposing PI4P-binding surfaces that may curve membranes to promote vesiculation (Fig. 4-S4C), we wondered if the densities were cages. However, we could not discern regular arrangement within the vesicles (Fig. 4-S4B). Similar small vesicles were not observed in untreated cells or regions outside NLRP3 fluorescence (Fig. 4-6A). The presence of these vesicles in LPS-primed human THP-1 cells is consistent with the recent finding that NLRP3 is immobilized on the Golgi before addition of nigericin (Williams and Peden 2023). In nigericin-activated cells we saw 50-nm vesicles in larger numbers, but we could not detect any special spatial correlation between the clusters of vesicles and mScarlet fluorescence because the fluorescence signal was uniformly high across the entire area due to the growth of the condensate (Fig. 4-S5).

After nigericin stimulation, little or no intact Golgi structure was seen (Fig. 4-5A). Instead, we observed diverse irregularly shaped membrane structures, which may have been cisternae unstacking and morphing into pleomorphic membranes (Fig. 4-5A). Again imaging THP-1 cells stably expressing TGN38-mNeonGreen, the TGN38 fluorescence appeared as dispersed speckles after nigericin activation (Fig. 4-5C), consistent with the cryo-ET data. We hypothesize that the 50-nm vesicles are derived from the Golgi cisternae during its dispersion (Chen and Chen 2018, Andreeva et al. 2021) and carry NLRP3 to the MTOC (Fig. 4-6A–B). Consistent with this hypothesis, some vesicles were non-spherical or even flattened, which is expected for different stages of content release (Fig. 4-6B).

To our surprise we found very few 50-nm vesicles in close contact with microtubule networks or intermediate filaments (Fig. 4-S4D). In mouse macrophages, NLRP3 has been shown to interact

with microtubules and intermediate filaments, and inflammasome activation depends on HDAC6-mediated microtubule transport (dos Santos et al. 2015, Li et al. 2017, Lang et al. 2018, Magupalli et al. 2020). We therefore tested in our human cell line whether inflammasome activation was also dependent on HDAC6-mediated microtubule transport. We found that NLRP3 inflammasome activation is independent of microtubule transport in both wildtype and mSL-NLRP3 cells, as shown by insensitivity to the microtubule disrupter colchicine and the HDAC6 inhibitor tubacin (Fig. 4-S1C–D). This microtubule independence, and the NEK7 independence found in a previous study (Schmacke et al. 2022) in human THP-1 cells, is intriguing as the human inflammasome is still formed at the MTOC.

Notably, we imaged a few LPS-primed cells in which both the MTOC and Golgi stacks were retained in the final lamellae. In these cases, the swollen Golgi stacks appeared as close as 200 nm from a centriole (Fig. 4-S4A). By contrast, in untreated mSL-NLRP3 cells, the MTOC and Golgi were never seen together in the same cryo-tomogram, indicating they are more than a few microns apart (the field of view of one tomogram) and suggesting that cisternae expansion after LPS priming might bring some parts of fully loaded Golgi structures close to the MTOC.

**Mitochondria are recruited to inflammasomes and appear damaged**

Mitochondria have been reported to play a role in the NLRP3 inflammasome activation pathway (Zhou et al. 2011, Gurung et al. 2015, Liu et al. 2018, Yabal et al. 2019). A recent study showed abnormal cristae structures in nigericin-activated ASC-overexpressing mouse iBMDMs (Liu et al. 2023). We observed a plethora of mitochondrial morphologies in untreated, LPS-primed, and early nigericin-activated (10 min) human cells, predominantly displaying intact outer membranes and

evenly distributed cristae, with rare cases showing loss of cristae or irregularly shaped cristae (Fig. 4-S6A). However, the number of mitochondria within 5 μm of the MTOC and NLRP3 condensate increased dramatically after 10 min of nigericin activation (Fig. 4-7A–B). Cells treated with nigericin for more than 30 min revealed much larger mitochondria with reduced cristae (Fig. 4-S6A), an indication of damage (Kaasik et al. 2007). Mitochondria were seen in clusters, and some appeared to be fusing (Fig. 4-7B, Fig. 4-S6B). The formation of mitochondrial clusters has been reported in cells overexpressing the mitochondrial fusion protein Mfn2, a protein known to induce caspase-mediated apoptosis (Huang et al. 2007, Huo et al. 2022). Increased mitochondrial clustering and fusion have also been observed in cells with elevated levels of reactive oxygen species (ROS) (Al-Mehdi et al. 2012, Agarwal and Ganesh 2020). As GSDMD-mediated mitochondrial damage has been shown to induce ROS (Miao et al. 2023, Du et al. 2024), we speculated that the mitochondrial clustering and fusion we observed was caused by similar pathways. After 10 minutes of nigericin activation, mitochondria were also seen in direct contact with autophagosomal-like structures surrounding the NLRP3 condensate (Fig. 4-7C; Fig. 4-S7A-B). We previously showed that NLRP3 inflammasome puncta colocalize with the autophagy marker LC3b (Magupalli et al. 2020). Here we confirmed that NLRP3 fluorescence again colocalized with LC3b in these cells, indicating that at least some of the structures were autophagic (Fig. 4-S7C).

## 4.3 DISCUSSION

### Mechanism of NLRP3 inflammasome activation

Here we have imaged the NLRP3 inflammasome at the MTOC and observed organelle changes associated with inflammasome activation. Our data support the following model. At the MTOC,

LPS priming enhances PCM density and microtubule nucleation (Fig. 4-8). LPS priming also leads to production of NLRP3 and its accumulation in expanded Golgi cisternae (Dunlop et al. 2017, Williams and Peden 2023). Expanded Golgi cisternae give rise to a number of special 50-nm vesicles close to the MTOC that are loaded with NLRP3 and perhaps other inflammasome materials. Nigericin activation then leads to complete Golgi dispersion into membrane fragments and more 50-nm vesicles, with the latter diffusing the short distance to the MTOC without active transport to unload their contents. These contents aggregate and recruit or concentrate ASC and caspase-1, which leads to caspase-1 activation and downstream cytokine release. Mitochondria are recruited and damaged, autophagasomes appear, the condensate eventually solidifies (no exchange of materials), and pyroptosis is triggered.

In context of the existing literature, our work supports Golgi dispersion (Chen and Chen 2018, Andreeva et al. 2021) and gross mitochondria damage after NLRP3 activation, likely by activated GSDMD. The present work does not provide new information about disrupted endocytic trafficking or we cannot rule out the possibility that endocytic trafficking disruptions (Zhang et al. 2023), or morphology-intact mitochondria damage that might underlie mitochondrial DNA release. We were unable to identify regular, ordered structures within the NLRP3 condensates. This observation rules out the presence of long, extended polymer tubes, but not smaller complexes such as the partial inflammasome disks seen in recombinant samples (Xiao et al. 2023), also present. Regular, ordered structures were not discernable in single-particle images of those recombinant samples—the disc shape and structure only became apparent after extensive 2D classification, which required hundreds of thousands of particles (orders of magnitude more than we have in our cryo-tomograms). We posit that extended filamentous structures, which were not

observed in our tomographic reconstructions, are not necessary for NLRP3 inflammasome activation. Instead, smaller assemblies such as partial discs must be sufficient to drive dimerization of the caspase domain of caspase-1 and proximity-induced enzymatic activation (Xiao et al. 2023). It is also possible that the condensate, even without ordered structures within, is sufficient to recruit ASC and caspase-1 and drive dimerization of the caspase domain of caspase-1 for proximity-induced enzymatic activation (Xiao et al. 2023).

We do not know whether mouse NLRP3 also forms condensates during its activation. We speculate that it might because of its localization at the MTOC, similar to human NLRP3. Condensates were not noted in the cryo-ET data of iBMDMs with ASC overexpression (Liu et al. 2023); however, the NLRP3 inflammasome speck in these cells also did not form at the MTOC, unlike specks in wildtype iBMDMs. Further study will be needed to see if condensate formation is a general feature for activation of NLRP3 in different species and how these condensates are related to the ordered inflammasome structures some of us (Xiao et al. 2023) have solved.

## Inflammation and cell division

Our results suggest why formation of the NLRP3 inflammasome and normal cell division are mutually exclusive (Shi et al. 2016): we found that LPS priming led to increased PCM and microtubule nucleation, but NLRP3 inflammasome activation disrupted centriole spacing and created a condensate that enveloped the MTOC, likely limiting its accessibility to other cell division cofactors and halting cell division (Vertii et al. 2016). These observations are consistent with two recent findings that microtubule nucleation requires dynamic PCM (Woodruff et al. 2017), and that loss of PCM is a consequence of full NLRP3 inflammasome activation (Bai et al. 2023).

## Phase separation as a general mechanism to promote innate immune signaling

Biomolecular condensate formation by phase separation has been implicated in numerous biological processes (Garcia et al. 2019, Alberti and Hyman 2021, Shapiro et al. 2021), including immunity to concentrate proteins and the driving of rapid, switch-like signaling (Su et al. 2016, Du and Chen 2018, Jobe et al. 2020, Shen et al. 2021, Yu et al. 2021). Some of us (Shen et al. 2021) previously found that NLRP6, an inflammasome protein in the same family as NLRP3, contains intrinsically disordered regions and forms dynamic condensates when bound to viral dsRNA or bacterial lipoteichoic acid (Shen et al. 2021). The condensate can recruit the ASC adaptor, which in turn recruits caspase-1, leading to solidification of the condensate (Shen et al. 2021). Our results suggest a similar mechanism for the NLRP3 inflammasome. Phase separation and formation of multi-protein complexes likely facilitate spatial control, raise local concentration, and regulate threshold behavior (Park et al. 2007, Lin et al. 2010, Wu 2013, Wu and Fuxreiter 2016). Further elucidation of these mechanisms could open up new avenues for therapeutic strategies to dampen overactive immune pathways.

## Analogy to short-distance presynaptic vesicle trafficking

Intracellular vesicle trafficking is a well-known process for exchanging materials between membrane-enclosed organelles (Cui et al. 2022). Facilitated by motor proteins and cytoskeleton tracks, cargoes secured in vesicles can be transported long distances from one cellular compartment to another. However, less is known about vesicle trafficking across short distances. One example occurs at synapses, where presynaptic vesicles in the phase-separated reserve pool travel approximately 200–300 nm to join the phase-separated active zone (Fernández-Busnadiego et al. 2010, Nelson et al. 2013, Milovanovic et al. 2018, Qiu et al. 2024). Active transport is

apparently not required. The NLRP3-associated vesicles observed in our study share similar features as presynaptic vesicles: both are, on average, 50-nm spherical vesicles enriched in high abundance at particular subcellular regions, and both diffuse short distances to join a phase-separated compartment (Navone et al. 1984, Südhof et al. 1993).

### Fluorescence-guided cryo-FIB milling

Our tri-coincident cryo-FIB-SEM-fluorescence instrument, the ENZEL, allowed us to routinely uncover and preserve in lamellae sub-diffraction-limited fluorescent targets like centrioles and nascent inflammasomes. This reliability allowed us to freeze and image cells at different time points, thereby revealing the entire inflammasome activation process. The resolution of the fluorescence microscopy on the final polished lamellae was even sufficient to correlate bright pixel with specific clusters of concentrated vesicles and their concentration, providing strong evidence that the vesicles contained NLRP3. Collectively, these instrumental and methodological advances open new opportunities for directly visualizing molecular complexes *in situ* by cryo-ET.

## 4.4 ACKNOWLEDGEMENT

We express our gratitude to Delmic B.V. for development of the tri-coincident cryo-FIB-SEM platform, the ENZEL. We would like to acknowledge the Stanford-SLAC Cryo-EM Center and Stanford University Cryo-electron Microscopy Center (cEMc) for instrumentation, with special thanks to Chensong Zhang and Lydia-Marie Joubert. We thank Stanford University Cell Sciences Imaging Facility (CSIF) for training and advice for live cell imaging. We also thank the Core for Imaging Technology & Education (CITE) and Microscopy Resources on the North Quad

(MicRoN) at Harvard Medical School for help with light microscopy. We also thank the Caltech Cryo-EM Facility for instrumentation during the initial phase of this project.

## 4.5 AUTHOR CONTRIBUTIONS

J.W., V.M., P.D.D., H.W., and G.J.J. designed and conceptualized the study. W.M. generated the mSL-NLRP3 THP-1 stable cell line used in this study, performed cytotoxicity assays and immunoblotting, immunofluorescence microscopy experiments and FRAP experiments, image analysis, and quantifications of fluorescence data. J.W. performed sample preparation for cryo-ET, performed live cell imaging and cryo-fluorescence microscopy, image analysis, and quantifications of cryo-ET data. J.W., P.D.D., and G.J.J. pioneered the tri-coincident imaging platform. J.W. performed the cryo-FIB-milling, cryo-ET data collection, data processing, and volume segmentation. P.D.D. and J.W. performed correlative light microscopy. J.W., H.W., and G.J.J. drafted the manuscript. J.W., P.D.D., H.W., and G.J.J. reviewed and edited the manuscript with input from all authors.

This work was supported in part by the National Institutes of Health (AI127401 to G.J.J., AI77778 to H.W., AR079766 to V.G.M., and the Cancer Research Institute Postdoctoral Feelowship to M.W.), Grant 2021-234593 from the Chan Zukerberg Initiative DAF advised fund of Silicon Valley Community Foundation (to P.D.D.), the Panofsky Fellowship at the SLAC National Accelerator Laboratory as part of the Department of Energy Laboratory Directed Research and Development program under contract DE-AC02-76SF00515 (to P.D.D.), and Boston Children's Hospital Office of Faculty Development/Basic & Clinical Translational Research Executive Committees Faculty Career Development Fellowship (to V.G.M.).

## 4.6 DECLARATION OF INTERESTS

H.W. is a co-founder and chair of the scientific advisory board of Ventus Therapeutics. The remaining authors declare no competing interests.

## 4.7 DATA AND CODE AVAILABILITY

Representative cryo-tomograms reported in this study have been deposited in the Electron Microscopy Data Bank (EMDB). Access codes will be provided when available.

This paper does not report original code.

## 4.8 MATERIALS AND METHODS

### Constructs and cloning

pLenti-CMV-Flag-mScarlet-NLRP3 was previously described (Andreeva et al. 2021). TGN38-mNeonGreen and mNeonGreen-ASC were cloned into the pHAGE-EF1α vector between XbaI and NheI sites using Gibson Assembly Master Mix (NEB, Cat. No: M5510).

### Generation of stable cell lines

To produce lentiviral particles, HEK293T cells (80% confluence) in 10 cm dishes were co-transfected with 10 µg pLenti-CMV-Flag-mScarlet-NLRP3, 10 µg pHAGE-EF1α-TGN38-mNeonGreen, or 10 µg pHAGE-EF1α-mNeonGreen-ASC, and packaging plamids 7.5 µg of psPAX2 and 3 µg pMD2.G (Addgene plasmids #12260 and #12259). 12 hours after transfection, the media were removed and replenished with 8 mL of fresh medium. The supernatants containing lentiviral particles were harvested twice at 48 and 72 hours after transfection, filtered through 0.45 µm filter (Pall Corporation, Cat. No: 4184), concentrated using Lenti-X™ Concentrator (Takara Bio, Cat. No: 631231) and stored at -80 °C until use.

To infect THP-1 cells with lentiviruses, cells were cultured in media containing lentiviruses and 20 µg/mL DEAE-Dextran (Sigma-Aldrich, Cat. No: 93556). To increase the transduction efficiency, fluorescence-activated cell sorting (FACS) was performed using a FACSAria II cell sorter from Becton Dickinson equipped with FacsDiva version 8.03. The instrument was set up with a 100 µm nozzle. The sorted populations were gated to exclude double, dead and auto-fluorescent cells. The cells were recovered for at least 7 days before performing subsequent experiments.

## Cell culture

Human monocytic THP-1 cells were maintained in Roswell Park Memorial Institute (RPMI) 1640 Medium (Thermo Fisher Scientific, Cat. No: 11875085), supplemented with heat inactivated 10% FBS and 0.05 mM 2-mercaptoethanol (Thermo Fisher Scientific, Cat. No: 31350010),10 mM HEPES (Thermo Fisher Scientific, Cat. No: 15630080), 1 mM Sodium Pyruvate (Thermo Fisher Scientific, Cat. No: 11360070), 100 units/mL of penicillin and 100 μg/mL of streptomycin.

The NLRP3 KO THP-1 cells were purchased from company (Invivogen, Cat. No: thp-konlrp3z). NLRP3 KO THP-1 reconstituted with mScarlet-NLRP3 cells were generated via lentivirus infection and flow cytometry sorting as described above, which is used for Cryo-electron tomography throughout the manuscript.

All cells were maintained at 37 °C with 5% $CO_2$. For inflammasome activation studies, THP-1 cells were differentiated for 48 hours with 100 nM phorbol myristate acetate (PMA, Sigma-Aldrich, Cat. No: P8139–5MG), followed by priming for 4 hours with 1 μg/mL lipopolysaccharides (LPS, Invivogen, Cat. No: tlrl-b5lps) before stimulation with 20 μM nigericin (Sigma-Aldrich, Cat. No: N7143-10MG) for the indicate times. When needed, 10 μM microtubule polymerization inhibitor Colchicine (Sigma-Aldrich, Cat. No: C9754–100MG), or 20 μM HDAC6 inhibitor Tubacin (Sigma-Aldrich, Cat. No: SML0065-1MG) were used for 2 hours before nigericin treatment.

## Sample preparation for cryo-ET

mScarlet-THP-1 cells were maintained as described in previous section. Cells were differentiated for 24 hours in tissue culture treated plate and seeded onto human fibronectin (25μg/mL in

1xPBS, Advanced Biomatrix, Cat. No: 5050) coated grids (R2/2, Au 200-mesh London Finder grid coated with extra thick carbon, Electron Microscopy Sciences) for another 24 hours to allow sufficient adherence. On the day of plunge freezing, cells on grids were primed with LPS (1 μg/mL) and stained by SiR-tubulin (1 μM, Cytoskeleton, Inc. Cat. No: CY-SC002) for 4 hours (Lukinavičius, Reymond et al. 2014). Cells in the treatment group were further treated with 20 μM nigericin for NLRP3 inflammasome activation for 10 min or 30 min. Untreated cells were stained by SiR-tubulin only for 4 hours. Grids were plunge-frozen in liquid ethane (Airgas) at different time points on a MarkIV vitrobot (Thermo Fisher Scientific) at 100% humidity with manual blotting. Each condition was frozen based on the following order: after 4 hours for both untreated and LPS treated cells; 4 hours plus 10 min for LPS+Nig 10 min treated cells; 4 hours plus 30 min for LPS+Nig 30 min treated cells.

**In-situ fluorescence-guided cryo-FIB-SEM milling**

Frozen grids were clipped into AutoGrids with 4 milling slots (Thermo Fisher Scientific) and loaded onto the Ariyscan laser scanning microscope (Zeiss LSM880) equipped with a cryogenic sample stage (Linkam, CMS196) for inspection of colocalized NLRP3 and MTOC puncta and ice quality. NLRP3 signal was detected by excitation at 555 nm. MTOC signal was detected by excitation at 625 nm. Grids were then transferred to an Aquilos2 Dual-Beam system (Thermo Fisher Scientific) with customized integrated fluorescent light microscope (ENZEL from Delmic) that is coincident with the FIB and SEM of the Aquilos2 as described previously (Boltje et al. 2022). Organo-platinum (Pt) deposition was applied to grids via the gas injection system (GIS) for 20-30 seconds. The NLRP3 inflammasome was identified as the colocalized NLRP3 and MTOC puncta observed on the ENZEL system equipped with a 100x long working distance vacuum

objective (NA 0.85). Materials above and below the target of interests were ablated accordingly monitored by real-time fluorescence. The stepwise milling was performed as described in previous studies (Wagner et al. 2020, Lam and Villa 2021). In brief, rough milling, thinning, and polishing were done at 0.1nA, 30pA, 10pA at 30kV. Final fluorescent images were taken when the thickness of the lamella was approximately 200nm with the following imaging parameters: NLRP3, ~0.96 W/cm$^2$ of 550 ± 10 nm with 1.5-2 seconds exposure; MTOC, ~ 0.46 W/cm$^2$ of 625 ± 10 nm with 1-2 seconds exposure; Reflected brightfield, ~0.1 W/cm$^2$ of 550 ± 10 nm with 500 milliseconds exposure.

**Tilt series acquisition guided by correlated fluorescence microscopy**

Atlases and tilt series were acquired on a Titan Krios G2 (Thermo Fisher Scientific) at 300 keV equipped with a K3 Summit detector and BioQuantum post-column energy filter (Gatan) operated in counting and dose fractionation mode with 10 eV slit in. Atlases were collected as joint serial sections at 6,500x magnification under low dose mode in SerialEM software suite (Mastronarde 2003, Mastronarde 2005). Tilt series were collected at a pixel size of 3.465 Å with a total dose of approximately 120-160 $e^-/Å^2$, ranging from -48° to 60° to account for a ~6-8° milling angle with 2-degree increment using SerialEM. This study included a total of 52 tilt series: 11, 17, 20, 4 for untreated, LPS, LPS+Nig 10 min, LPS+Nig 30min, respectively.

**Tomogram reconstruction and quantification of cellular features**

Unbinned image frames were preprocessed in WARP with patch motion correction, CTF estimation, and defocus estimation, which ultimately assembled to aligned tilt series with a binning factor of 2 (Tegunov and Cramer 2019, Tegunov et al. 2021). Aligned tilt series were reconstructed

manually in IMOD at a pixel size of 13.86 Å with 30 iterations of SIRT-like filter following CTF correction (Kremer et al. 1996, Mastronarde and Held 2017). Tomogram reconstructions containing TGN were loaded in FIJI for measuring cisternae width. Tomogram reconstructions containing NLRP3 associated vesicles were loaded in IMOD (Kremer et al. 1996, Mastronarde and Held 2017). The center of each vesicle was manually set and used the size function to measure the radius of each vesicle in pixel, which later was converted to vesicle diameter in nanometers.

### Tomogram segmentation and visualization

Tomograms used for segmentation were imported to Dragonfly 2022.2 and subject to Gaussian filtering to enhance image contrast. Training data sets were prepared by manually segmented 10 slices containing microtubules, large membrane structures, Golgi stacks, small vesicles, ribosomes, and mitochondria. The Neural Network Model was generated with a dimension of 2.5D and 3 slices. NLRP3 condensate and PCM were segmented using the thresholding tool. Segmented features were exported independently and later processed in FIJI with Gaussian blurring (sigma=0.8) and imported to ChimeraX (version 1.7.1) for visualization (Meng et al. 2023). Tomograms containing NLRP3 vesicles were manually segmented in IMOD for microtubules, NLRP3 associated vesicles, and intermediate filaments.

### Correlative fluorescence microscopy

Registration of fluorescence and electron tomography data was performed utilizing a customized toolkit compatible with MATLAB version R2023b. Briefly, 16-bit multi-channel fluorescent images obtained from the ENZEL system were firstly correlated to atlases collected at 6500x magnification using obvious features (e.g., lamellae edges, visible ice contamination, or grid holes)

present in both brightfield optical microscopy and the electron microscopy. A total of 8-10 pairs of reference points were selected accordingly for precise correlation. These point pairs were used to calculate a projective transformation to carry the fluorescence data to this low magnification EM space. Secondly, a new set of points visible in the registered atlases and in a z-projection of the tomographic reconstruction were selected. These points largely included visible cellular features (e.g., large membrane structure, vesicles, mitochondria, or MTOC). A total of 10-13 pairs of reference points were manually selected for registration and the computation of a similarity transformation to carry the atlas space into the tomography space. Lastly, the projective and similar transformation were serially applied to the fluorescence images to bring the fluorescence images to the tomography space. For visualization, final correlated images containing SiR-tubulin and NLRP3 channels were generated by overlaying fluorescent channels with actual tomogram reconstruction (z = 10 slices).

### Vesicle correlation analysis

Correlated atlases and tomogram reconstructions were computed as described in previous section. Vesicle x and y coordinates were extracted from IMOD segmented models and later correlated with registered tomogram reconstructions. Number of vesicles within each registered fluorescent pixel was plotted and fitted to a simple linear regression.

### LDH cytotoxicity assay

WT THP-1, NLRP3 KO THP-1 and NLRP3 KO THP-1 reconstituted with mScarlet-NLRP3 were seeded on a 24 well plate. After differentiation, priming and NLRP3 activation, cell

supernatants were analyzed for LDH activity using LDH-Glo™ Cytotoxicity Assay Kit (Promega, Cat. No: J2381) according to manufacturer's guidelines.

## Immunofluorescence (IF)

To detect protein localization by immunofluorescence in fixed cells, cells were seeded on High Performance No.1.5 18 × 18 mm glass coverslips (Zeiss™ Cat. No: 474030-9000-000), and fixed with 4% PFA for 15 min, followed by permeabilization with 0.5% Triton X-100 for 5 min. Then, cells were blocked with 1.5% BSA for 1 hour at room temperature. Primary antibodies (ASC 1:200, AdipoGen: AG25B0006C100; LC3B 1:20, Santa Cruz Biotechnology: sc-271625) were diluted in 1.5% BSA and incubated overnight with fixed cells at 4 °C. After washing with 1 × DPBS 3 times, fluorescent secondary antibodies were 1: 1,000 diluted in 1.5% BSA and incubated for 1 hour at room temperature. Samples were mounted in VECTASHIELD antifade mounting medium (Vector Laboratories, Cat. No: H-1000-10) and sealed with Nail polish (Fisher Scientific, Cat. No: NC1849418).

## Live cell imaging

For visualization of mScarlet-NLRP3-THP-1, TGN38-mNeonGreen and SiR-tubulin in live cells, cells were differentiated and grown in glass bottom dishes (MatTek corporation, Cat. No: P35G-1.5–14-C) for 48 hours. Then cells were first washed once with PBS and the medium was replaced by RPMI 1640 medium with no phenol red (Thermo Fisher Scientific, Cat. No: 11835030) supplemented with 10% FBS, and placed back in the incubator for at least 1 hour. 1 μM SiR-Tubulin was used for 1-2 hours to stain the microtubule network in live cells. Live cell images were obtained at 37 °C with 5% $CO_2$ condition.

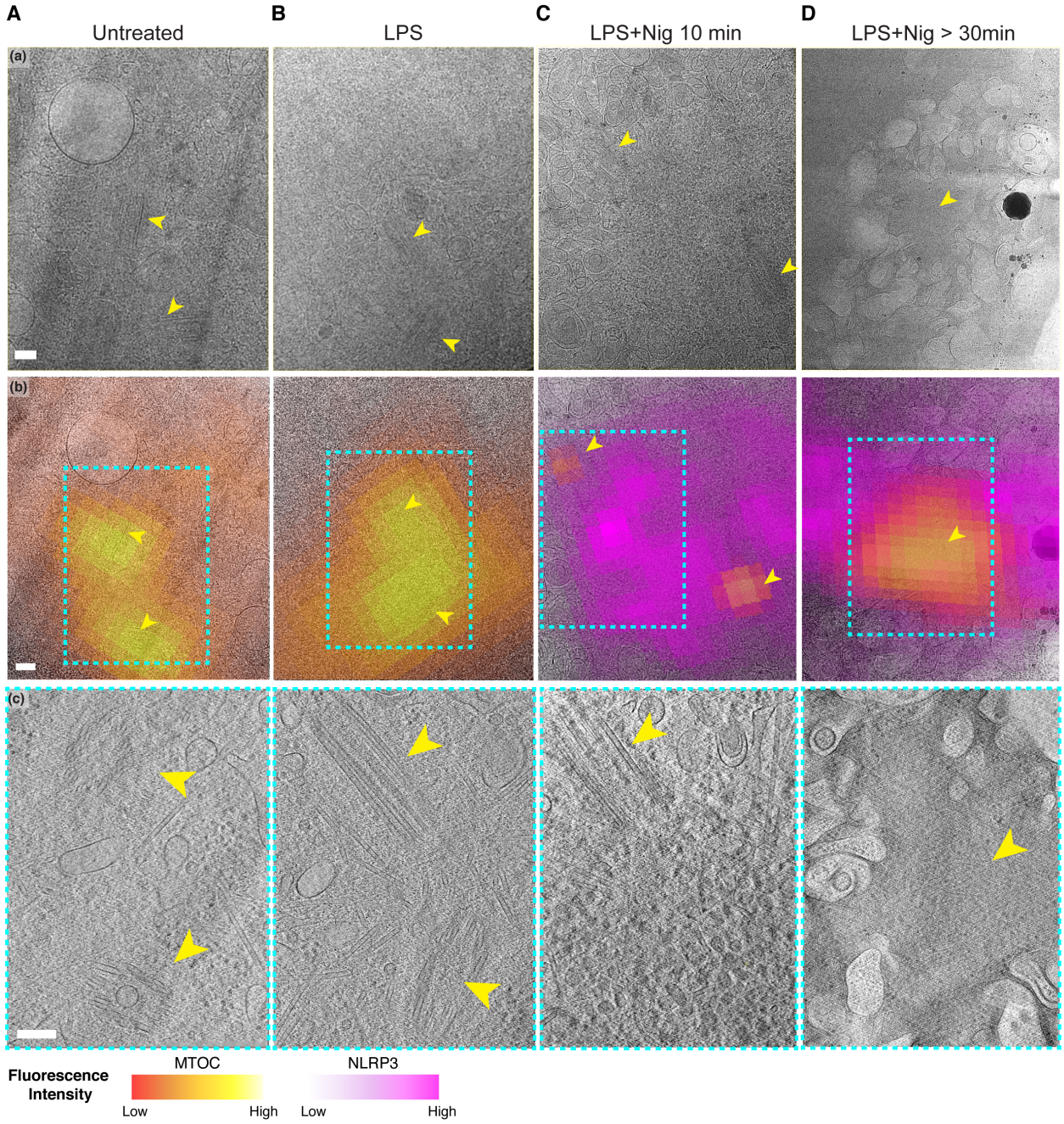


**Figure 4-1. Fluorescent signals guide milling and cryo-ET imaging to the NLRP3 inflammasome and MTOC.** **(A–D)** Representative images with increasing magnification showing the MTOC and formation of the NLRP3 inflammasome condensate ordered by chronological sequence with **(a)** cryo-ET atlas, **(b)** fluorescence image overlaid with (a), **(c)** representative tomographic slices obtained from designated imaging area indicated as cyan dashed lines in (b). The MTOC and NLRP3 inflammasome are colored in yellow and magenta, respectively, based on fluorescence intensity profile. Two centrioles from the MTOC are indicated by yellow arrows. Arrow positions were determined by (b) and superimposed to (a) and (c), respectively. Number of incidents at each stage: Untreated, N=12; LPS, N=10; LPS+Nig 10-20 min, N=10; LPS+Nig > 30min, N=3. (scale bar = 200nm for all panels).

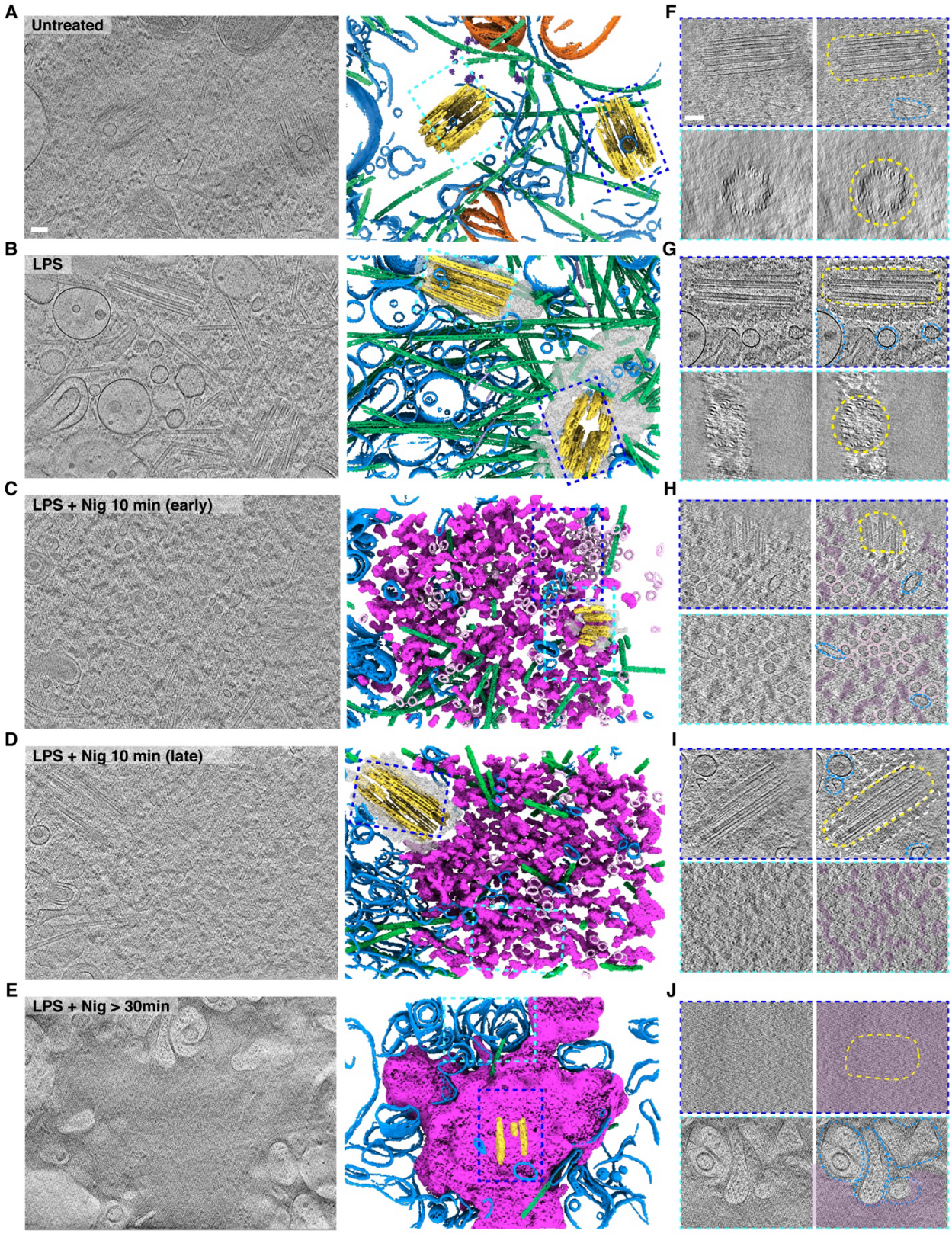
A
Untreated
B
LPS
C
LPS + Nig 10 min (early)
D
LPS + Nig 10 min (late)
E
LPS + Nig > 30min
F
G
H
I
J

**Figure 4-2. NLRP3 inflammasome activation leads to formation of condensate at the MTOC. (A–E)** Representative tomographic slices and segmented models illustrating NLRP3 inflammasome activation (MTOC, yellow; microtubules, green; NLRP3-associated vesicles, light pink; NLRP3 condensate, magenta; membrane, blue; mitochondria, orange, ribosomes, purple; scale bar = 100 nm). **(F–J)** Enlarged and rotated views of the areas immediately surrounding the centriole marked by the dashed boxes A-E.

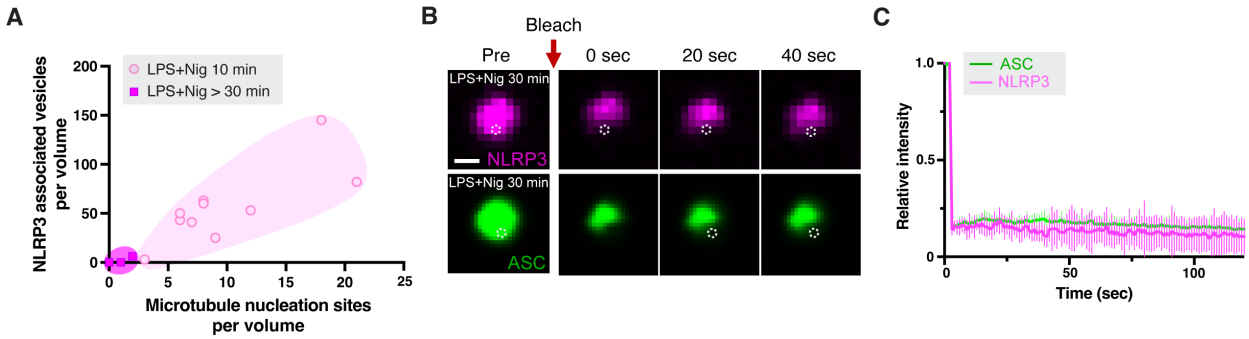


**Figure 4-3. NLRP3 inflammasome becomes an immobilized solid condensate. (A)** Correlation analysis of number of NLRP3-associated vesicles and number of microtubule nucleation sites within NLRP3 condensate. Each data point represents one cell. Individual cells treated with LPS+Nig 10 min are indicated as light pink circles; cells treated with LPS+Nig > 30 min are marked as magenta squares. Area shaded in light pink includes all cells treated with LPS+Nig 10 min; area shaded in magenta includes all cells treated with LPS+Nig > 30 min. **(B-C)** Tracking of NLRP3 mobility by fluorescence recovery after photobleaching (FRAP). Bleached areas indicated by white dashed circle (scale bar = 1 μm).

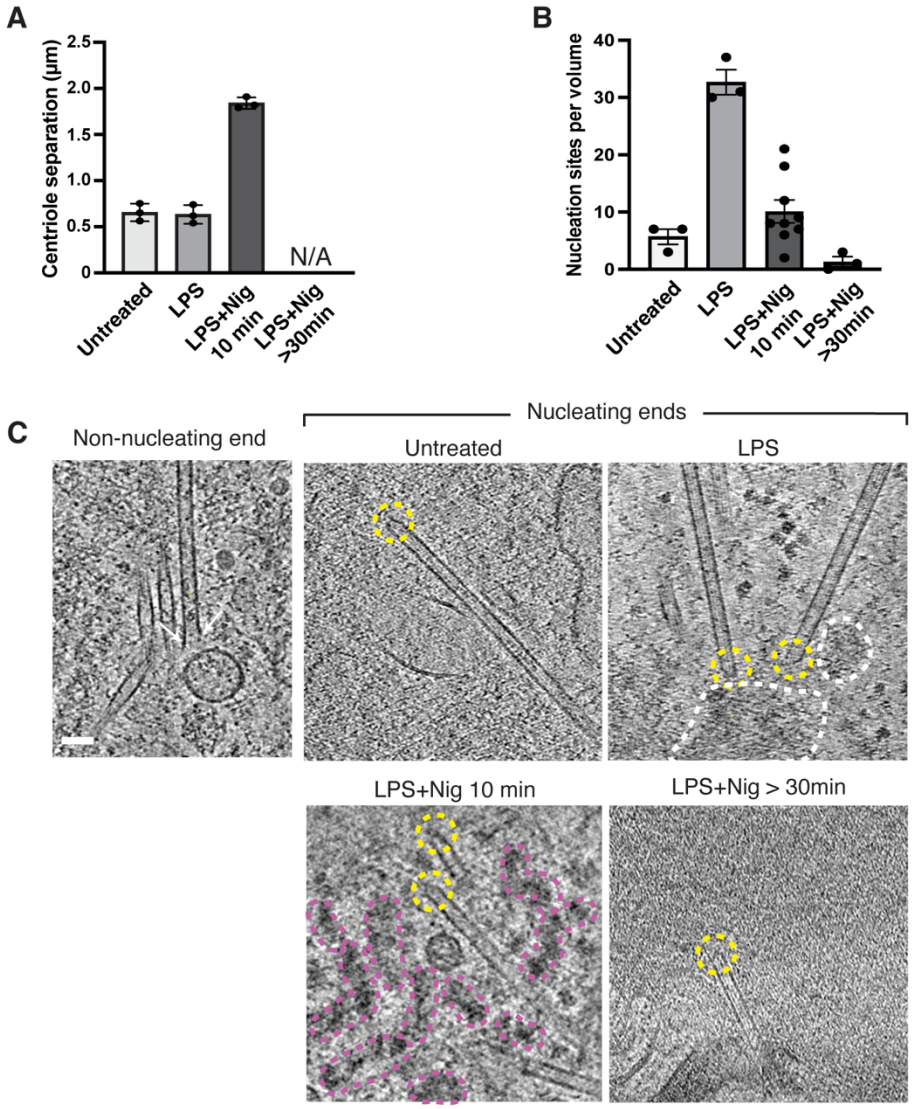


**Figure 4-4. NLRP3 inflammasome activation alters MTOC conformation. (A)** Distance of centriole separation in response to NLRP3 inflammasome activation (one-way ANOVA, $p < 0.0001$). **(B)** Quantification of the number of nucleation sites in presence of the complete MTOC. Each data point represents one cell (one-way ANOVA, $p < 0.0001$). (**C**) Representative tomographic slices showing non-nucleating ends and MT nucleation sites at different conditions. The non-nucleating end is marked by two white arrows and the nucleation site is circled in yellow; PCM and NLRP3 condensate are marked by white and magenta dotted circles, respectively (scale bar = 50nm).

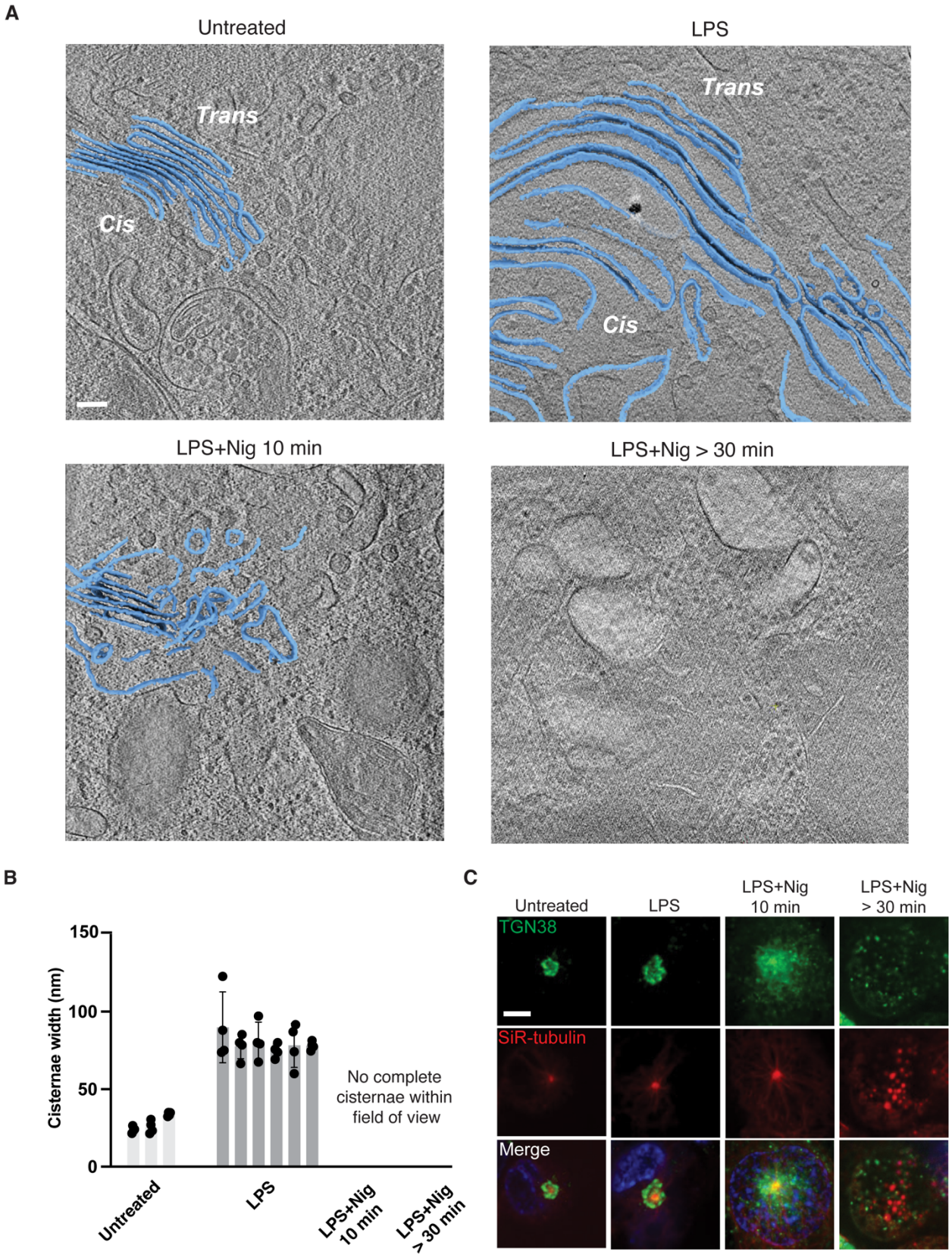
A
Untreated
Trans
Cis
LPS
Trans
Cis
LPS+Nig 10 min
LPS+Nig > 30 min
B
Cisternae width (nm)
150
100
50
0
Untreated
LPS
LPS+Nig 10 min
LPS+Nig > 30 min
No complete cisternae within field of view
C
Untreated
LPS
LPS+Nig 10 min
LPS+Nig > 30 min
TGN38
SiR-tubulin
Merge

**Figure 4-5. Nigericin activation disrupts Golgi integrity. (A)** Tomographic slices with segmented Golgi cisternae (Golgi cisternae, blue; z = 10, scale bar = 100 nm). Face of the Golgi is assigned based on relative distance to the nucleus on lamellae where the *Cis* face is closer to the nucleus. **(B)** Quantification of the cisternae spacing in response to LPS. Each bar graph represents 3 distance measurements for each Golgi structure. All cells come from different passages and different grids (Untreated, n = 3; LPS, n = 6; one-way ANOVA, $p < 0.0001$). **(C)** Live cell imaging of TGN38-mNeonGreen and SiR-tubulin during NLRP3 inflammasome activation (scale bar = 5 μm).

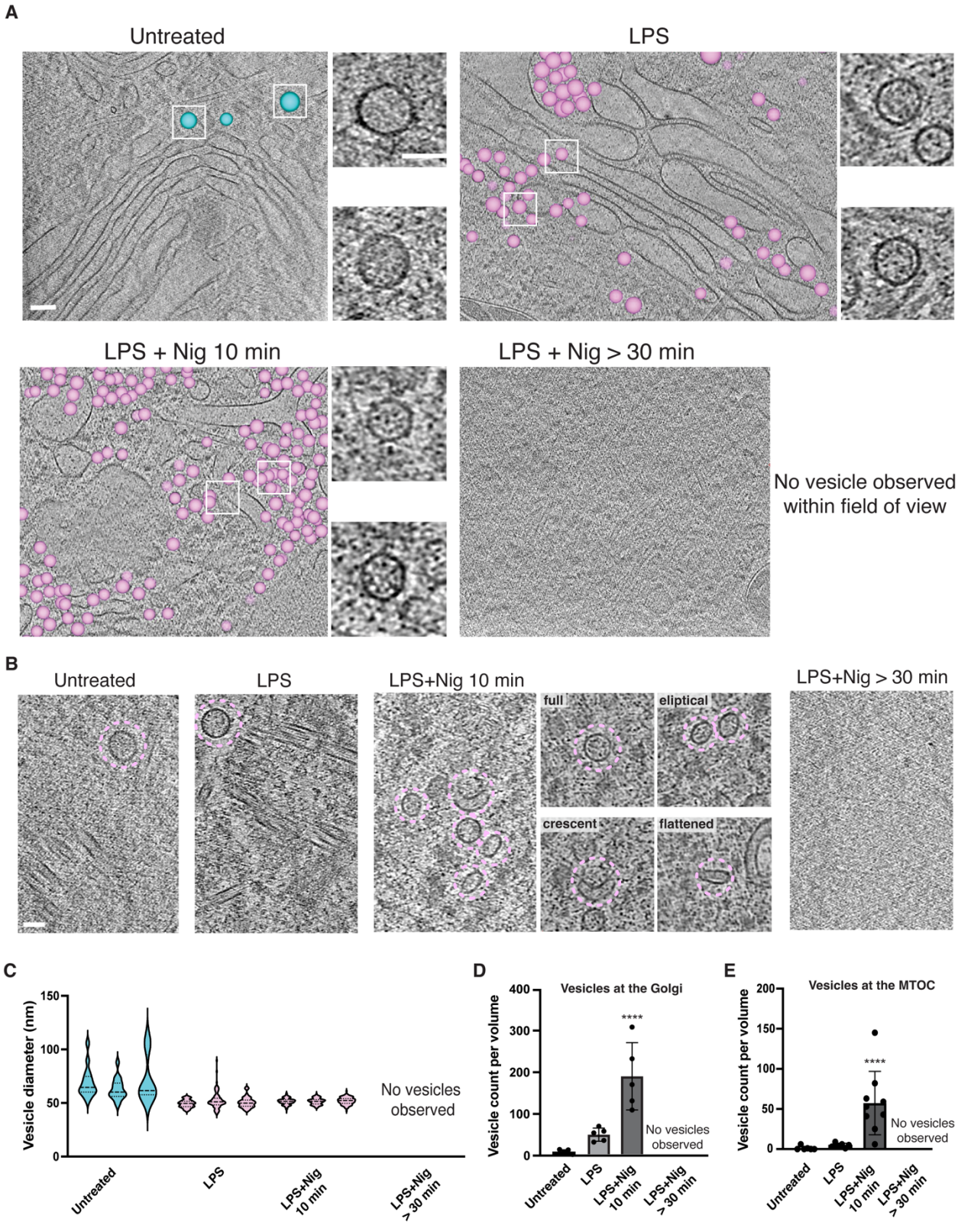
A
Untreated
LPS
LPS + Nig 10 min
LPS + Nig > 30 min
No vesicle observed within field of view
B
Untreated
LPS
LPS+Nig 10 min
full
eliptical
crescent
flattened
LPS+Nig > 30 min
C
Vesicle diameter (nm)
150
100
50
0
No vesicles observed
Untreated
LPS
LPS+Nig 10 min
LPS+Nig > 30 min
D
Vesicles at the Golgi
Vesicle count per volume
400
300
200
100
0
****
No vesicles observed
Untreated
LPS
LPS+Nig 10 min
LPS+Nig > 30 min
E
Vesicles at the MTOC
Vesicle count per volume
200
150
100
50
0
****
No vesicles observed
Untreated
LPS
LPS+Nig 10 min
LPS+Nig > 30 min

**Figure 4-6. NLRP3-associated vesicles trafficking to the MTOC independent of microtubule transport. (A)** Overlaid tomographic model on segmented slices showing vesicles observed at the Golgi (vesicles observed before priming and NLRP3 inflammasome activation, cyan; vesicles observed after priming and NLRP3 inflammasome activation, light pink; scale bar = 100 nm). Enlarged view of representative vesicles observed under each condition indicated by white boxes (scale bar = 50 nm). **(B)** Representative tomographic slices showing vesicles near the MTOC before and after NLRP3 inflammasome condensate formation (z = 10). Vesicles are circled in light pink. **(C)** Quantification of vesicle diameters in response to NLRP3 inflammasome activation. Each violin plot represents one cell (one-way ANOVA, $p < 0.0001$). **(D)** Quantification of vesicle numbers observed near the Golgi in response to NLRP3 inflammasome (one-way ANOVA, $p < 0.0001$). Each data point represents one cell. **(E)** Quantification of number of vesicles present at the MTOC at different conditions. Each data point represents one cell (one-way ANOVA, $p < 0.0001$).

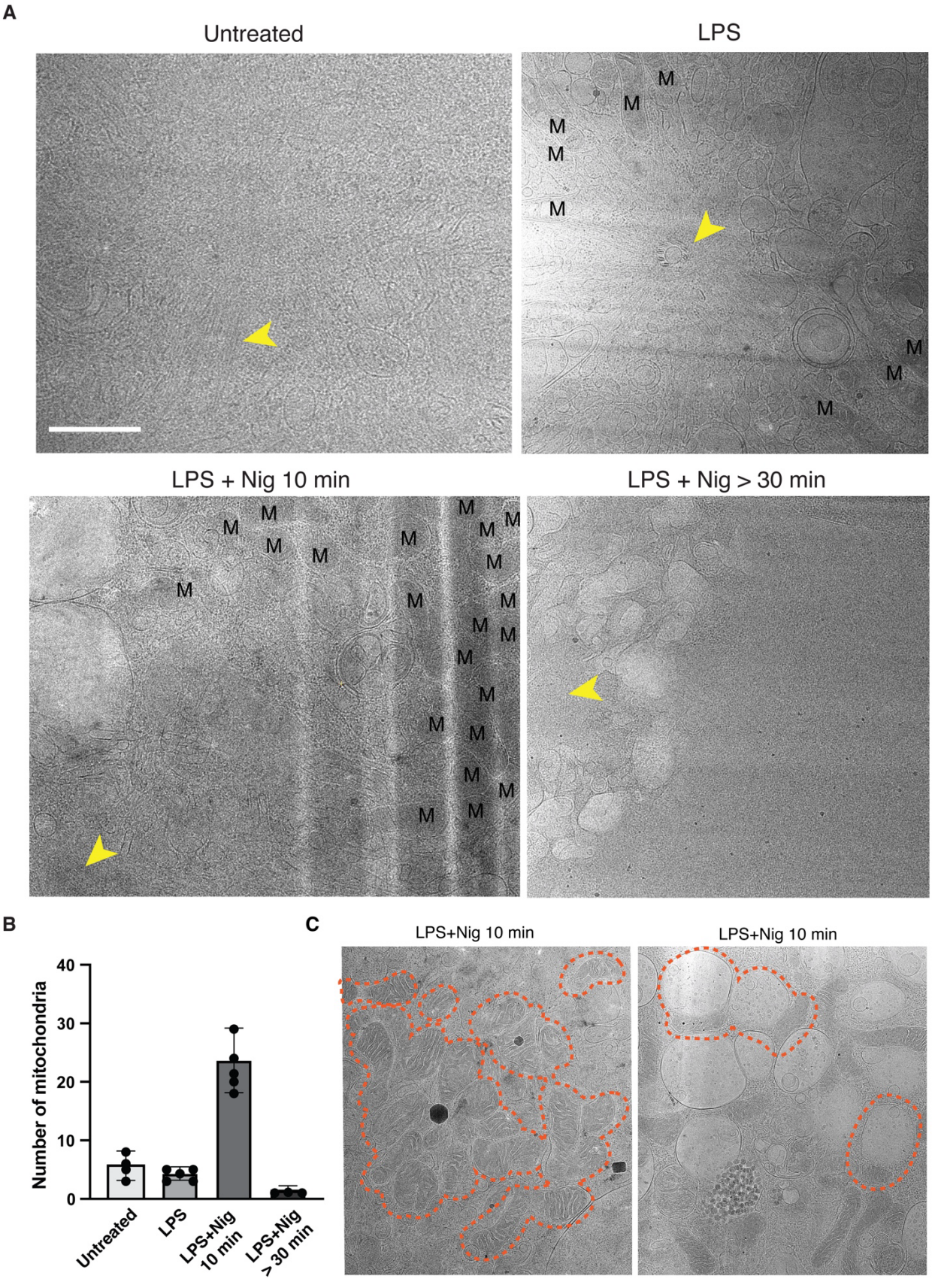
A
Untreated
LPS
LPS + Nig 10 min
LPS + Nig > 30 min
M
B
Number of mitochondria
40
30
20
10
0
Untreated
LPS
LPS+Nig 10 min
LPS+Nig > 30 min
C
LPS+Nig 10 min
LPS+Nig 10 min

**Figure 4-7. NLRP3 inflammasome activation induces changes in mitochondria. (A)** Representative atlas views of the MTOC and nearly mitochondria (scale bar = 1 μm). Centrioles are marked in yellow and mitochondria are denoted as "M." **(B)** Quantification of number of mitochondria present within 5 μm from the MTOC. Each data point represents one cell (one-way ANOVA, $p < 0.0001$). **(C)** Representative mitochondria cluster and associated with putative autophagosome (dashed orange areas).

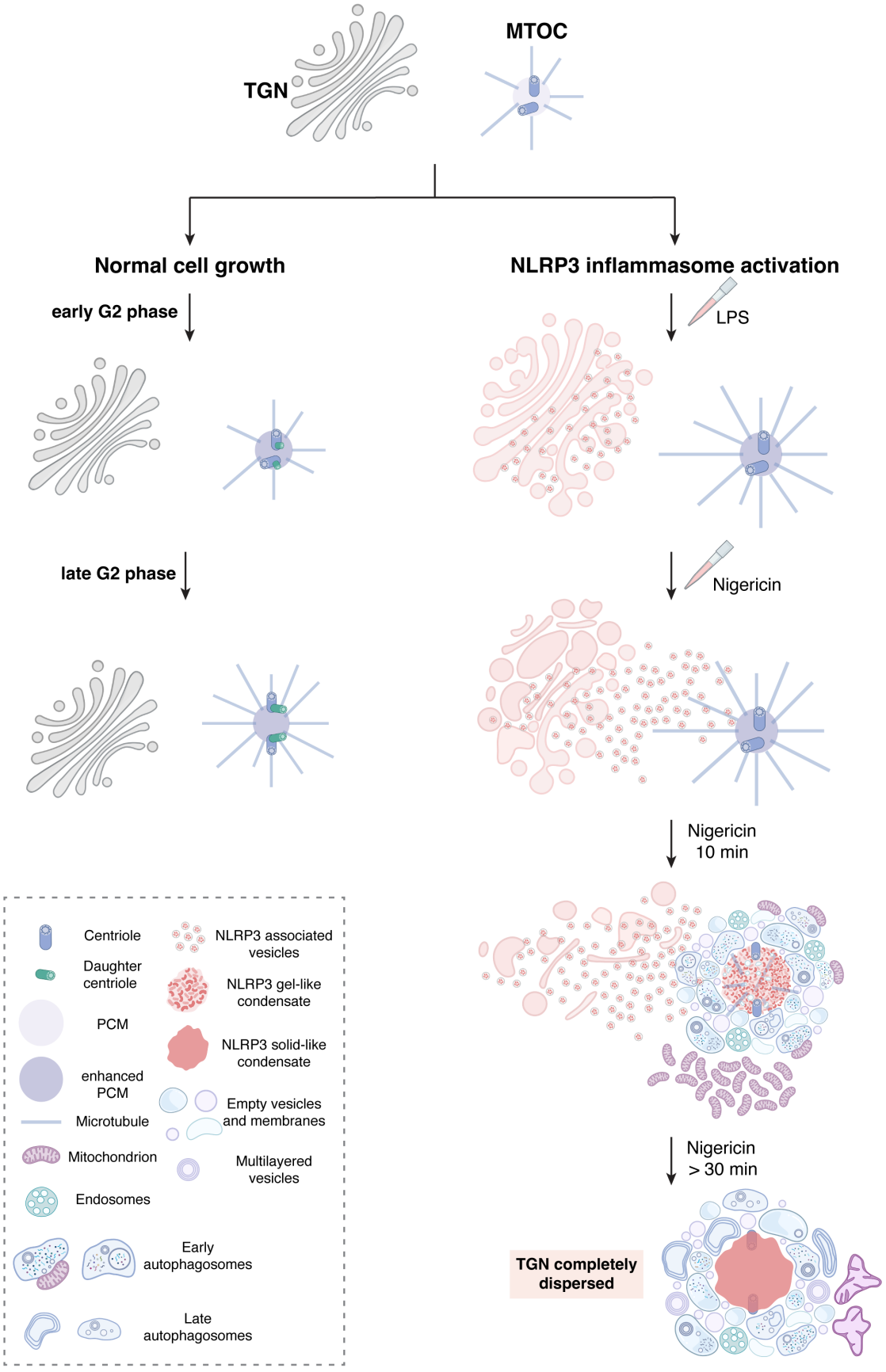
TGN
MTOC
Normal cell growth
NLRP3 inflammasome activation
early G2 phase
late G2 phase
LPS
Nigericin
Nigericin
10 min
Nigericin
> 30 min
TGN completely
dispersed
Centriole
Daughter
centriole
PCM
enhanced
PCM
Microtubule
Mitochondrion
Endosomes
Early
autophagosomes
Late
autophagosomes
NLRP3 associated
vesicles
NLRP3 gel-like
condensate
NLRP3 solid-like
condensate
Empty vesicles
and membranes
Multilayered
vesicles

**Figure 4-8. Progression of NLRP3 inflammasome activation at the MTOC.** Cartoon representations are annotated in the bottom left. The NLRP3-associated vesicles were modeled based on previous structures (PDB: 7FLH) (Andreeva et al. 2021). [Figure was created with BioRender, https://BioRender.com).]

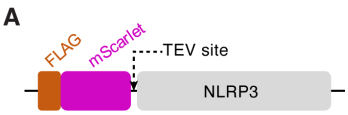


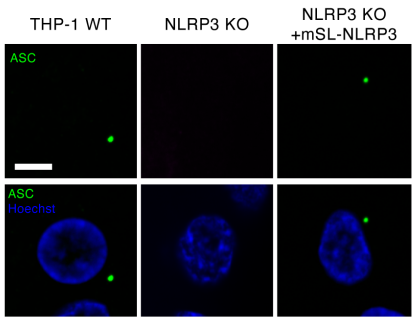


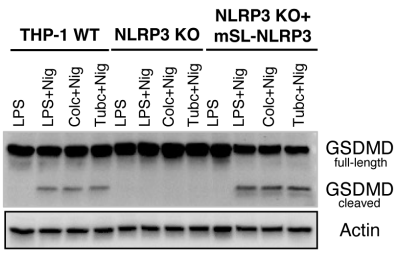


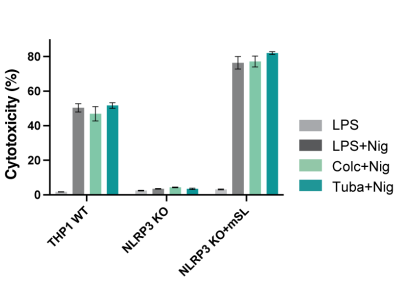


G

| | Colocalized MTOC-NLRP3 | Non-colocalized MTOC-NLRP3 |
|---|---|---|
| 37 degree | 87 | 0 |
| -180 degree | 94 | 0 |

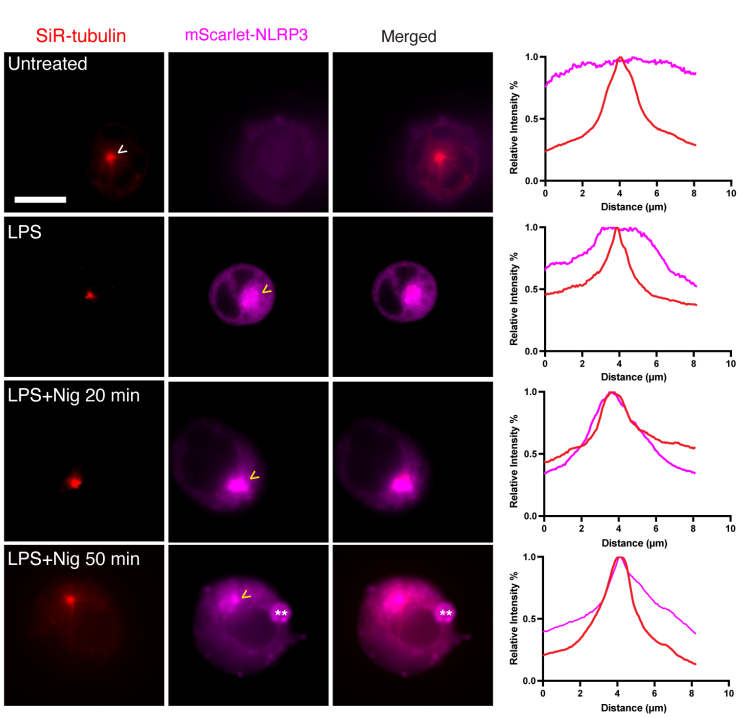


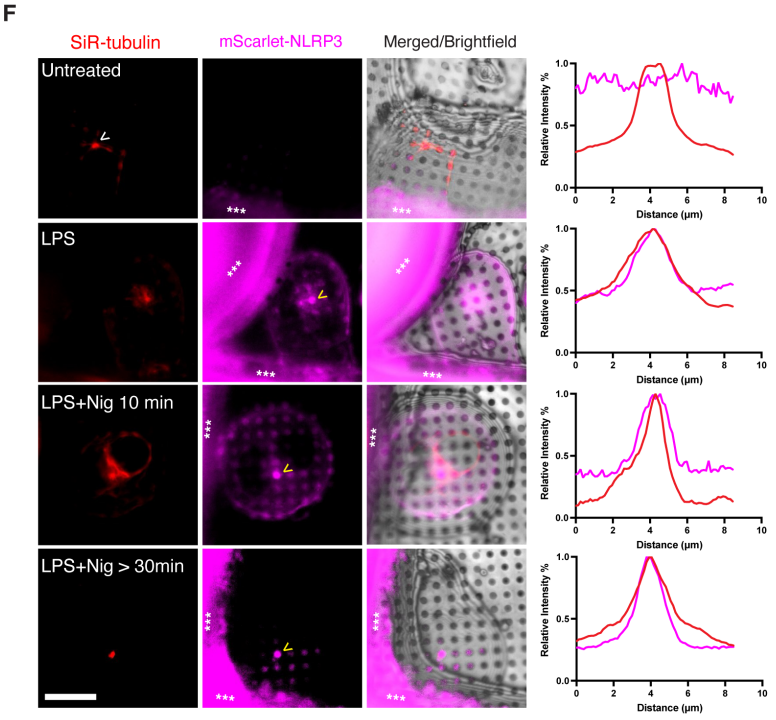

**Figure 4-S1. NLRP3 inflammasome activation leads to formation of a single punctum at the MTOC independent of microtubule transport in mSL-NLRP3 cells. (A)** A schematic of the FLAG-mSL-NLRP3 construct. **(B)** Confocal imaging of ASC speck formation in THP-1 cells (wildtype, NLRP3 KO, and mSL-NLRP3) by IF. Cells were primed with 1 μg/mL LPS for 4 hours and treated with 20 μM nigericin for 30 min. Green: ASC, Blue: nucleus (Scale bar = 5 μm). **(C–D)** Western blot (C) and LDH release assay (D) for NLRP3 activation in THP-1 cells (wildtype, NLRP3 KO, and NLRP3 KO reconstituted with mSL-NLRP3). LPS-primed cells were treated with 10 μM microtubule polymerization inhibitor Colchicine (Colc) or 20 μM HDAC6 inhibitor Tubacin (Tubc) for 2 hours before activation with 20 μM nigericin for 30 min. **(E)** Live cell imaging of mSL-NLRP3 cells before and after NLRP3 inflammasome activation. Cells were primed and activated following the same protocol in (A). NLRP3 inflammasome puncta are indicated by yellow arrows, and MTOC puncta in inactivated cells are indicated by white arrows. Cell debris is marked with two asterisks (Scale bar = 10 μm). Fluorescence intensity profiles of puncta are shown in the last panel of each row. **(F)** Cryogenic fluorescent imaging of mSL-NLRP3 cells before and after NLRP3 inflammasome activation. Cells were primed and activated following the same protocol in (A). NLRP3 inflammasome puncta are indicated by yellow arrows, and MTOC puncta in inactivated cells are indicated by white arrows. Grid bars are marked as asterisks (Scale bar = 10 μm). Fluorescence intensity profiles of puncta are shown in the last panel of each row.

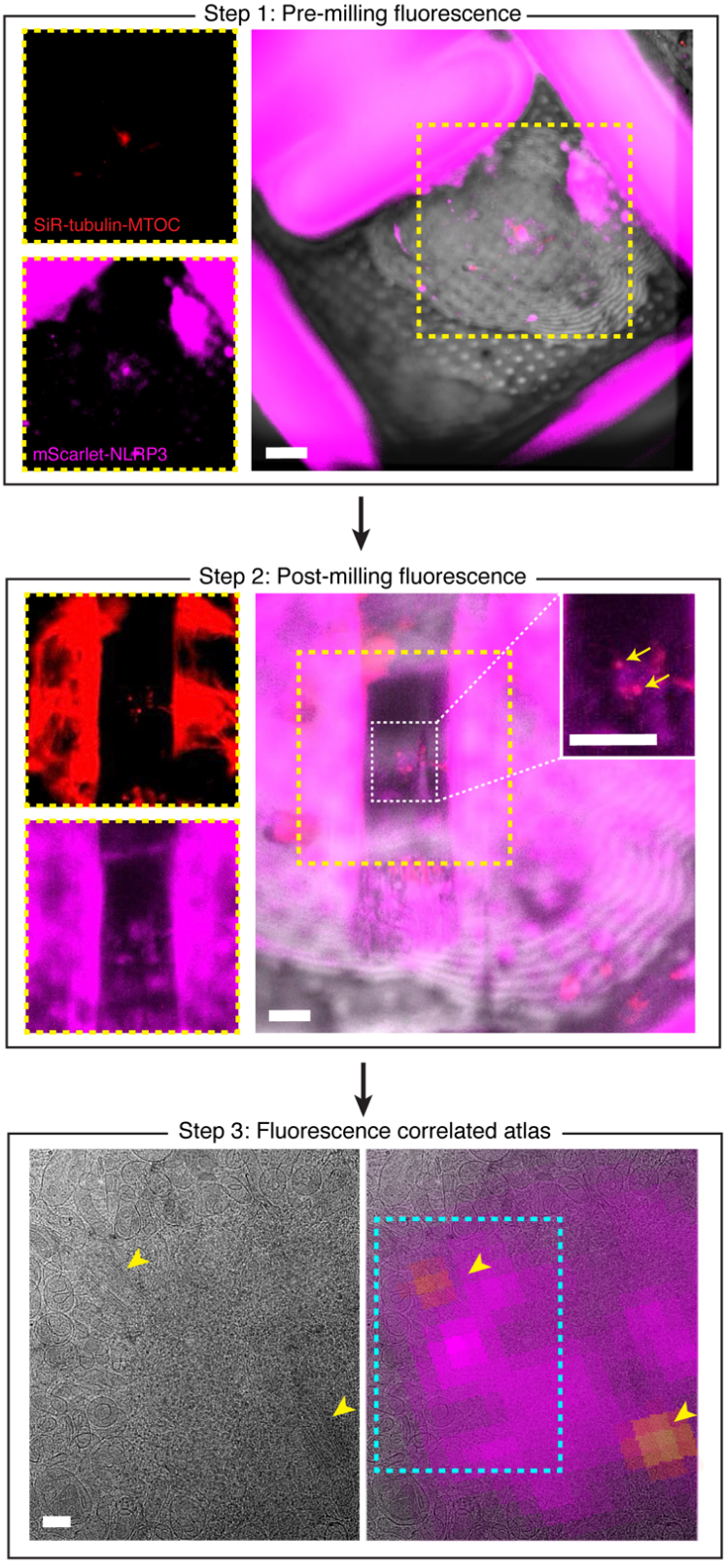
Step 1: Pre-milling fluorescence
SiR-tubulin-MTOC
mScarlet-NLRP3
Step 2: Post-milling fluorescence
Step 3: Fluorescence correlated atlas
Step 4: Cryo-ET tilt series collection

**Figure 4-S2. Fluorescence guided cryo-FIB-SEM milling workflow for targeting the NLRP3 inflammasome and MTOC.** Fluorescent images of stepwise targeted milling. The representative example was treated with LPS+Nig 10min. The same example was also shown in Fig. 1 C and Fig. 2D, I. Centrioles are indicated as yellow arrows. Imaging frame size is marked in cyan. Scale bar=10 μm for all panels showing fluorescent images; scale bar=200nm for representative cryo-EM images.

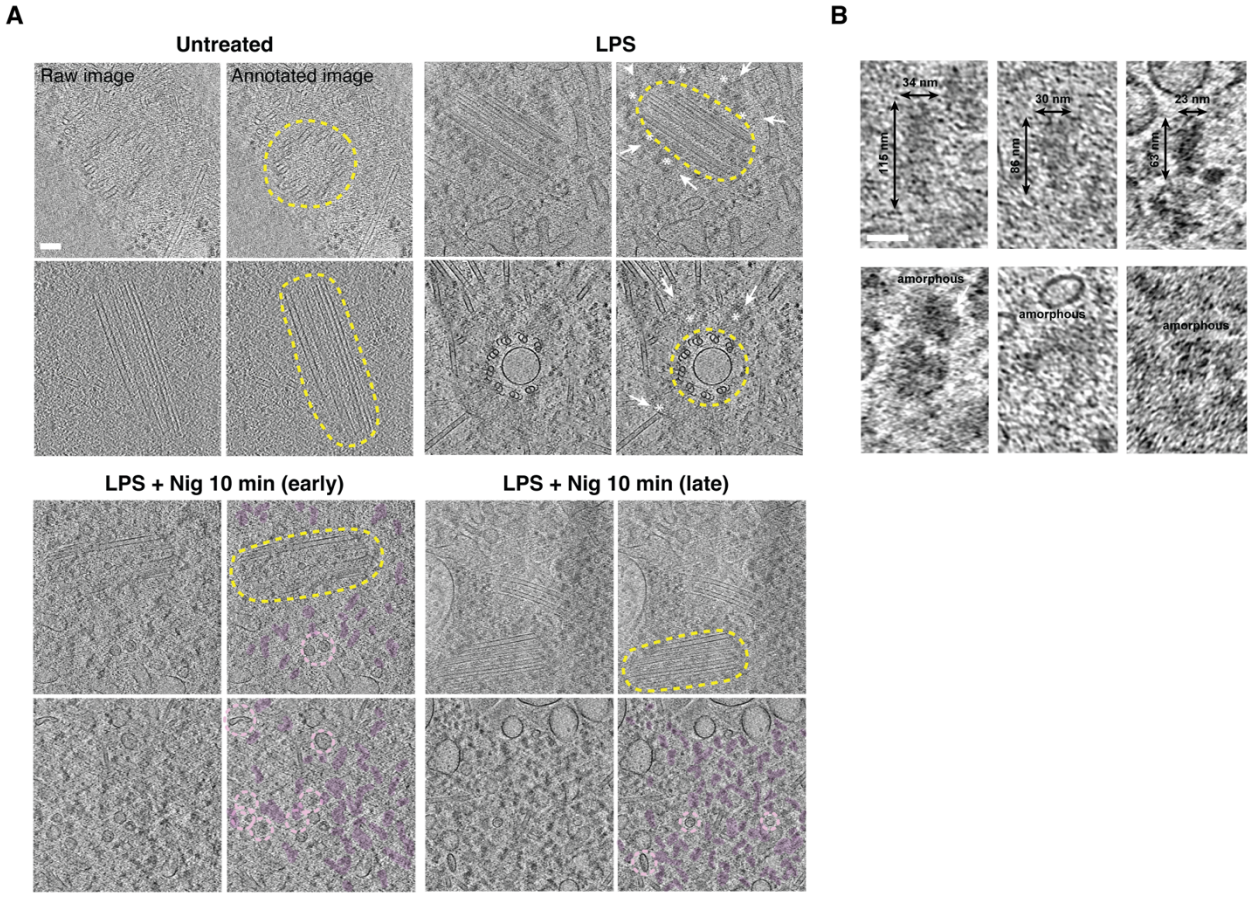


**Figure 4-S3. NLRP3 inflammasome forms condensate with pericentriolar material (PCM). (A)** Representative tomographic slices showing NLRP3 condensate in chronological order (scale bar=100 nm). Cellular features are marked as following: MTOC, yellow; NLRP3 condensate, magenta; NLRP3-associated vesicles, light pink. For each row, raw images are shown on the left and annotated images are shown on the right. **(B)** Representative examples of NLRP3 condensate (scale bar=50 nm).

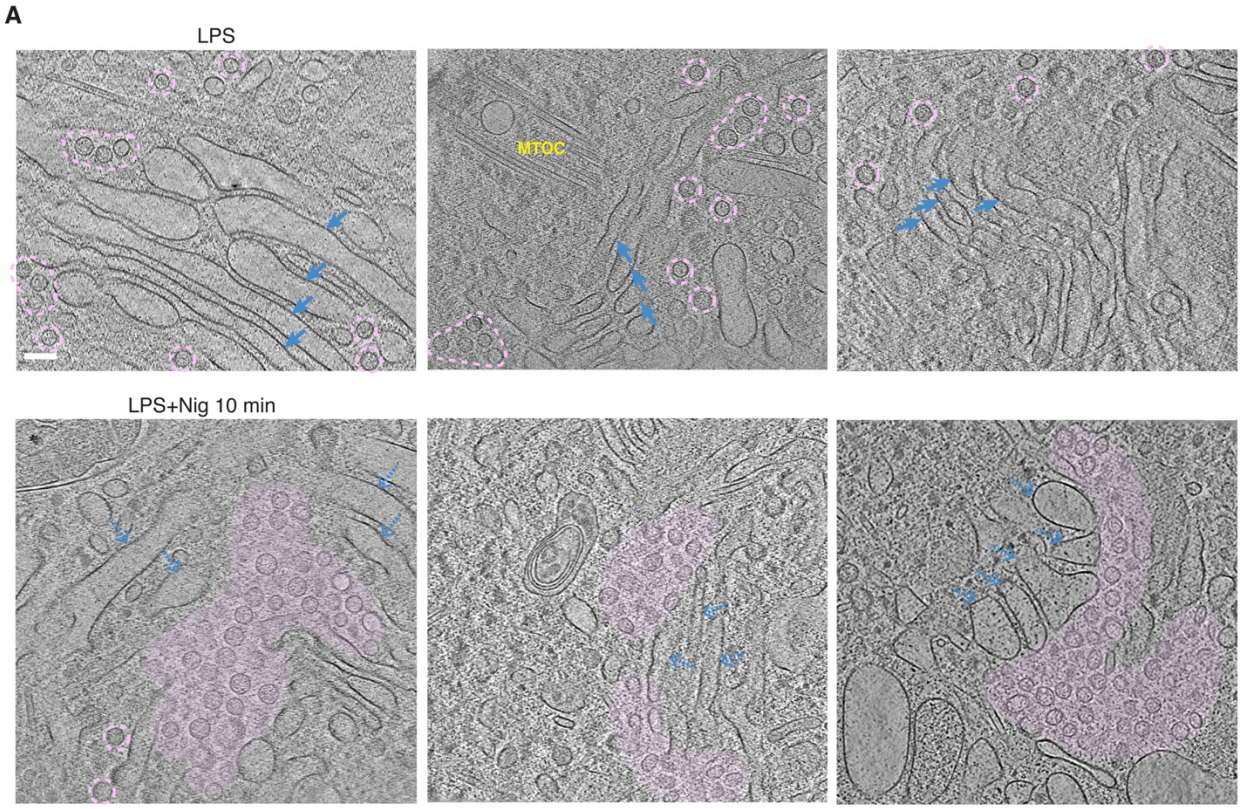
A
LPS
MTOC
LPS+Nig 10 min

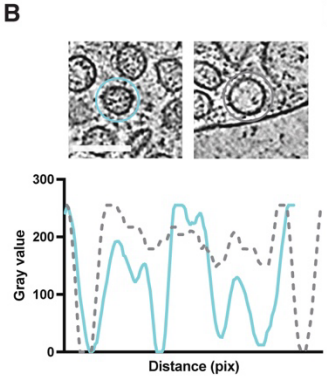
B
300
200
100
0
Gray value
Distance (pix)

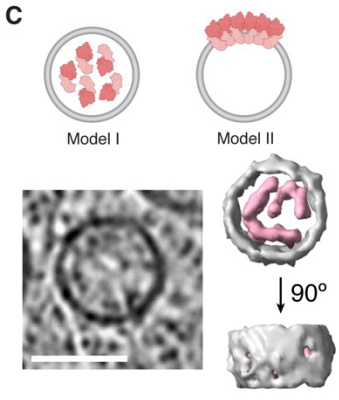
C
Model I
Model II
90°

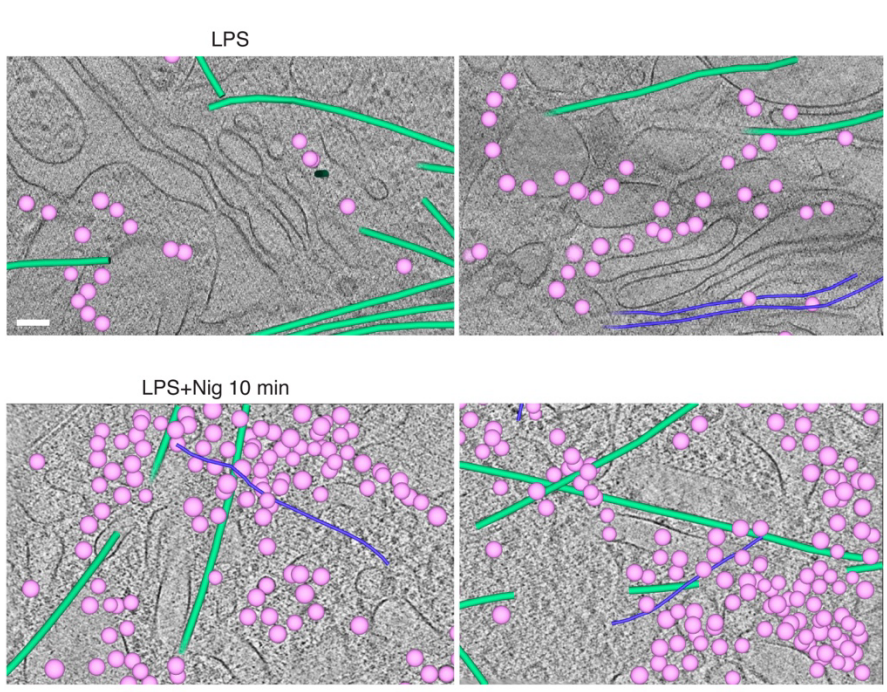
D
LPS
LPS+Nig 10 min

**Figure 4-S4. NLRP3-associated vesicles are ferry to the MTOC in response to TGN dispersion via microtubule independent mechanism. (A)** Representative examples of NLRP3-associated vesicles on TGN in primed cells and in the cytosol after addition of nigericin. Complete TGN cisternae are indicated as blue arrows and partial TGN structures or debris are indicated as dashed blue arrows. NLRP3-associated vesicles are circled or shaded in light pink (scale bar=100 nm). **(B)** NLRP3 associated vesicles are filled with protein densities compared to empty vesicles naturally present in cells (scale bar=50nm). Intensity profile of NLRP3-associated vesicles, blue line; empty vesicle, grey dashed line. **(C)** Density analysis of NLRP3 associated vesicles. A representative vesicle is shown together with segmented models (protein density, light pink, vesicle membrane, grey) (scale bar=50 nm). **(D)** Trafficking of NLRP3 associated vesicles is independent from retrograde transport. Cellular features are colored as following: NLRP3-associated vesicles, light pink; microtubules, green; intermediate filaments, purple (scale bar=100nm).

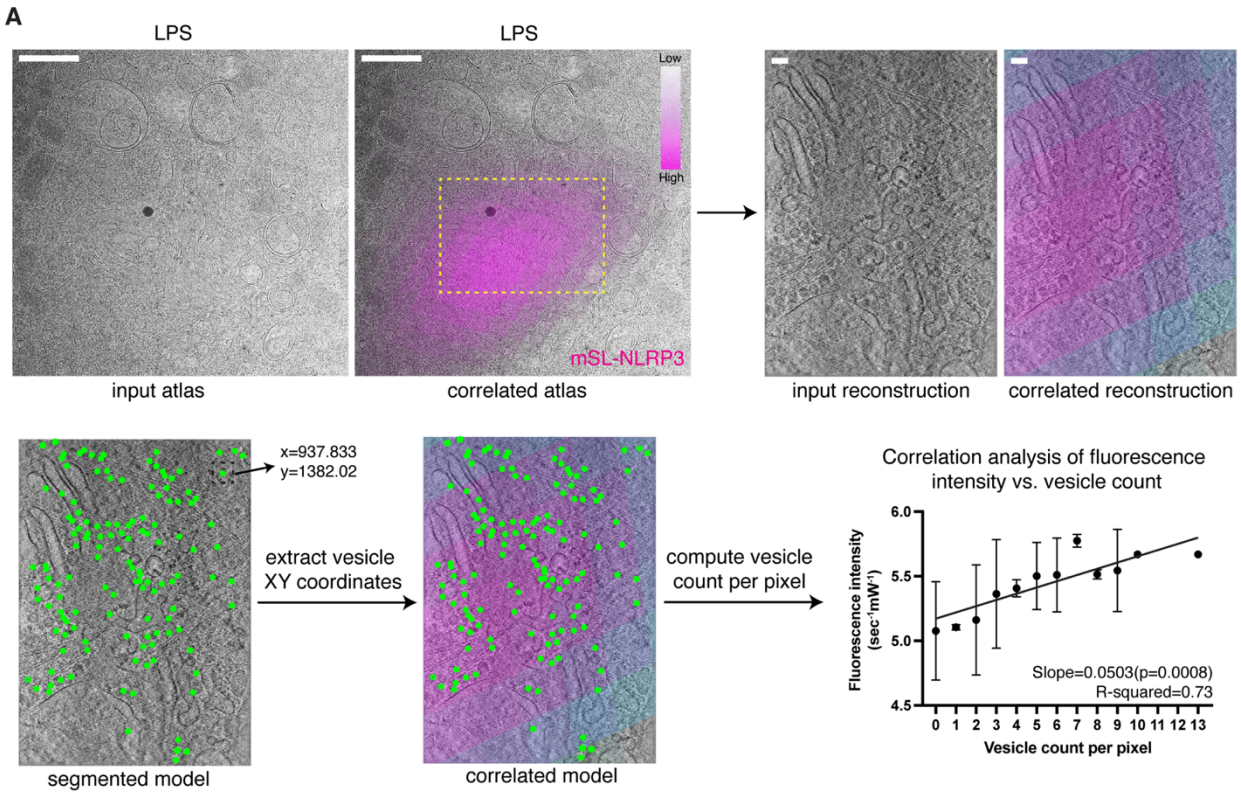
A
LPS
LPS
Low
High
mSL-NLRP3
input atlas
correlated atlas
input reconstruction
correlated reconstruction
x=937.833
y=1382.02
extract vesicle
XY coordinates
compute vesicle
count per pixel
segmented model
correlated model
Correlation analysis of fluorescence
intensity vs. vesicle count
Fluorescence intensity
(sec⁻¹mW⁻¹)
Slope=0.0503(p=0.0008)
R-squared=0.73
Vesicle count per pixel

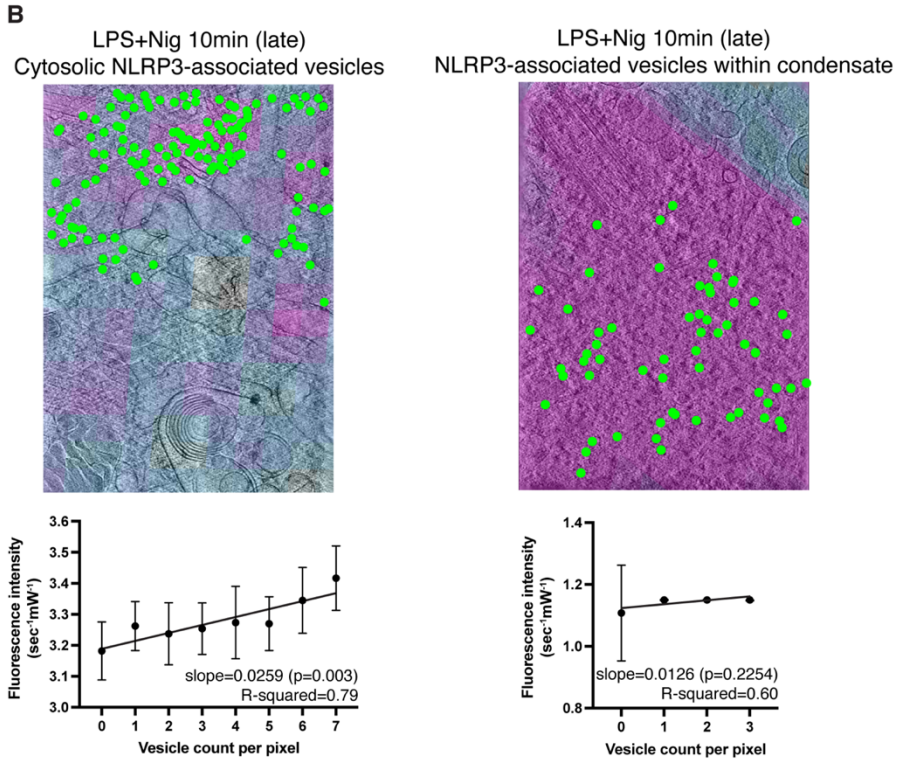
B
LPS+Nig 10min (late)
Cytosolic NLRP3-associated vesicles
LPS+Nig 10min (late)
NLRP3-associated vesicles within condensate
Fluorescence intensity
(sec⁻¹mW⁻¹)
slope=0.0259 (p=0.003)
R-squared=0.79
Vesicle count per pixel
slope=0.0126 (p=0.2254)
R-squared=0.60
Vesicle count per pixel

**Figure 4-S5. Fluorescence correlation analysis on NLRP3-associated vesicles. (A)** Workflow of computing correlation between mScarlet fluorescence intensity and NLRP3-associated vesicle density (scale bar=1 μm for atlas; scale bar=100 nm for reconstructions). Fluorescence intensity has been normalized by exposure time and laser power. **(B)** Correlation analysis on NLRP3-associated vesicles observed in the cytosol and at the MTOC after 10 min-nigericin treatment.

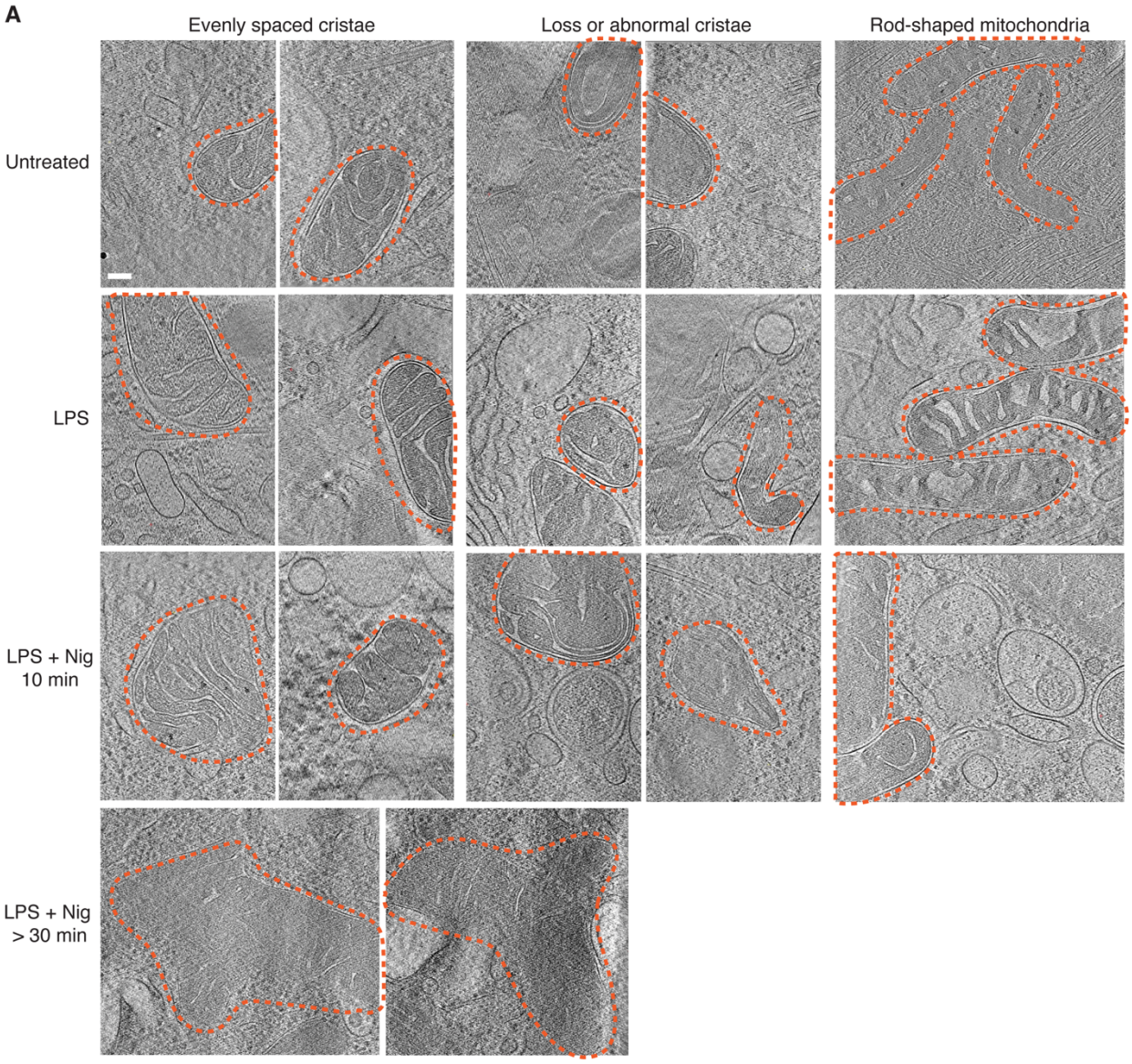
A
Evenly spaced cristae
Loss or abnormal cristae
Rod-shaped mitochondria
Untreated
LPS
LPS + Nig
10 min
LPS + Nig
> 30 min
B
Mitochondria within cluster
Mitochondria fusion within cluster
LPS + Nig
10 min

**Figure 4-S6. Mitochondria display a variety of morphology in response to NLRP3 inflammasome activation.** **(A)** Gallery showing mitochondrial morphology before and after NLRP3 inflammasome activation. Mitochondria are circled in orange (scale bar=100 nm). **(B)** Representative examples of mitochondria observed within clusters after 10 min-nigericin treatment (scale bar=100 nm).

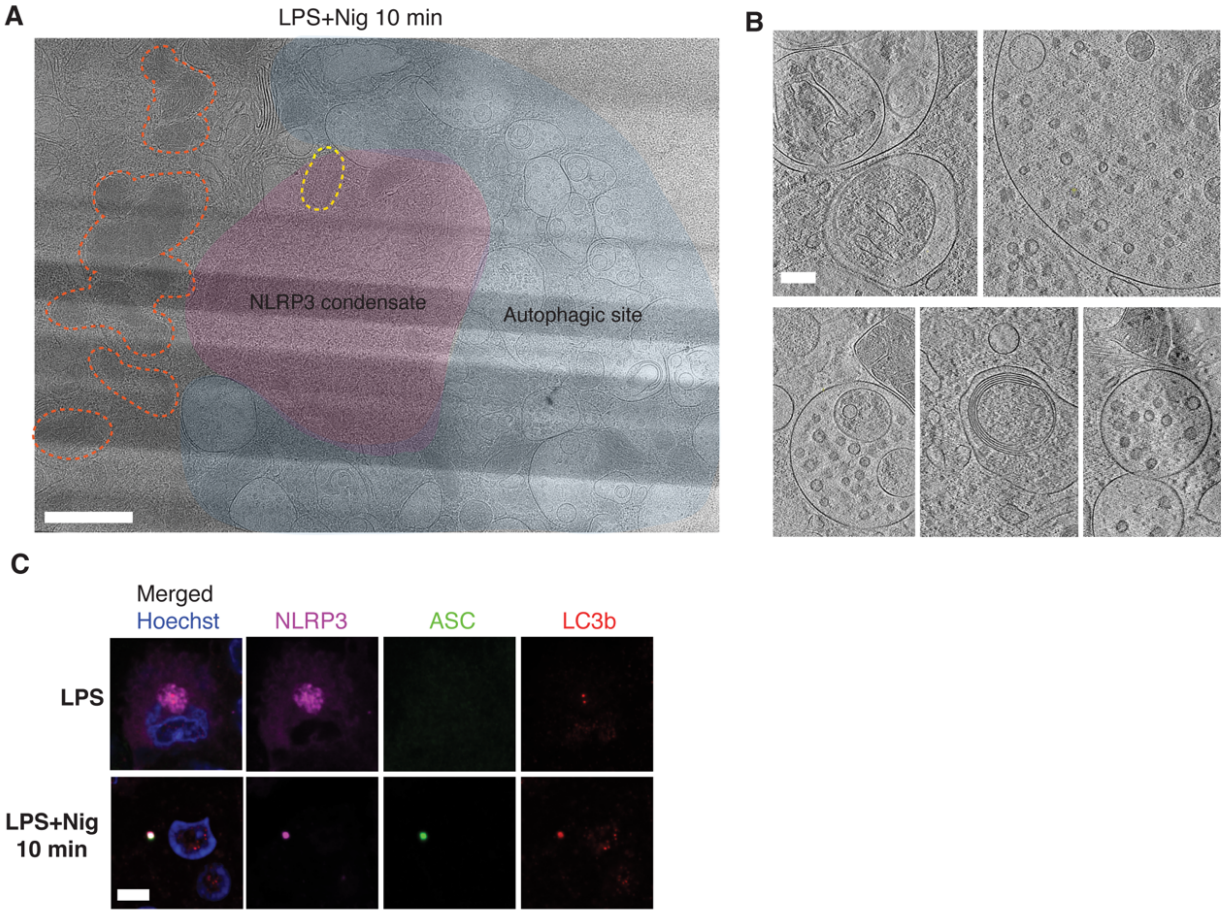


**Figure 4-S7. NLRP3 inflammasome condensate forms close contact with autophagic membranes. (A)** Representative atlas showing NLRP3 condensate, autophagic membranes, and mitochondria in proximity. Cellular features are marked as following: NLRP3 condensate; magenta, autophagic membranes, blue; mitochondria, orange (scale bar=1 μm). **(B)** Gallery of autophagic membranes present in close contact with NLRP3 condensate (scale bar=100 nm). **(C)** Immunofluorescent imaging of NLRP3, ASC and LC3B in fixed cells (scale bar=5 μm).

# CONCLUSIONS

This thesis pioneered a novel cryo-FM-FIB-SEM platform allowing simultaneous cryo-FM imaging and cryo-FIB milling to overcome difficulties in precise target localization. This method enables direct visualization of small and rare targets *in situ*. We used the ENZEL to localize the MTOC, previously shown as a challenging target to study by cryo-FIB-SEM. We showed a success rate >70% to retain the MTOC on the final lamella, compared to a success rate <7% reported in previous studies. Our results revealed the molecular architecture of the MTOC and structural details at the microtubule nucleation sites, providing improved understanding of the centrosome architecture and exciting mechanistic insights of microtubule nucleation. We further utilized this imaging platform to explore the NLRP3 inflammasome activation pathway as a complicated biological system. We provided the first in-situ image of this protein complex and showed the NLRP3 inflammasome forms a condensate at the MTOC. We also provided molecular evidence to explain why NLRP3 inflammasome and cell division are mutually exclusive since formation of condensate disrupts MTOC conformation. We also described organelle changes in response to NLRP3 inflammasome, such as Golgi expansion and dispersion, mitochondrial damage, and autophagosome formation. Collective observations *in situ* at various stages of inflammasome activation allowed us to purpose an improved mechanistic schematic of the NLRP3 inflammasome pathway. This thesis also demonstrated the potential of utilizing this imaging platform to investigate other protein complexes involved in the immune system or broader biological applications.

# BIBLIOGRAPHY

Abbate, A., et al. (2020). "Interleukin-1 and the inflammasome as therapeutic targets in cardiovascular disease." Circ Res **126**(9): 1260-1280.

Agarwal, S. and S. Ganesh (2020). "Perinuclear mitochondrial clustering, increased ROS levels, and HIF1 are required for the activation of HSF1 by heat stress." J Cell Sci **133**(13).

Agulleiro, J. I. and J. J. Fernandez (2011). "Fast tomographic reconstruction on multicore computers." Bioinformatics **27**(4): 582-583.

Agulleiro, J. I. and J. J. Fernandez (2015). "Tomo3D 2.0--exploitation of advanced vector extensions (AVX) for 3D reconstruction." J Struct Biol **189**(2): 147-152.

Al-Mehdi, A. B., et al. (2012). "Perinuclear mitochondrial clustering creates an oxidant-rich nuclear domain required for hypoxia-induced transcription." Sci Signal **5**(231): ra47.

Alberti, S. and A. A. Hyman (2021). "Biomolecular condensates at the nexus of cellular stress, protein aggregation disease and ageing." Nat Rev Mol Cell Biol **22**(3): 196-213.

Andreeva, L., et al. (2021). "NLRP3 cages revealed by full-length mouse NLRP3 structure control pathway activation." Cell **184**(26): 6299-6312.e6222.

Arnold, J., et al. (2016). "Site-specific cryo-focused ion beam sample preparation guided by 3D correlative microscopy." Biophys J **110**(4): 860-869.

Bai, S., et al. (2023). "Pyroptosis leads to loss of centrosomal integrity in macrophages." bioRxiv: 2023.2011.2022.568260.

Bertran, M. T., et al. (2011). "Nek9 is a Plk1-activated kinase that controls early centrosome separation through Nek6/7 and Eg5." EMBO J **30**(13): 2634-2647.

Boltje, D. B., et al. (2022). "A cryogenic, coincident fluorescence, electron, and ion beam microscope." eLife **11**.

Breslow, D. K. and A. J. Holland (2019). "Mechanism and Regulation of Centriole and Cilium Biogenesis." Annu Rev Biochem **88**: 691-724.

Brilot, A. F., et al. (2021). "CM1-driven assembly and activation of yeast γ-tubulin small complex underlies microtubule nucleation." eLife **10**.

Broz, P. and V. M. Dixit (2016). "Inflammasomes: mechanism of assembly, regulation and signalling." Nat Rev Immunol **16**(7): 407-420.

Busselez, J., et al. (2019). "Cryo-electron tomography and proteomics studies of centrosomes from differentiated quiescent thymocytes." Sci Rep **9**(1): 7187.

Bykov, Y. S., et al. (2017). "The structure of the COPI coat determined within the cell." eLife **6**.

Carter, S. D., et al. (2020). "Correlated cryogenic fluorescence microscopy and electron cryo-tomography shows that exogenous TRIM5α can form hexagonal lattices or autophagy aggregates in vivo." Proc Natl Acad Sci USA **117**(47): 29702-29711.

Carvalho-Santos, Z., et al. (2011). "Evolution: Tracing the origins of centrioles, cilia, and flagella." J Cell Biol **194**(2): 165-175.

Chen, J. and Z. J. Chen (2018). "PtdIns4P on dispersed trans-Golgi network mediates NLRP3 inflammasome activation." Nature **564**(7734): 71-76.

Cheng, Y. (2018). "Single-particle cryo-EM-How did it get here and where will it go." Science **361**(6405): 876-880.

Christgen, S., et al. (2020). "Toward targeting inflammasomes: Insights into their regulation and activation." Cell Res **30**(4): 315-327.

Clarey, M. G., et al. (2008). "Single particle EM studies of the Drosophila melanogaster origin recognition complex and evidence for DNA wrapping." J Struct Biol **164**(3): 241-249.

Conduit, P. T., et al. (2015). "Centrosome function and assembly in animal cells." Nat Rev Mol Cell Biol **16**(10): 611-624.

Consolati, T., et al. (2020). "Microtubule nucleation properties of single human γTuRCs explained by their cryo-EM structure." Dev Cell **53**(5): 603-617.e608.

Cui, L., et al. (2022). "Vesicle trafficking and vesicle fusion: Mechanisms, biological functions, and their implications for potential disease therapy." Mol Biomed **3**(1): 29.

Dahlberg, P. D., et al. (2022). "Metallic support films reduce optical heating in cryogenic correlative light and electron tomography." J Struct Biol **214**(4): 107901.

Dendooven, T., et al. (2024). "Structure of the native γ-tubulin ring complex capping spindle microtubules." Nat Struct Mol Biol **31**(7): 1134-1144.

Dobro, M. J., et al. (2010). "Plunge freezing for electron cryomicroscopy." Methods Enzymol **481**: 63-82.

Dong, Y., et al. (2024). "Structural transitions enable interleukin-18 maturation and signaling." Immunity.

dos Santos, G., et al. (2015). "Vimentin regulates activation of the NLRP3 inflammasome." Nat Commun **6**: 6574.

Du, G., et al. (2024). "ROS-dependent S-palmitoylation activates cleaved and intact gasdermin D." Nature **630**(8016): 437-446.

Du, M. and Z. J. Chen (2018). "DNA-induced liquid phase condensation of cGAS activates innate immune signaling." Science **361**(6403): 704-709.

Dunlop, M. H., et al. (2017). "Land-locked mammalian Golgi reveals cargo transport between stable cisternae." Nat Commun **8**(1): 432.

Fernández-Busnadiego, R., et al. (2010). "Quantitative analysis of the native presynaptic cytomatrix by cryoelectron tomography." J Cell Biol **188**(1): 145-156.

Frank, J. (2016). "Generalized single-particle cryo-EM – a historical perspective." Microscopy (Oxf) **65**(1): 3-8.

Fribourgh, J. L., et al. (2014). "Structural insight into HIV-1 restriction by MxB." Cell Host Microbe **16**(5): 627-638.

Fu, J. and H. Wu (2023). "Structural mechanisms of NLRP3 inflammasome assembly and activation." Annu Rev Immunol **41**: 301-316.

Fu, X., et al. (2019). "AutoCLEM: An Automated Workflow for Correlative Live-Cell Fluorescence Microscopy and Cryo-Electron Tomography." Sci Rep **9**(1): 19207.

Fujita, H., et al. (2016). "Regulation of the centrosome cycle." Mol Cell Oncol **3**(2): e1075643.

Gaidt, M. M. and V. Hornung (2018). "The NLRP3 Inflammasome Renders Cell Death Pro-inflammatory." J Mol Biol **430**(2): 133-141.

Garcia Quiroz, F., et al. (2019). "Intrinsically disordered proteins access a range of hysteretic phase separation behaviors." Sci Adv **5**(10): eaax5177.

Gould, R. R. and G. G. Borisy (1977). "The pericentriolar material in Chinese hamster ovary cells nucleates microtubule formation." J Cell Biol **73**(3): 601-615.

Guichard, P., et al. (2020). "Native architecture of the centriole proximal region reveals features underlying its 9-fold radial symmetry." Curr Biol **30**(11): 2204.

Guillet, V., et al. (2011). "Crystal structure of γ-tubulin complex protein GCP4 provides insight into microtubule nucleation." Nat Struct Mol Biol **18**(8): 915-919.

Guo, Q., et al. (2018). "*In situ* structure of neuronal C9orf72 poly-GA aggregates reveals proteasome recruitment." Cell **172**(4): 696-705.e612.

Gurung, P., et al. (2015). "Mitochondria: diversity in the regulation of the NLRP3 inflammasome." Trends Mol Med **21**(3): 193-201.

Hampton, C. M., et al. (2017). "Correlated fluorescence microscopy and cryo-electron tomography of virus-infected or transfected mammalian cells." Nat Protoc **12**(1): 150-167.

He, Y., et al. (2016). "NEK7 is an essential mediator of NLRP3 activation downstream of potassium efflux." Nature **530**(7590): 354-357.

Heebner, J. E., et al. (2022). "Deep learning-based segmentation of cryo-electron tomograms." J Vis Exp(189).

Henderson, R., et al. (1990). "Model for the structure of bacteriorhodopsin based on high-resolution electron cryo-microscopy." J Mol Biol **213**(4): 899-929.

Hochheiser, I. V., et al. (2022). "Structure of the NLRP3 decamer bound to the cytokine release inhibitor CRID3." Nature **604**(7904): 184-189.

Hornung, V., et al. (2009). "AIM2 recognizes cytosolic dsDNA and forms a caspase-1-activating inflammasome with ASC." Nature **458**(7237): 514-518.

Huang, P., et al. (2007). "Mitochondrial clustering induced by overexpression of the mitochondrial fusion protein Mfn2 causes mitochondrial dysfunction and cell death." Eur J Cell Biol **86**(6): 289-302.

Huo, Y., et al. (2022). "The MFN1 and MFN2 mitofusins promote clustering between mitochondria and peroxisomes." Commun Biol **5**(1): 423.

Iancu, C. V., et al. (2006). "Electron cryotomography sample preparation using the Vitrobot." Nat Protoc **1**(6): 2813-2819.

Jana, S. C. (2021). "Centrosome structure and biogenesis: Variations on a theme?" Semin Cell Dev Biol **110**: 123-138.

Jana, S. C., et al. (2014). "Mapping molecules to structure: unveiling secrets of centriole and cilia assembly with near-atomic resolution." Curr Opin Cell Biol **26**: 96-106.

Jiang, X., et al. (2021). "Condensation of pericentrin proteins in human cells illuminates phase separation in centrosome assembly." J Cell Sci **134**(14).

Jobe, F., et al. (2020). "Respiratory Syncytial Virus Sequesters NF-$\varkappa$B Subunit p65 to Cytoplasmic Inclusion Bodies To Inhibit Innate Immune Signaling." J Virol **94**(22).

Kaasik, A., et al. (2007). "Regulation of mitochondrial matrix volume." Am J Physiol Cell Physiol **292**(1): C157-163.

Kantsadi, A. L., et al. (2022). "Structures of SAS-6 coiled coil hold implications for the polarity of the centriolar cartwheel." Structure **30**(5): 671-684.e675.

Kaplan, M., et al. (2021). "*In situ* imaging and structure determination of biomolecular complexes using electron cryo-tomography." Methods Mol Biol **2215**: 83-111.

Kollman, J. M., et al. (2011). "Microtubule nucleation by γ-tubulin complexes." Nat Rev Mol Cell Biol **12**(11): 709-721.

Komeili, A., et al. (2006). "Magnetosomes are cell membrane invaginations organized by the actin-like protein MamK." Science **311**(5758): 242-245.

Kremer, J. R., et al. (1996). "Computer visualization of three-dimensional image data using IMOD." J Struct Biol **116**(1): 71-76.

Kumar, A., et al. (2014). "Role of centrosome in regulating immune response." Curr Drug Targets **15**(5): 558-563.

Ladinsky, M. S., et al. (1999). "Golgi structure in three dimensions: functional insights from the normal rat kidney cell." J Cell Biol **144**(6): 1135-1149.

Lam, V. and E. Villa (2021). "Practical approaches for cryo-FIB milling and applications for cellular cryo-electron tomography." Methods Mol Biol **2215**: 49-82.

Lamkanfi, M. and V. M. Dixit (2014). "Mechanisms and functions of inflammasomes." Cell **157**(5): 1013-1022.

Lang, T., et al. (2018). "Macrophage migration inhibitory factor is required for NLRP3 inflammasome activation." Nat Commun **9**(1): 2223.

Laporte, M. H., et al. (2024). "Time-series reconstruction of the molecular architecture of human centriole assembly." Cell **187**(9): 2158-2174.e2119.

Last, M. G. F., et al. (2023). "Selecting optimal support grids for super-resolution cryogenic correlated light and electron microscopy." Sci Rep **13**(1): 8270.

Lee, B., et al. (2023). "Disruptions in endocytic traffic contribute to the activation of the NLRP3 inflammasome." Sci Signal **16**(773): eabm7134.

LeGuennec, M., et al. (2021). "Overview of the centriole architecture." Curr Opin Struct Biol **66**: 58-65.

Leidel, S., et al. (2005). "SAS-6 defines a protein family required for centrosome duplication in C. elegans and in human cells." Nat Cell Biol **7**(2): 115-125.

Li, S., et al. (2019). "Electron cryo-tomography provides insight into procentriole architecture and assembly mechanism." Elife **8**.

Li, S., et al. (2023). "ELI trifocal microscope: A precise system to prepare target cryo-lamellae for in situ cryo-ET study." Nat Methods **20**(2): 276-283.

Li, X., et al. (2013). "Electron counting and beam-induced motion correction enable near-atomic-resolution single-particle cryo-EM." Nat Methods **10**(6): 584-590.

Li, X., et al. (2017). "MARK4 regulates NLRP3 positioning and inflammasome activation through a microtubule-dependent mechanism." Nat Commun **8**: 15986.

Li, Y., et al. (2018). "Cryo-EM structures of ASC and NLRC4 CARD filaments reveal a unified mechanism of nucleation and activation of caspase-1." Proc Natl Acad Sci U S A **115**(43): 10845-10852.

Liao, M., et al. (2013). "Structure of the TRPV1 ion channel determined by electron cryo-microscopy." Nature **504**(7478): 107-112.

Lieberman, J., et al. (2019). "Gasdermin D activity in inflammation and host defense." Sci Immunol **4**(39).

Lin, S. C., et al. (2010). "Helical assembly in the MyD88-IRAK4-IRAK2 complex in TLR/IL-1R signalling." Nature **465**(7300): 885-890.

Liu, Q., et al. (2018). "The role of mitochondria in NLRP3 inflammasome activation." Mol Immunol **103**: 115-124.

Liu, Y., et al. (2023). "Cryo-electron tomography of NLRP3-activated ASC complexes reveals organelle co-localization." Nat Commun **14**(1): 7246.

Loginov, S. V., et al. (2024). "Depth-dependent scaling of axial distances in light microscopy." Optica **11**: 553-568.

Lu, A., et al. (2014). "Unified polymerization mechanism for the assembly of ASC-dependent inflammasomes." Cell **156**(6): 1193-1206.

Lukinavičius, G., et al. (2014). "Fluorogenic probes for live-cell imaging of the cytoskeleton." Nat Methods **11**(7): 731-733.

Magupalli, V. G., et al. (2020). "HDAC6 mediates an aggresome-like mechanism for NLRP3 and pyrin inflammasome activation." Science **369**(6510).

Mahamid, J., et al. (2016). "Visualizing the molecular sociology at the HeLa cell nuclear periphery." Science **351**(6276): 969-972.

Mastronarde, D. N. (2003). "SerialEM: A program for automated tilt series acquisition on Tecnai microscopes using prediction of specimen position." Microscopy and Microanalysis **9**(S02): 1182-1183.

Mastronarde, D. N. (2005). "Automated electron microscope tomography using robust prediction of specimen movements." J Struct Biol **152**(1): 36-51.

Mastronarde, D. N. and S. R. Held (2017). "Automated tilt series alignment and tomographic reconstruction in IMOD." J Struct Biol **197**(2): 102-113.

McMullan, G., et al. (2014). "Comparison of optimal performance at 300keV of three direct electron detectors for use in low dose electron microscopy." Ultramicroscopy **147**: 156-163.

Meng, E. C., et al. (2023). "UCSF ChimeraX: Tools for structure building and analysis." Protein Sci **32**(11): e4792.

Miao, R., et al. (2023). "Gasdermin D permeabilization of mitochondrial inner and outer membranes accelerates and enhances pyroptosis." Immunity **56**(11): 2523-2541.e2528.

Milovanovic, D., et al. (2018). "A liquid phase of synapsin and lipid vesicles." Science **361**(6402): 604-607.

Mishra, S. R., et al. (2021). "Mitochondrial dysfunction as a driver of NLRP3 inflammasome activation and its modulation through mitophagy for potential therapeutics." Int J Biochem Cell Biol **136**: 106013.

Murphy, K. and C. Weaver (2017). Janeway's immunobiology. New York, NY, Garland Science/Taylor & Francis Group, LLC.

Muñoz-Planillo, R., et al. (2013). "$K^+$ efflux is the common trigger of NLRP3 inflammasome activation by bacterial toxins and particulate matter." Immunity **38**(6): 1142-1153.

Navone, F., et al. (1984). "Synapsin I in nerve terminals: selective association with small synaptic vesicles." Science **226**(4679): 1209-1211.

Nelson, J. C., et al. (2013). "The actin cytoskeleton in presynaptic assembly." Cell Adh Migr **7**(4): 379-387.

Noble, A. J. and A. de Marco (2024). "Cryo-focused ion beam for in situ structural biology: State of the art, challenges, and perspectives." Curr Opin Struct Biol **87**: 102864.

Nogales, E. and J. Mahamid (2024). "Bridging structural and cell biology with cryo-electron microscopy." Nature **628**(8006): 47-56.

Nogales, E. and S. H. Scheres (2015). "Cryo-EM: A unique tool for the visualization of macromolecular complexity." Mol Cell **58**(4): 677-689.

Ohto, U., et al. (2022). "Structural basis for the oligomerization-mediated regulation of NLRP3 inflammasome activation." Proc Natl Acad Sci U S A **119**(11): e2121353119.

Paintrand, M., et al. (1992). "Centrosome organization and centriole architecture: Their sensitivity to divalent cations." J Struct Biol **108**(2): 107-128.

Pancione, M., et al. (2021). "Centrosome dynamics and its role in inflammatory response and metastatic process." Biomolecules **11**(5).

Park, H. H., et al. (2007). "Death domain assembly mechanism revealed by crystal structure of the oligomeric PIDDosome core complex." Cell **128**(3): 533-546.

Perez, D., et al. (2022). "Identification and demonstration of roGFP2 as an environmental sensor for cryogenic correlative light and electron microscopy." J Struct Biol **214**(3): 107881.

Petrov, P. N. and W. E. Moerner (2020). "Addressing systematic errors in axial distance measurements in single-emitter localization microscopy." Opt Express **28**(13): 18616-18632.

Qi, F. and J. Zhou (2021). "Multifaceted roles of centrosomes in development, health, and disease." J Mol Cell Biol **13**(9): 611-621.

Qiu, H., et al. (2024). "Short-distance vesicle transport via phase separation." Cell **187**(9): 2175-2193.e2121.

Que, X., et al. (2024). "Fantastic voyage: The journey of NLRP3 inflammasome activation." Genes Dis **11**(2): 819-829.

Rigort, A. and J. M. Plitzko (2015). "Cryo-focused-ion-beam applications in structural biology." Arch Biochem Biophys **581**: 122-130.

Sanchez, A. D. and J. L. Feldman (2017). "Microtubule-organizing centers: from the centrosome to non-centrosomal sites." Curr Opin Cell Biol **44**: 93-101.

Sartor, A. M., et al. (2023). "Characterization of mApple as a red fluorescent protein for cryogenic single-Molecule Imaging with Turn-Off and Turn-On Active Control Mechanisms." J Phys Chem B **127**(12): 2690-2700.

Sborgi, L., et al. (2015). "Structure and assembly of the mouse ASC inflammasome by combined NMR spectroscopy and cryo-electron microscopy." Proc Natl Acad Sci U S A **112**(43): 13237-13242.

Schapfl, M. A., et al. (2024). "Centrioles are frequently amplified in early B cell development but dispensable for humoral immunity." Nat Commun **15**(1): 8890.

Schindelin, J., et al. (2012). "Fiji: an open-source platform for biological-image analysis." Nat Methods **9**(7): 676-682.

Schmacke, N. A., et al. (2022). "IKKβ primes inflammasome formation by recruiting NLRP3 to the trans-Golgi network." Immunity **55**(12): 2271-2284.e2277.

Schmid-Burgk, J. L., et al. (2016). "A genome-wide CRISPR (Clustered Regularly Interspaced Short Palindromic Repeats) screen identifies NEK7 as an essential component of NLRP3 inflammasome activation." J Biol Chem **291**(1): 103-109.

Schroder, K. and J. Tschopp (2010). "The inflammasomes." Cell **140**(6): 821-832.

Sexton, D. L., et al. (2022). "Super-resolution confocal cryo-CLEM with cryo-FIB milling for." Curr Res Struct Biol **4**: 1-9.

Shapiro, D. M., et al. (2021). "Protein phase separation arising from intrinsic disorder: First-principles to bespoke applications." J Phys Chem B **125**(25): 6740-6759.

Sharif, H., et al. (2019). "Structural mechanism for NEK7-licensed activation of NLRP3 inflammasome." Nature **570**(7761): 338-343.

Shen, C., et al. (2021). "Phase separation drives RNA virus-induced activation of the NLRP6 inflammasome." Cell **184**(23): 5759-5774.e5720.

Shi, H., et al. (2016). "NLRP3 activation and mitosis are mutually exclusive events coordinated by NEK7, a new inflammasome component." Nat Immunol **17**(3): 250-258.

Sica, A. V., et al. (2024). "Optical interference for the guidance of cryogenic focused ion beam milling beyond the axial diffraction limit." bioRxiv: 2024.2011.2001.621231.

Smith, E., et al. (2011). "Differential control of Eg5-dependent centrosome separation by Plk1 and Cdk1." EMBO J **30**(11): 2233-2245.

Stutz, A., et al. (2009). "Inflammasomes: Too big to miss." J Clin Invest **119**(12): 3502-3511.

Stutz, A., et al. (2013). "ASC speck formation as a readout for inflammasome activation." Methods Mol Biol **1040**: 91-101.

Su, X., et al. (2016). "Phase separation of signaling molecules promotes T cell receptor signal transduction." Science **352**(6285): 595-599.

Su, Z., et al. (2021). "Cryo-EM structures of full-length Tetrahymena ribozyme at 3.1 Å resolution." Nature **596**(7873): 603-607.

Swanson, K. V., et al. (2019). "The NLRP3 inflammasome: Molecular activation and regulation to therapeutics." Nat Rev Immunol **19**(8): 477-489.

Südhof, T. C., et al. (1993). "Membrane fusion machinery: insights from synaptic proteins." Cell **75**(1): 1-4.

Tegunov, D. and P. Cramer (2019). "Real-time cryo-electron microscopy data preprocessing with Warp." Nat Methods **16**(11): 1146-1152.

Tegunov, D., et al. (2021). "Multi-particle cryo-EM refinement with M visualizes ribosome-antibiotic complex at 3.5 Å in cells." Nat Methods **18**(2): 186-193.

Tollervey, F., et al. (2024). "Molecular architectures of centrosomes in C. elegans embryos visualized by cryo-electron tomography." Dev Cell.

Tovey, C. A. and P. T. Conduit (2018). "Microtubule nucleation by γ-tubulin complexes and beyond." Essays Biochem **62**(6): 765-780.

Verba, K. A., et al. (2016). "Atomic structure of Hsp90-Cdc37-Cdk4 reveals that Hsp90 traps and stabilizes an unfolded kinase." Science **352**(6293): 1542-1547.

Vertii, A., et al. (2016). "The centrosome undergoes Plk1-independent interphase maturation during inflammation and mediates cytokine release." Dev Cell **37**(4): 377-386.

Villa, E., et al. (2013). "Opening windows into the cell: focused-ion-beam milling for cryo-electron tomography." Curr Opin Struct Biol **23**(5): 771-777.

Vitiello, E., et al. (2019). "Acto-myosin force organization modulates centriole separation and PLK4 recruitment to ensure centriole fidelity." Nat Commun **10**(1): 52.

Wagner, F. R., et al. (2020). "Preparing samples from whole cells using focused-ion-beam milling for cryo-electron tomography." Nat Protoc **15**(6): 2041-2070.

Wang, L., et al. (2021). "Structures and functions of the inflammasome engine." J Allergy Clin Immunol **147**(6): 2021-2029.

Wang, Z., et al. (2020). "NLRP3 inflammasome and inflammatory diseases." Oxid Med Cell Longev **2020**: 4063562.

Weier, A. K., et al. (2022). "Multiple centrosomes enhance migration and immune cell effector functions of mature dendritic cells." J Cell Biol **221**(12).

Williams, D. M. and A. A. Peden (2023). "S-acylation of NLRP3 provides a nigericin sensitive gating mechanism that controls access to the Golgi." bioRxiv: 2023.2011.2014.566891.

Winey, M. and E. O'Toole (2014). "Centriole structure." Philos Trans R Soc Lond B Biol Sci **369**(1650).

Woodruff, J. B., et al. (2017). "The centrosome is a selective condensate that nucleates microtubules by concentrating yubulin." Cell **169**(6): 1066-1077.e1010.

Woodruff, J. B., et al. (2014). "Pericentriolar material structure and dynamics." Philos Trans R Soc Lond B Biol Sci **369**(1650).

Wu, D., et al. (2022). "Inflammasome meets centrosome: Understanding the emerging role of centrosome in controlling inflammasome activation." Front Immunol **13**: 826106.

Wu, G. H., et al. (2020). "Multi-scale 3D cryo-correlative microscopy for vitrified cells." Structure **28**(11): 1231-1237.e1233.

Wu, H. (2013). "Higher-order assemblies in a new paradigm of signal transduction." Cell **153**(2): 287-292.

Wu, H. and M. Fuxreiter (2016). "The structure and dynamics of higher-order assemblies: Amyloids, signalosomes, and granules." Cell **165**(5): 1055-1066.

Wu, J., et al. (2021). "The role of the inflammasome in heart failure." Front Physiol **12**: 709703.

Wu, J., et al. (2010). "Involvement of the AIM2, NLRC4, and NLRP3 inflammasomes in caspase-1 activation by Listeria monocytogenes." J Clin Immunol **30**(5): 693-702.

Wu, S., et al. (2016). "Single-particle cryo-EM data acquisition by using direct electron detection camera." Microscopy (Oxf) **65**(1): 35-41.

Würtz, M., et al. (2022). "Modular assembly of the principal microtubule nucleator γ-TuRC." Nat Commun **13**(1): 473.

Xian, H., et al. (2022). "Oxidized DNA fragments exit mitochondria via mPTP- and VDAC-dependent channels to activate NLRP3 inflammasome and interferon signaling." Immunity **55**(8): 1370-1385.e1378.

Xiao, L., et al. (2023). "Cryo-EM structures of the active NLRP3 inflammasome disc." Nature **613**(7944): 595-600.

Xue, L., et al. (2022). "Visualizing translation dynamics at atomic detail inside a bacterial cell." Nature **610**(7930): 205-211.

Yabal, M., et al. (2019). "Stressing out the mitochondria: Mechanistic insights into NLRP3 inflammasome activation." J Leukoc Biol **105**(2): 377-399.

Yang, J. E., et al. (2021). "CorRelator: Interactive software for real-time high precision cryo-correlative light and electron microscopy." J Struct Biol **213**(2): 107709.

Yu, X., et al. (2024). "Structural basis for the oligomerization-facilitated NLRP3 activation." Nat Commun **15**(1): 1164.

Yu, X., et al. (2021). "The STING phase-separator suppresses innate immune signalling." Nat Cell Biol **23**(4): 330-340.

Zahid, A., et al. (2019). "Pharmacological Inhibitors of the NLRP3 Inflammasome." Front Immunol **10**: 2538.

Zhang, J., et al. (2010). "Mechanism of folding chamber closure in a group II chaperonin." Nature **463**(7279): 379-383.

Zhang, L., et al. (2015). "Cryo-EM structure of the activated NAIP2-NLRC4 inflammasome reveals nucleated polymerization." Science **350**(6259): 404-409.

Zhang, X., et al. (2023). "Molecular mechanisms of stress-induced reactivation in mumps virus condensates." Cell **186**(9): 1877-1894.e1827.

Zhang, Z., et al. (2023). "Distinct changes in endosomal composition promote NLRP3 inflammasome activation." Nat Immunol **24**(1): 30-41.

Zhou, R., et al. (2011). "A role for mitochondria in NLRP3 inflammasome activation." Nature **469**(7329): 221-225.

Zimmermann, F., et al. (2020). "Assembly of the asymmetric human γ-tubulin ring complex by RUVBL1-RUVBL2 AAA ATPase." Sci Adv **6**(51).

Zwicker, D., et al. (2014). "Centrosomes are autocatalytic droplets of pericentriolar material organized by centrioles." Proc Natl Acad Sci U S A **111**(26): E2636-2645.